UNIVERSITY OF OKLAHOMA

GRADUATE COLLEGE

SEISMIC DETECTION OF FAULT ZONE HYDROCARBON CONDUIT-SEAL POTENTIAL USING VELOCITY, FREQUENCY, AND *Q* ANALYSIS: LA CONCEPCION FIELD, LAKE MARACAIBO VENEZUELA EXAMPLE

A Dissertation
SUBMITTED TO THE GRADUATE FACULTY

in partial fulfillment of the requirements for the
Degree of

Doctor of Philosophy

by

AHMED OMAR ALAHDAL

NORMAN, OKLAHOMA

2006

UMI Number: 3242291

ProQuest Information and Learning Company
300 North Zeeb Road
P.O. Box 1346
Ann Arbor, MI 48106-1346

SEISMIC DETECTION OF FAULT ZONE HYDROCARBON CONDUIT-SEAL POTENTIAL USING VELOCITY, FREQUENCY, AND *Q* ANALYSIS: LA CONCEPCION FIELD, LAKE MARACAIBO VENEZUELA EXAMPLE

A Dissertation APPROVED FOR THE
SCHOOL OF GEOLOGY AND GEOPHYSICS

BY

Dr. John D. Pigott

Dr. Judson L. Ahern

Dr. Raymon Brown

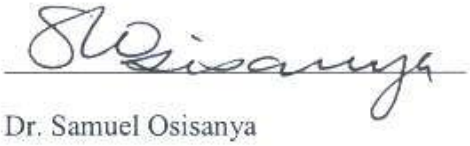

Dr. Samuel Osisanya

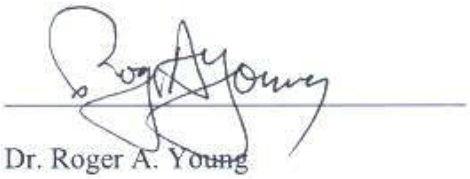

Dr. Roger A. Young

ACKNOWLEDGMENTS

I would like to express my sincere appreciation to a number of people for guidance and support throughout this dissertation research. Thank You to my advisor, Dr. John Pigott, for your cordial and consistent advice, encouragement and support. for guidance and friendship.

Thank You to my dissertation committee members, Dr. Roger Young, Dr. Judson Ahern, Dr. Raymon Brown for their consistent encouragement, advices and endless assistance. Thank You to Dr. Samuel Osisanya for serving as my committee member and for his nice friendship.

Thank You to Jan Dodson for your computer assistance. Thank You to Donna Mullins for your assistance, advice and friendship. I would like to thank my colleagues and friends that I have made at the University of Oklahoma. Friends who helped me with the encouragements and their faith in my ability and confidence to complete my dissertation. Special thank to my friend Yasser Mohamed for his endless assistance and encouragements.

I would like to express my gratitude to the School of Geology and Geophysics at the University of Oklahoma for the consistent financial support without which, this work would not have been possible. I would like to thank the Society of Exploration Geophysicists (SEG) and the Geophysical Society of Oklahoma City (GS.OKC) student scholarship for awarding me a scholarship. I

am grateful to the American Federation of Mineralogical Societies for their generosity and financial support.

I would like to thank Dr. Ferro Elmer of Petrobras Energia. Thank you for supplying the data used in this research. Without your data, this work would not have been possible.

Last but not the least I would like to thank all my family. Special thanks to my wife “Saeeda Ghafoor Alahdal for her consistent patience, understanding and encouragement. Big thanks be to God.

TABLE OF CONTENTS

LIST OF FIGURES

LIST OF TABLES

ABSTRACT

The 3-D Post-Stack Time Migrated Seismic Data of La Concepcion Field, Maracaibo Basin, Venezuela cover an existing field with known oil and gas pay zones. The thesis problem is how to use this seismic data in an interpretation of leaky faults that occur in the exploration area of interest. A solution to the problem was obtained using an integrated geophysical approach that included published seismic attribute methods (Variance Cube, Geoframe IESX). Specific developments in this thesis to solve the interpretation problem of leaky faults in the region include (1) an image ray perturbation approach for updating the interval velocity in a faulted domain (2) a peak frequency approach to attenuation estimation within intervals and (3) a scaled interpretation of the velocity measurements at sonic, checkshot and surface seismic reflection data. The first development refines the interval velocities within fracture zones. The second development identifies anomalous attenuation most likely due to the presence of gas. The combined effects of low interval velocity and high attenuation are interpreted to be signs of leaking faults.

CHAPTER 1

PROBLEM DEFINITION

1.1 Importance

One of many critical components (Metwalli and Pigott, 2005) which can control the charge of a hydrocarbon reservoir is a fault, whether permeable or impermeable. Most present day seismic reflection analyses focus upon the detection and mapping of fault images rather than determining their physical properties, e.g. permeability. This dissertation addresses the seismic information behind the image and attempts to relate the extracted information to the potential for fault-zone permeability (leaky faults).

1.2 Location of Study Area

La Concepcion field is located in the northwestern portion of the Maracaibo Basin in the Zulia county of Venezuela (Figure 1.1). The field covers a surface of 248 km^2, bounded by the oil fields of La Paz, Mara, Sibucare, and Boscan. La Concepcion field was discovered in 1924 with the C-X-1 exploration well by the Venezuelan Oil Consortium Ltd. (Shell). It consists of two major reservoirs with sub-equal cumulative oil reserves: an Eocene reservoir and Cretaceous reservoir (Ferro et al., 2001).

1.3 Statement of the Problem

The 3-D, post-stack time-migrated seismic data of La Concepcion field in the Maracaibo Basin, Venezuela, covers an existing field with known pay zones of oil and gas. The question of whether the seismic response is indicative of the presence of fractures and/or the gas-saturation of the fractures is considered. An interpretation technique for predicting fractures and gas saturation is developed based upon velocity anomalies associated with fractures, frequency and Q analysis. In other words, this dissertation concerns the detection and analysis of velocity anomalies owing to subtle fractures, peak frequency and inverse attenuation Q in La Concepcion field, Venezuela. The approach combines seismic attributes, and analysis of image-ray perturbation through depth conversion method as an interval velocity estimation, peak frequencies and seismic quality factor Q.

1.4 Data Used

The data used in this study includes 3-D, post-stack, time-migrated seismic data along with root-mean square velocities, V_{rms}, checkshot two-way times, gamma-ray, bulk density, and sonic logs, and depths to formation tops.

1.4.1 3-D Time-Migrated Seismic Data

The 3D seismic data cube (approx 250 km^2) as shown in Figure 1.2 was acquired by Western Geco (formerly Western Geophysical) during the years

1999 and 2000. The field acquisition parameters are shown in Table 1.1, and the processing sequences of the seismic data applied by Veritas are listed below:

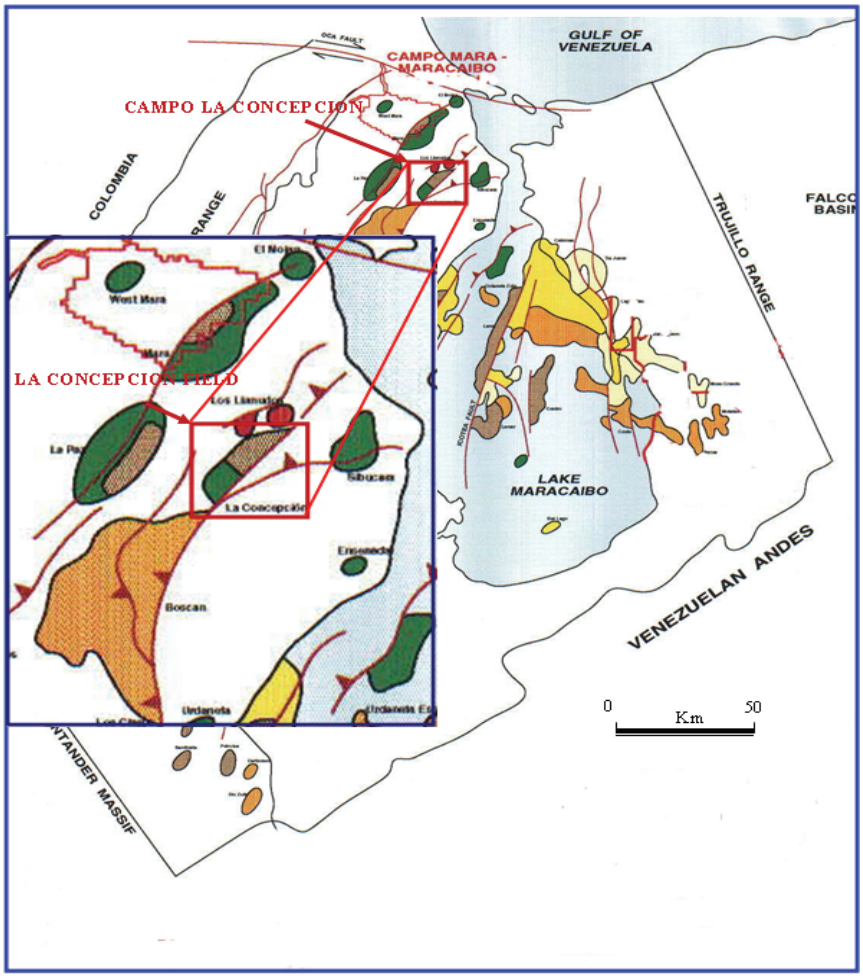

Figure 1.1 Lake Maracaibo oil fields and La Concepcion field, Zulia State, Venezuela (from Gebretsadik, 2005).

a. demux; sample rate 2 ms.

b. geometry.

c. trace edit.

d. gain.

e. phase matching of dynamite and vibroseis.

f. Surface-consistent deconvolution analysis (number of windows:1; operator length: 120 ms; prewhitening: 0.01; window size: 400-3 000 ms @ 0 m / 1 900 – 3200 ms @ 3 200 m CMP sort).

g. stacking velocity analysis: 1st pass.

h. stack; residual static: 1st pass.

i. stacking velocity analysis: 2nd pass; Residual static: 2nd pass.

j. static (trim); velocity analysis for DMO.

k. time variant bandpass: 10-15. 90-110 (0-1 000 ms); 10-15, 60-80 (1 000 – 2 500 ms); 10-15, 40-50 (2 500 – 3 500 ms).

l. FXY predictive deconvolution operator: 5,5 (random noise attenuation and smoothing).

m. Kirchhoff 3D migration.

1.4.2 Borehole Information

The La Concepcion field is rich in borehole information. Below is a list of some of the borehole data:

a. eighteen boreholes with gamma ray (GR) logs and sonic logs in lax format, (Table 1.2). Of these only two are shown in Figure 1.2; they are: C-270 and C - 276, only one is used for this study; it is C-270.

b. nine boreholes with checkshot two-way times (Table 1.2). Of these four are used in this study and are shown in Figure 1.2; they are C-270, C-153, C-152, and C-150.

c. ten boreholes with formation tops (Table 1.2). Of these only six are used in this study and are shown in Figure 1.2; they are C-270, C-276, C-153, and C-152, C-150.

d. one well with bulk density log (Table 1.2 and Figure 1.2); it is C-270.

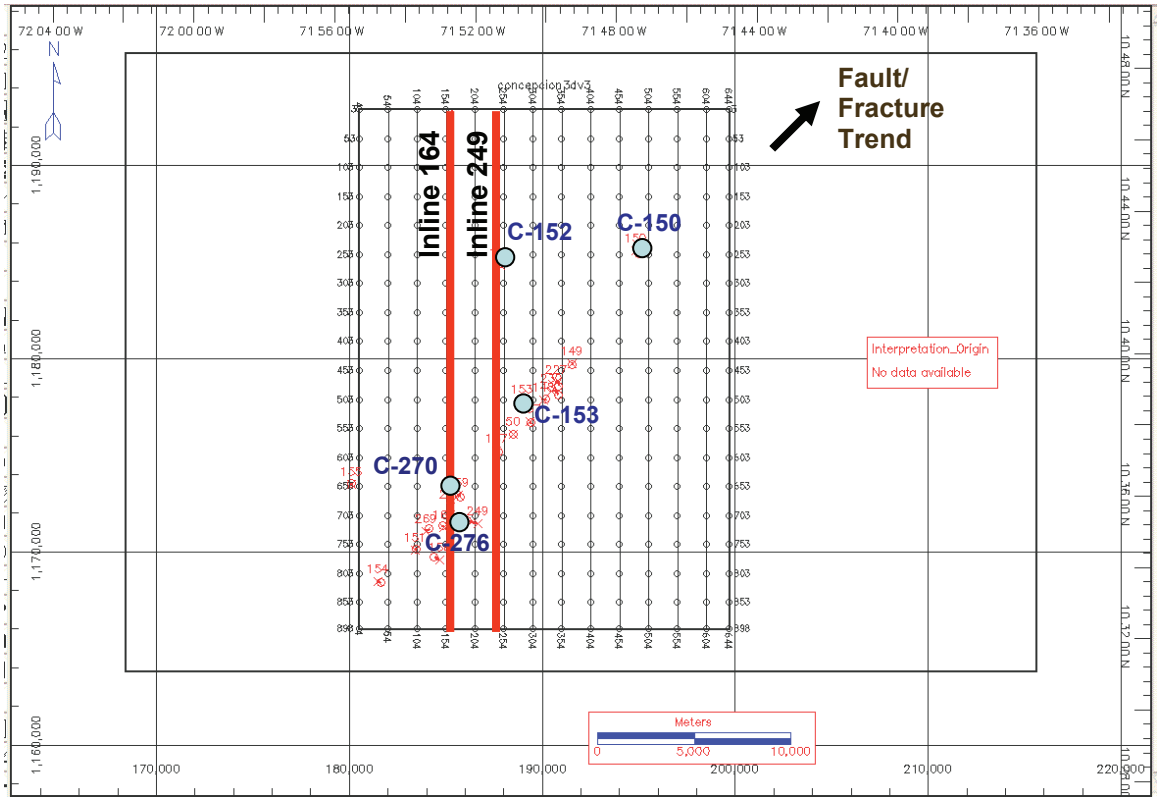

Figure 1.2 Seismic and well location map.

Table 1.1 Field acquisition parameters (from Cardozo, 2001).

Acquisition area	248 km^2
Total SP	9092
Total RP	6671
Bin size	30 x 30 meters
Maximum off-set	3942 meters
Largest min off-set	558 meters
Fold coverage total	44
Fold coverage Inline	8.83
Fold coverage Crossline	5
Source	Dynamite and the Vibroseis
Record time	5 seconds

Table 1.2 Boreholes with gamma ray (GR), sonic logs, density logs, formation tops, and checkshot two-way times.

Name of Wells with GR and Sonic Logs	Name of Wells with Formation Tops	Name of Wells with Checkshots Two-way times	Name of Wells with Density Logs
C-270	C-159	C-150	C-270
C-271	C-162	C-152	

C-276	C-249	C-153	
C-285	C-269	C-230	
C-293	C-270	C-270	
C-302	C-271	C-291	
C-303	C-276	C-294	
C-304	C-285	C-304	
C-305	C-291	C-305	
C-306	C-293		
C-306			
C-309			
C-310			
C-311			
C-312			
C-313			

1.5 Tectonic Setting and Stratigraphy of the Area

1.5.1 Tectonic Setting

The regional geologic setting of the Maracaibo basin can be described by Escalona (2006) as a triangular intermontane depression bounded to the east and west by Merida Andes and Sierra de Perija, respectively, and by the Oca fault the

north (Figure 1.3). The Oca fault is an active right-lateral strike-slip fault, with estimates of Oligocene-Holocene horizontal offset. Figure 1.3 also shows that the Merida Andes to the south and the Bocono faults are bout right-lateral strike-slip faults.

The total volume of accumulated sediment in the Maracaibo basin is estimated to be 250 000 km^3, deposited between the Jurassic and Holocene (Lugo, 1991). Since the middle of the past century, several tectonic models have been proposed to explain the evolution of the Maracaibo Basin. Most of these models agree that the Mesozoic history began with the separation between North and South America which resulted in passive margin formation on both sides (Figure 1.4).

According to Lugo and Mann (1995), three principal tectonic episodes in the geological evolution of the Maracaibo Basin during the Jurassic-Eocene defined as:

1. Jurassic rift, related to the North and South America separation.
2. Passive margin subsidence during the Cretaceous.
3. Foreland basin subsidence type, owing to the oblique collision between the Caribbean plate and the northwest margin of South America.

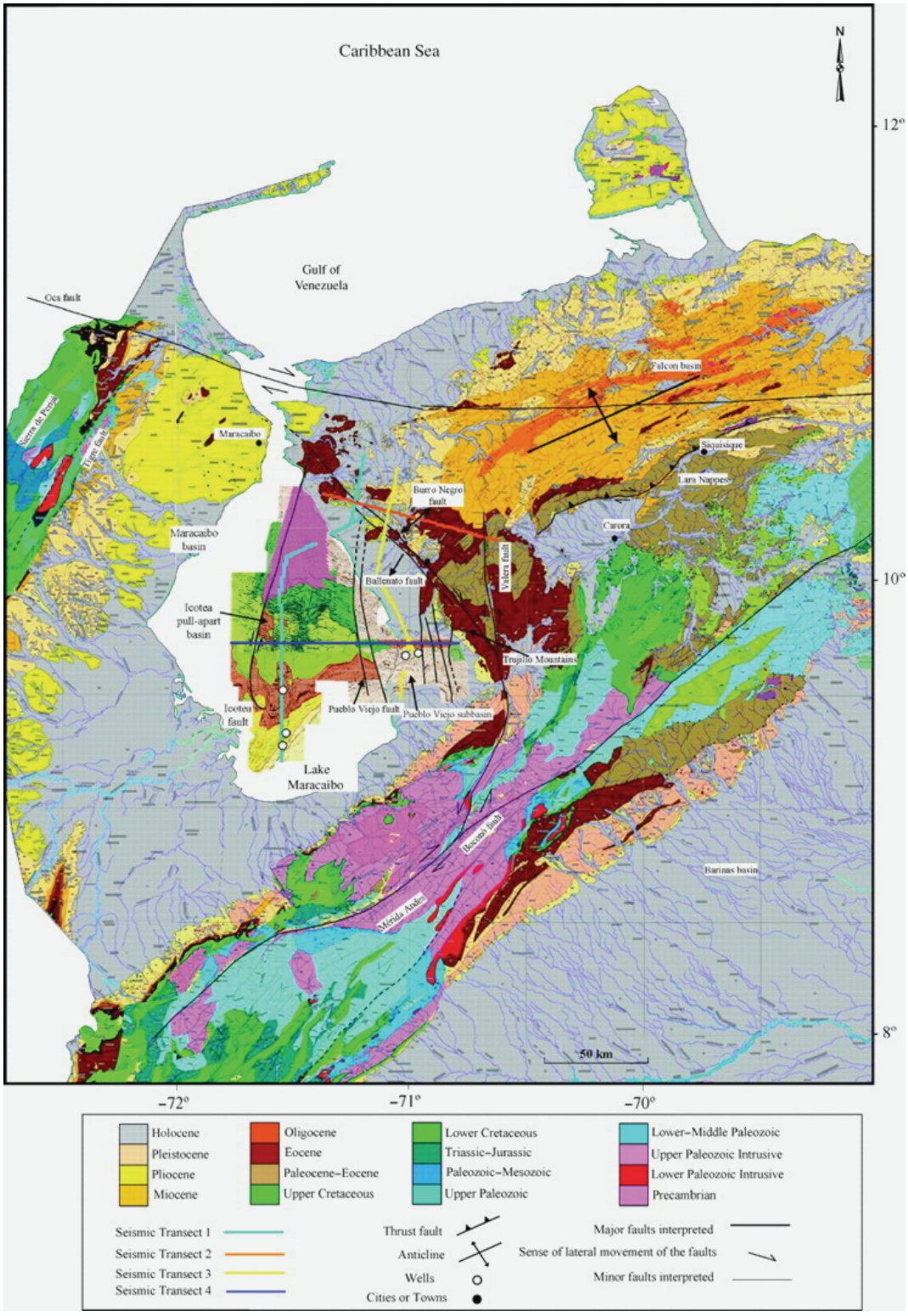

Figure 1.3. Surface geologic map of the Maracaibo Basin region (from Escalona and Mann, 2006).

However, recent work by Hoang (2005) suggests that there were four pulses of tectonics in La Concepcion area which influenced the mechanics of fault formation.

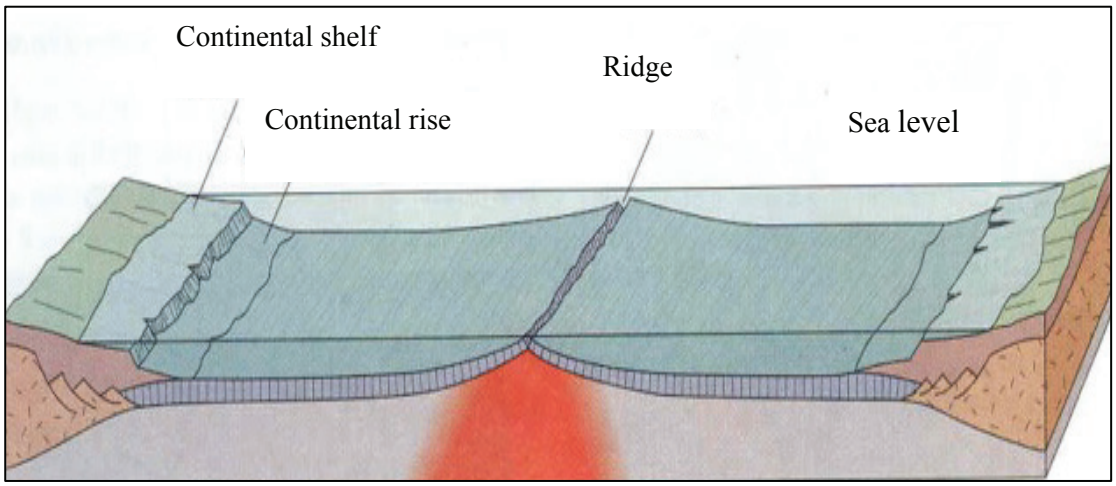

Figure 1.4 Example of passive margin formation (from Cardozo, 2001).

1.5.2 Stratigraphy

The stratigraphic sequences of La Concepcion field were formed during the Cretaceous and Tertiary periods. Figure 1.5 summarizes the formation names, and the paleobathymetric curve constructed by Cardozo (2001) using the marine zonation from Tipsword et al. (1966); and the global sea level curve from Haq et al, (1988). Figure 1.6 shows the lithology and depositional environment of formations in La Concepcion field, Maracaibo Basin.

Based on Figure 1.5, the Cretaceous rock Formations in La Concepcion field include the Rio Negro Formation, the Apon Formation, the Lisure Formation, the Maraca Formation, the G-RN Formation, the Colon Formation, and the Mito Juan Formation.

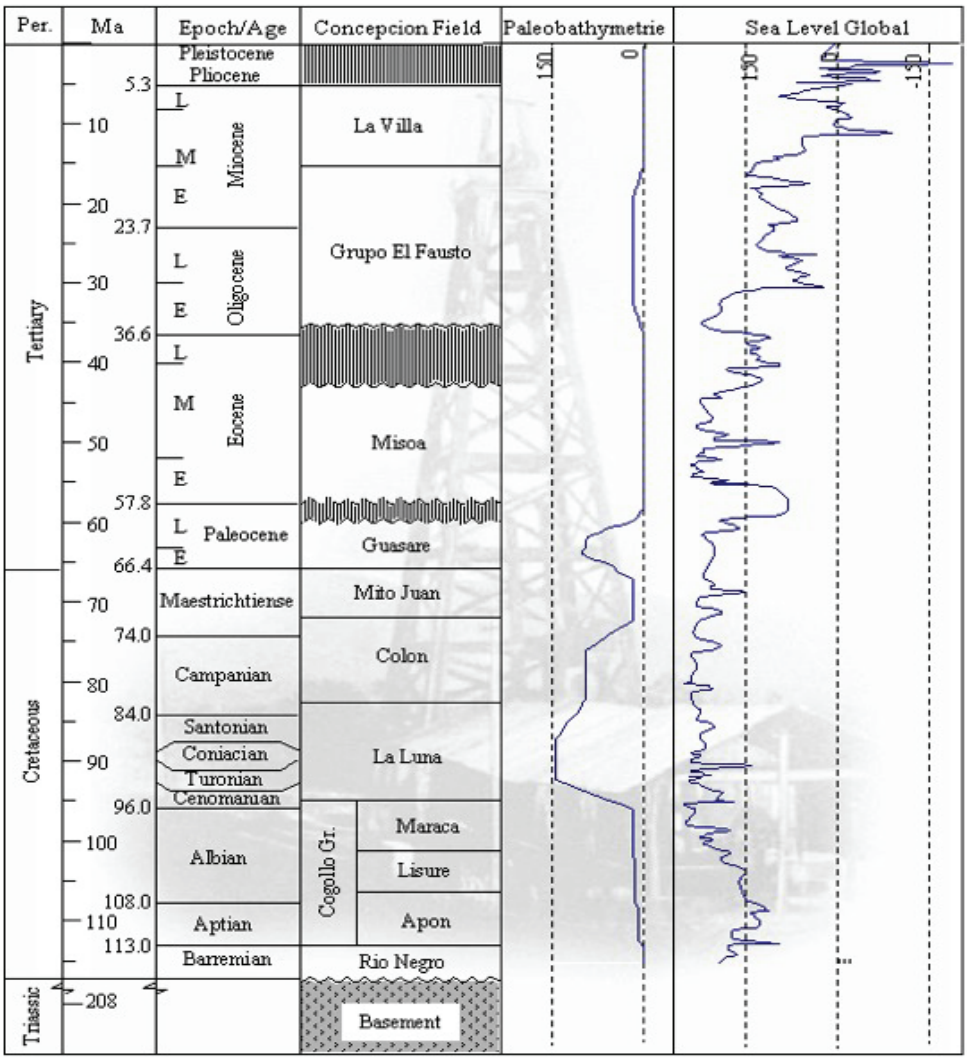

Figure 1.5 Chronostratigraphic chart summarizing the formation names from Cardozo (2001).

AGE	FORMATION	LITHOLOGY	DEPOSITIONAL ENVIRNMENT
Miocene	La Villa	SH, SST	Lacustrine
Oligocene	Gr Fausto	SH	Shallow Marine
Eocene	La Sierra	SST,SH	Coastal lagoon
	Misoa	SST,SH	Shallow Marine, Deltaic
Paleocene	Guasare	LST, SH	Marine
Cretaceous	Mito Juan	SH	Shallow Marine
	Colon	LST, SH	Marine
	La Luna	LST, SH	Marine
	Maraca	LST	Shallow Marine to coastal line
	Lisure	SST, LST	Marine
	Apon	LST, SST	Shallow to deep Marine
	Rio Negro	SST, CGL	Coastal lagoon, Deltaic
Paleozoic	Basement	IgneousMetamorfic	---

Figure 1.6 Lithology and paleoenvironment description for the formations in La Concepcion area (from Cardozo, 2001).

Of the above mentioned Cretaceous rock formations; La Luna Formation has a great geologic importance because of its hydrocarbon potentials. La Luna Formation is composed of fossiliferous limestone and black shales which are very rich in organic material. Therefore, La Luna Formation is the most prolific petroleum source rock in Venezuela (Talukdare et al., 1985) and possibly in the world (West, 1996). According to Hoang (2005), La Luna Formation has the critical properties of a hydrocarbon reservoir, and the generated hydrocarbon might be sealed by the intercalated shales.

The Tertiary rock formations (Figure 1.5) include the Guasare Formation, the Misoa Formation, the El Fausto group, and the La Villa Formation.

Of these Tertiary rock formations, the Misoa Formation (Eocene) is of great importance as a hydrocarbon reservoir. According to Cardozo (2001), the Misoa Formation is basically deltaic and composed of fine-grained to conglomeratic quartz sandstones. Accordingly, the Misoa Formation has good porosity and permeability and is considered as a good hydrocarbon reservoir in La Concepcion field.

As a petroleum source rock and hydrocarbon reservoirs, Guasare Formation and Misoa Formation are of great interest for this research work.

1.6 Strategy and Objectives

There are four principle objectives to this research. Chapter 2 presents some important definitions, concepts, and formulae for calculating seismic attributes and estimating seismic interval velocity and the seismic quality factor, Q_{seismic} using Gaussian function. Basic concepts of depth conversion, and image-ray analysis, and its applications, are described.

The first objective is the precise detection of faults and fractures on the seismic sections. In Chapter 3, recent 3D seismic interpretation includes defining major stratigraphic markers and delineating faults, followed by generating variance cube attributes in order to emphasize the presence of fractures and faults through their characteristics of discontinuities or low coherence.

The second objective is the interval velocity estimation of surface seismic survey using the observed root-mean-square velocity, V_{rms}, at CMP gathers. Chapter 4 introduces 2-D seismic modeling including digitizing an interpreted time-migrated seismic section and conducting depth conversion through layer migration using the image ray method. 2-D seismic modeling is conducted by using the image ray method as a new approach for update the interval velocity.

The third and one of the more important objectives is the prediction of fracture effects on seismic response using scaled velocity interpretation of the velocity measurements and peak frequency as a second new approach. Chapter 5 covers the fracture effects on seismic response of the Arena Sup A – Mb. Areniscas Inferiores (ASA-MAI) Formations and the Guasare – Rio Negro Formations (G-RN) Formations in La Concepcion field through interval velocity analysis and peak frequencies. The researcher applied amplitude-frequency spectrum of Fourier transforms on six selected CMP gathers to estimate the amount of the peak frequencies that occurred as a result of the seismic wave attenuation.

The fourth and fifth most important objectives are: 1) estimating the magnitude of fracture effects on: a) seismic response using: 1) travel-times of seismic wave, b) checkshots, and c) sonic waves through the ASA-MAI Formation and G-RN Formations, and 2) estimating the seismic quality factor, Q_{seismic} A third new approach is developed to estimate the amount this factor. The amount of Q_{seismic} is calculated by modeling the amplitude spectrum of a

signal in the frequency domain using a model for plane wave attenuation. Assuming that the seismic amplitude spectrum of a zero phase wavelet can be calculated using the Gaussian function.

Chapter 6 shows how these effects on seismic response are estimated from traveltime analysis by calculating the total travel-times of the seismic waves of the surface seismic survey and comparing them with the total travel-times of the checkshot seismic waves and the travel-times of the sonic waves through the ASA-MAI Formations and G-RN Formations in order to estimate the amount of the effects on the surface seismic waves only. Chapter 6 also presents the calculated values of the seismic quality factor Q_{seismic} in the fractured zones, fault zone, and non-fractured zones and compares the results in order to estimate the amount of the attenuation on seismic waves in the fracture zones as a result of fractures or saturation effects. Finally, the Q_{seismic} values obtained from seismic data through G-RN Formations are compared with Q_{core} values obtained from well core measurements.

Chapter 7 presents summary and conclusions. The next chapter presents the methodology used in this study.

CHAPTER 2

METHODOLGY

2.1 Seismic Attributes

According to Taner, 2000, seismic attributes are any information obtained from seismic data. These seismic attributes can provide important information relating to the amplitude, shape, and/or position of the seismic waveform.

2.1.1 Complex Trace Attributes

The seismic data is treated is considered as an analytic trace which contains both real and imaginary parts. Different amplitude, phase, and frequency attributes can be calculated. These attributes include instantaneous attributes and response attributes. Instantaneous attributes are associated with a point in time. Response attributes are related to a lobe of the energy envelope *A(t);* they correspond to an event, rather than a single time sample. Figure 2.1 shows complex trace attributes.

2.1.2 Fourier Attributes

According to Nissen (2000), Fourier attributes or frequency domain attributes are obtained through Fourier analysis. These frequency domain attributes may include amplitude variation with bandwidth in frequency (avbf) and spectral decomposition. Fourier attributes are illustrated in Figure 2.2.

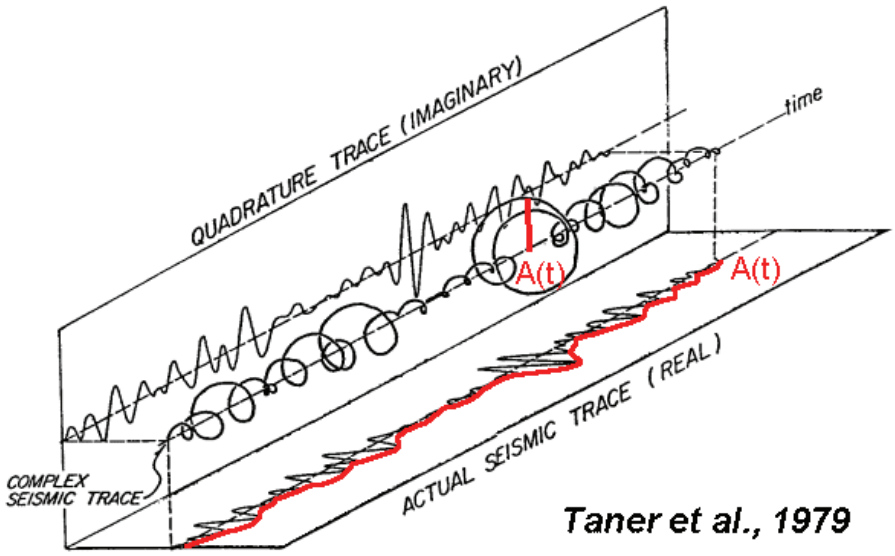

Figure 2.1 Complex trace attributes (Taner and Sheriff, 1979, modified by Nissen, 2002).

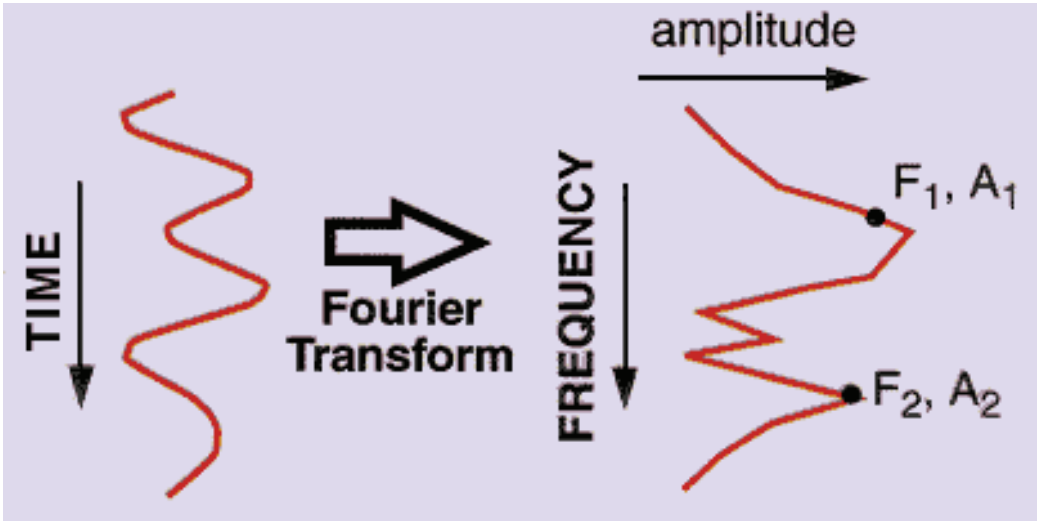

Figure 2.2 Fourier attributes (Nissen, 2002)

2.1.3 Time Attributes

Time attributes are related to the vertical position of the waveform in the seismic section. Time attributes may include horizon time picks and isochrones.

2.1.4 Window Attributes

Window attributes summarize information from a vertical window of data. According to Nissen (2002), Window attributes include: Maximum Absolute Amplitude, Time Maximum Absolute Amplitude, Average Absolute Amplitude, Sum of Absolute Amplitudes, Average Instantaneous Frequency, Number of zero Crossings, Largest Peak/Trough Amplitude Difference, and Largest Peak/Trough Time Difference.

2.1.5 Multi-Trace Attributes

Multi-trace attributes are calculated using more than one input seismic trace, which provides quantitative information about lateral variation in the seismic data. Multi-trace attributes may include coherence and dip/azimuth attributes..

2.1.6 Basic Definitions and Formulae

The complex seismic trace function can be defined using the following formula:

$$C(t) = A(t)e^{i\theta(t)} \tag{2.1}$$

where *A(t)* is the phase independent seismic amplitude or reflection strength, and *(t)* is the phase (Taner, 1979). By Euler's equation,

$$e^{i\theta t} = \cos(\theta(t)) + i\sin(\theta(t)) \tag{2.2}$$

Hence, the complex seismic trace can be divided into a real and an imaginary part. The real part, displayed in the seismic data:

$$r(t) = A(t)\cos(\theta(t)) \tag{2.3}$$

The imaginary part, also called the Hilbert transform, which is simply the real part phase-shifted by 90 degrees:

$$q(t) = A(t)\sin(\theta(t)) \tag{2.4}$$

dividing (2.4) by (2.3), an equation for the phase is obtained.

$$\theta(t) = \arctan\left(\frac{q(t)}{r(t)}\right) \tag{2.5}$$

So the instantaneous phase is the angle that the complex seismic trace makes with the real axis.

Instantaneous attributes may include envelope, instantaneous phase, and instantaneous frequency. Some of these are:

Envelope attribute: $$A(t)=\left(q^2(t)+r^2(t)\right)^{1/2} \tag{2.6}$$

Instantaneous Phase**:** $$\theta(t)=\arctan\left(\frac{q(t)}{r(t)}\right) \tag{2.7}$$

Instantaneous Frequency: $$\omega(t)=\left(\frac{d\theta(t)}{dt}\right) \tag{2.8}$$

Instantaneous attributes are illustrated in Figure 2.3.

Response attributes of the shaded area include:

Response Amplitude: maximum envelope

Response Phase: value of instantaneous phase at time of maximum envelope.

Response Frequency: value of instantaneous frequency at time of maximum envelope.

Response attributes of the shaded area are illustrated in Figure 2.4

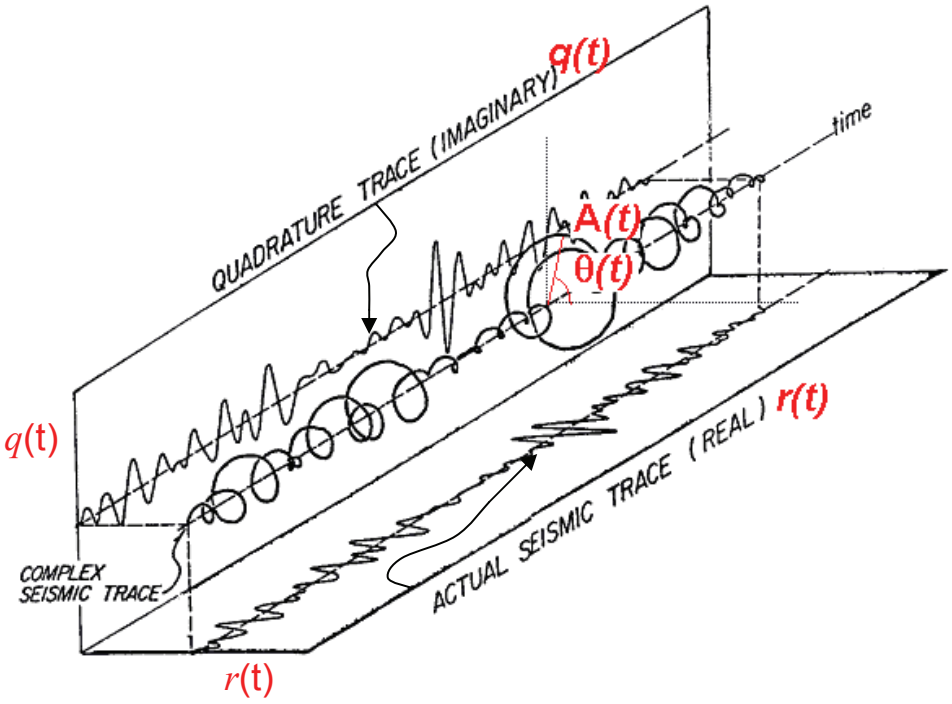

(a)

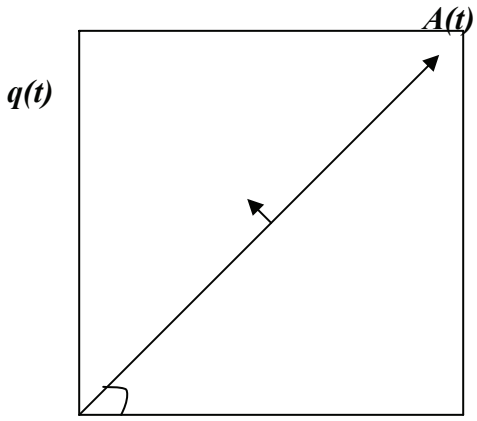

(b)

Figure 2.3 a) Instantaneous attributes (Taner and Sheriff, 1979, modified by Nissen, 2002). b), phasor diagram of a complex seismic trace at time *t* (from Chen, 2002).

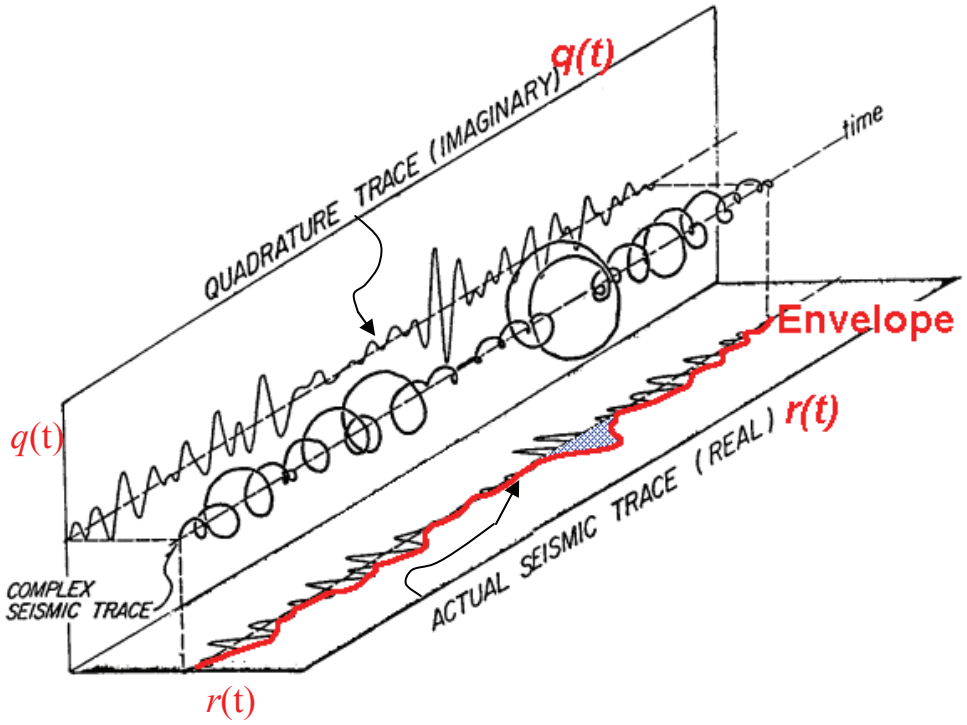

Figure 2.4 Attributes of shaded area (Taner and Sheriff, 1979, modified by Nissen 2002).

Spectral decomposition uses the Fourier transform to calculate the amplitude spectrum of a short time window covering the zone of interest. The amplitude spectrum is tuned by the geologic units within the analysis window, so that units with different rock properties and/or thicknesses will exhibit different amplitude responses. Figure 2.5 shows spectral decomposition.

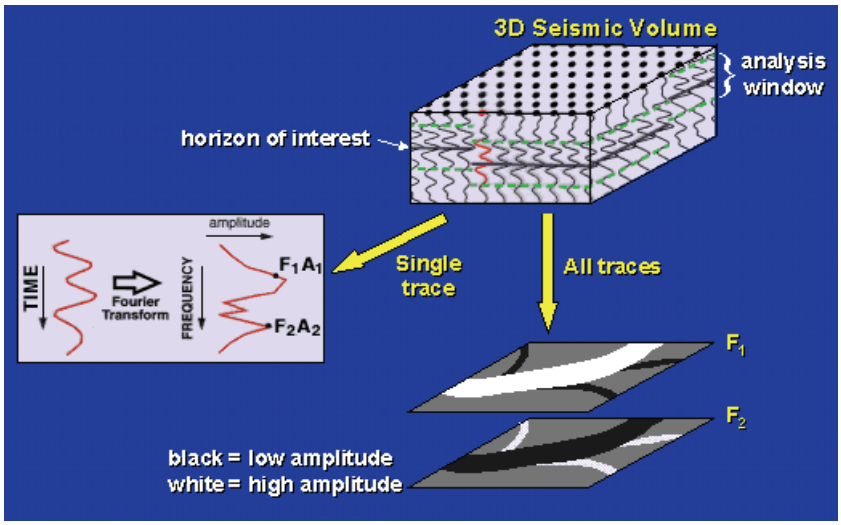

Figure 2.5 Spectral decomposition (from Nissen, 2002).

Seismic coherence is a measure of the trace-to-trace similarity of the seismic waveform within a small analysis window (Niessen, 2002). Figure 2.6 shows seismic coherence.

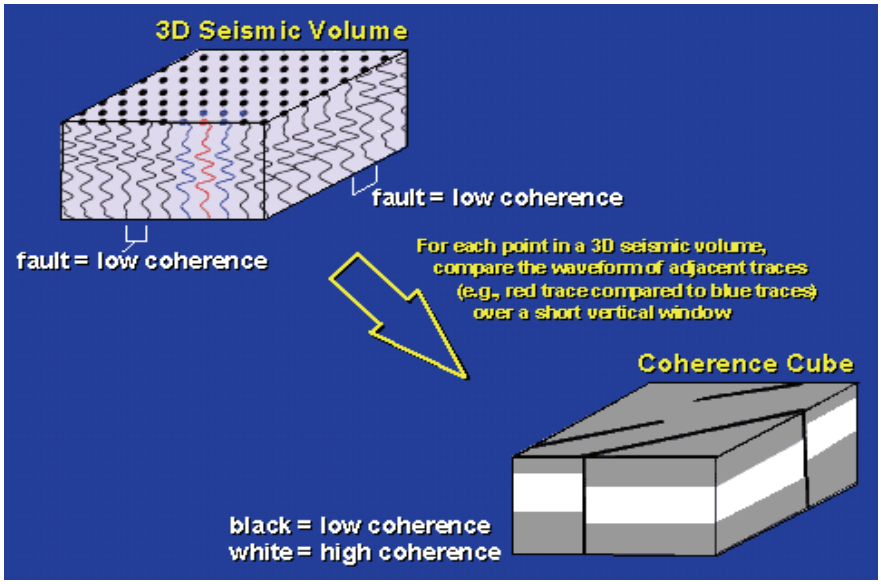

Figure 2.6 Seismic coherence (from Nissen, 2002).

2.1.7 Measuring Coherence

If it is assumed that the reflections are identical on the neighboring traces, the normalized output/input energy ratio can be used as a measure of coherence. This coefficient is the semblance (S_k), (Neidell and Taner, 1971).

The semblance (S_k) can be calculated using the following equation:

$$S_k = \frac{\sum_{j=k-(N/2)}^{k+(N/2)} \left\{ \sum_{i=1}^{M} f_{ij} \right\}^2}{M \sum_{J=k-(N/2)}^{k+(N/2)} \sum_{i=1}^{M} f_{i,j}^2} \tag{2.9}$$

where N is the number of samples in the time gate, M is the number of channels, i and j are channel and time indices, k is the reference time index, and is the real time series. The semblance is defined as the power of the sum divided by the average power of the components of the sum (Taner and Koehler, 1969; Sheriff, 1973).

If we allow the amplitude to change arbitrarily, but we assume the phase to be fixed at a given time, the coherence measure gamma ($_k$) can be used (Gelchinsky et al., 1985) as follows:

$$\gamma_k = \frac{1}{N} \sum_{J=k-(N/2)}^{k+(N/2)} \frac{\sum_{i=1}^{M-1} \sum_{l=i+1}^{M} a_{i,j} a_{lj} \cos\left(\phi_{ij} - \phi_{lj}\right)}{\sum_{i=1}^{M-1} \sum_{l=i+1}^{M} a_{i,j} a_{l,j}} \tag{2.10}$$

where a is the envelope trace, and is the phase. Seismic coherence can be applied in different ways:

1. delineating geological boundaries (faults, lateral stratigraphic contacts, etc.).
2. evaluating large data sets.
3. estimating presence of faults and fractures quantitatively.
4. enhancing stratigraphic information that is otherwise difficult to extract.

The difference between amplitude and coherence is shown in Figure 2.7.

Coherence may be calculated for the entire seismic volume and then a slice can be extracted from the coherence volume at either a constant two-way time or along an interpreted horizon. Alternately, a coherence horizon slice may be calculated from a subset of the seismic volume which has been flattened on the interpreted horizon prior to calculation of coherence. Figure 2.8 shows a schematic representation of three methods for obtaining a coherence slice from a seismic volume.

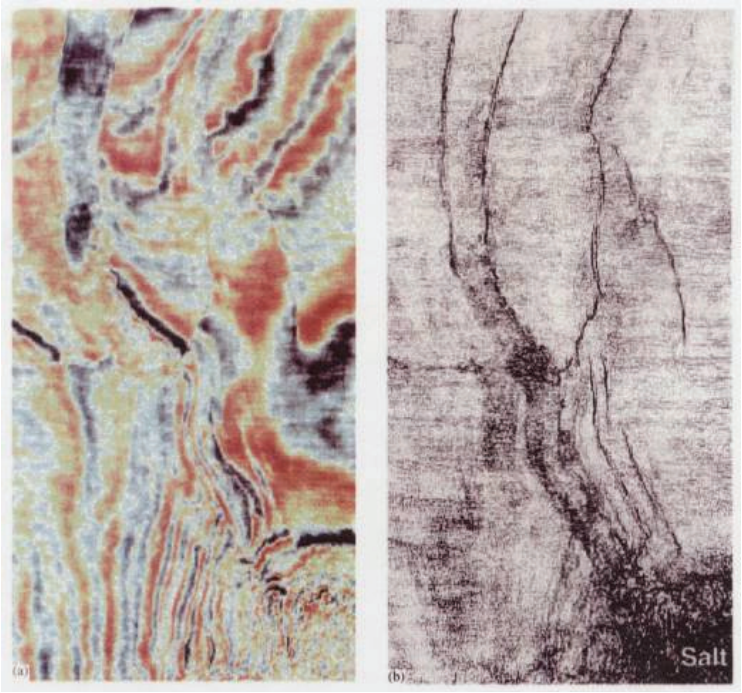

Figure 2.7 Seismic Amplitude (a) and Coherence (b). Note that faults parallel to strikes of the formations are clearly detected on the coherence in (b) (from Bahorich and Farmer, 1995).

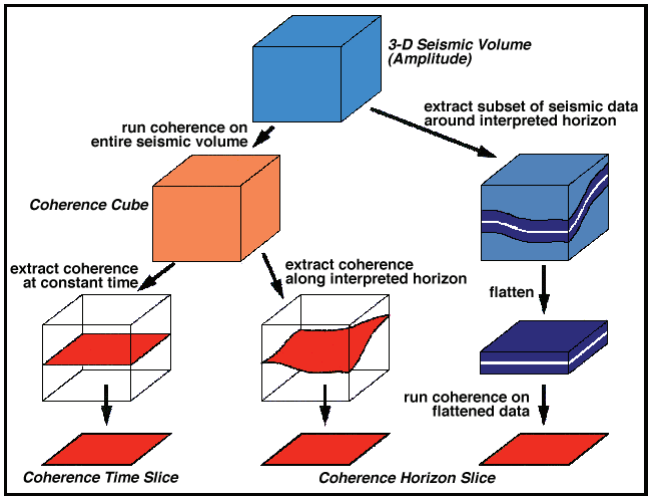

Figure 2.8 Schematic representation of methods for obtaining coherence slice (from Nissen, 2000).

Variance cube attributes are similar to coherence cube attributes. According to Cardozo (2001), the algorithm is a weighted moving variance, calculated at each time sample. The eight traces (Figure 2.9.a) that surround the trace are used, and a number of samples above and below the current sample equals to one-half the variance window length (IESX reference guide, 1998). The parameters and operator type can set up as shown in Figure 2.9. b and c.

This section discusses the different types of seismic attributes, the basic definitions and the methods of measuring coherence. The following section covers the methods of interval velocity estimation.

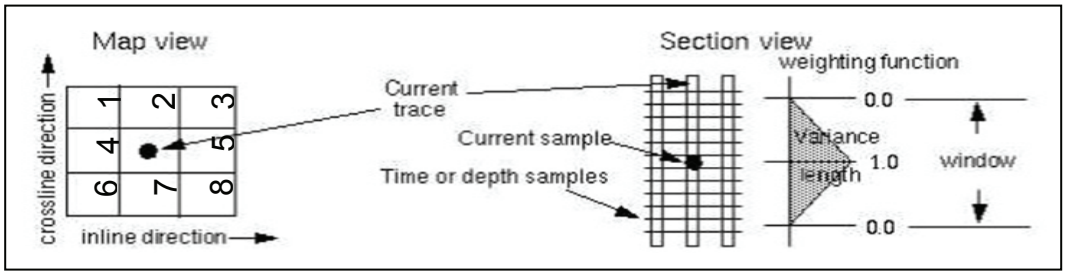

(a)

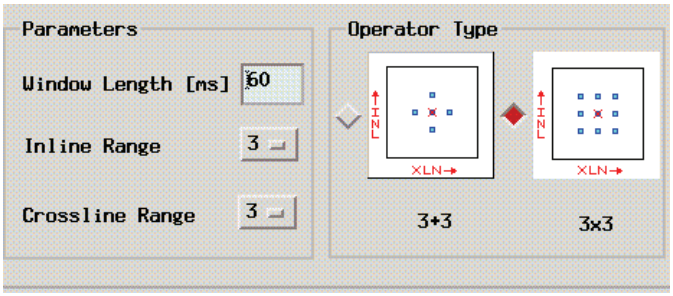

(b)

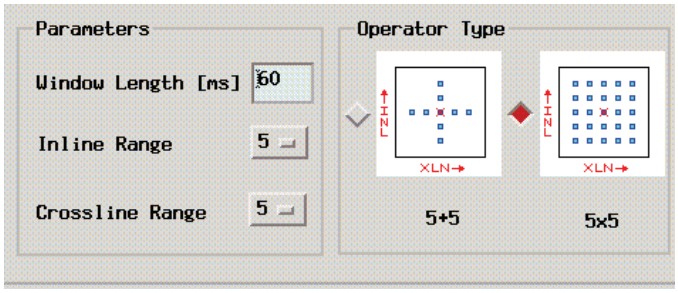

(c)

Figure 2.9 Variance cube operator (from IESX, 1998).

2.2 Interval Velocity Estimation

The Dix equation is a method of calculating the interval velocity from the root-mean square velocity (V_{rms}). The solution of traveltime from source to reflector to receiver (ABCDE) in a multilayer model (Figure 2.10) produces an equation of a two-layer case:

$$T_x^{\,2} = C_1 + C_2 X^{\,2} \tag{2.11}$$

where C_1 is equal to T_o^2 and

$$C_2 = \left(\frac{\sum_{1}^{2} \Delta t_i}{\sum_{i=1}^{2} V_i^{\,2} \Delta t_i} \right) \tag{2.12}$$

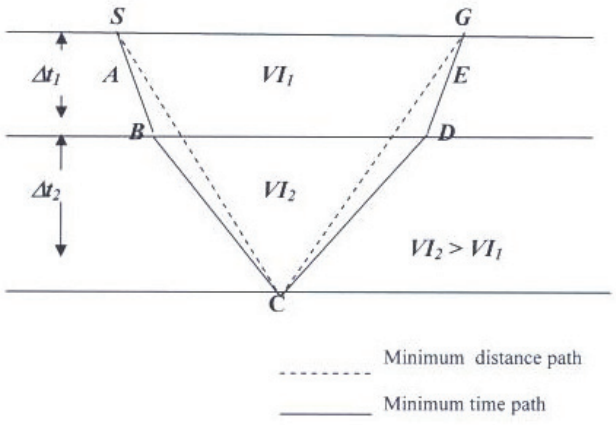

Figure 2.10 Two-layer case velocity model (from Dix, 1955).

Substitute C_1 and C_2 in equation (2.12) to get traveltime:

$$T_x^{\,2} = T_0^{\,2} + \left(\frac{X^2}{V_2^{\,2}} \right) \tag{2.13}$$

According to Taner (1969), Figure 2.11 illustrates that in a multi-layer case, the wavefront is traveling along the shortest time path, in accordance with Fermat's principle, and hence the arrival time will be given by an infinite series of the form:

$$T_{x,n}^{\,2} = C_1 + C_2 X^2 + C_3 X^4 + C_4 X^6 + ... \tag{2.14}$$

where the coefficients C_1 , C_2 **, ….,** depend on layer thicknesses d_1, d_2, …., d_n, and interval velocities $_1$, $_2$, …… $_n$. For the purpose of seismic exploration, all the terms containing high powers of X^2 in equation (2.14) can be neglected, which simplifies the expression to,

$$T_{x,n}^{\,2} = C_1 + C_2 X^2 \tag{2.15}$$

where

$$C_1 = \left(\sum_{k=i}^{n} t_k \right)^2 = T_{0,n}^{\,2} \tag{2.16}$$

and

$$C_2 = \left(\frac{\left(\sum_{k=1}^{n} t_k \right)^2}{\sum_{k=1}^{n} t_k v_k^{\,2}} \right) = V_n^{\,2} \tag{2.17}$$

$$V_n^{\,2} = \left(\frac{\sum_{k=1}^{n} t_k v_k^{\,2}}{T_{0,n}} \right) \tag{2.18}$$

Therefore, equation (2.15) becomes:

$$T_{x,n}^{\,2} = \left(\frac{T_{0,n}^{\,2} + X^2}{V_n^{\,2}} \right) \tag{2.19}$$

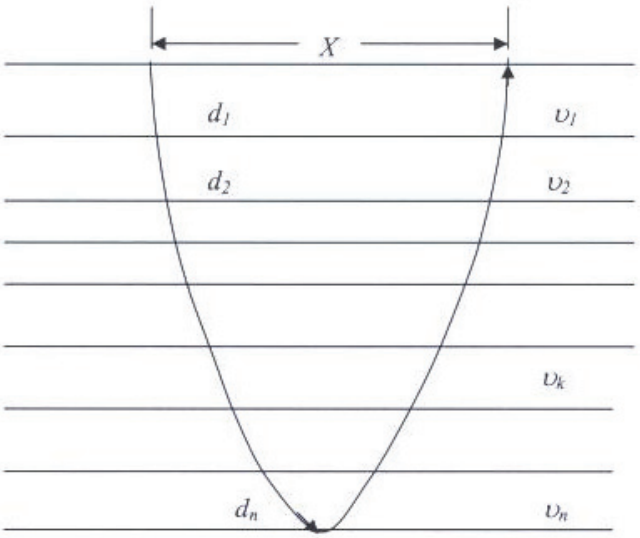

Figure 2.11 Snell's Law ray analysis in horizontally layered medium (from Taner, et. al., 1969).

If equation (2.19) is differentiated with respect to X^2, the slope $\left(\frac{dT_x^2}{dX^2}\right) = C_2$ at $X^2 = 0$. Thus, if T^2_x is plotted versus X^2, the slope of the plot at $X^2 = 0$ is the quantity C_2. The square root of the inverse of the quantity C_2 is recognized as the interval-time-weighted root-mean-square of the interval velocities and is called V_{rms}. For horizontal layers and short distances, $V_{rms} = V_{nmo}$. But for a large distance X, the terms higher than X^2 become more and more significant and a linear fit in the X^2, T^2 domain will not produce a V_{nmo} that is approximately V_{rms} (Amery, 1993). So for short source-receiver distances (offsets), where V_{nmo} approximates V_{rms}, this relationship may be used to determine interval velocities.

If the maximum offset distance (X_{max}) is less than the depth to the reflectors at the top and base of an interval, the interval velocity may be determined. Applying equation (2.18) for V_{rms} to the top and base of the bed gives the following:

$$V^2_{rms(n-1)} T_{0,n-1} = \sum_{k=1}^{n} t_k v^2 \qquad \text{(top)} \qquad (2.20)$$

and

$$V^2_{rms(n)} T_{0,n} = \sum_{k=1}^{n} t_k v^2_k \qquad \text{(base)} \qquad (2.21)$$

If equation (2.20) is subtracted from equation (2.21), the interval velocity may be estimated as follows:

$$V_{\text{int}} = \sqrt{\frac{V^2_{rms(n)} T_{0,n} - V^2_{rms,n-1} T_{0,n-1}}{T_0 - T_{0,n-1}}} \tag{2.22}$$

Equation (2.22) is referred to as the "Dix equation." Applying the Dix equation to perform calculations for all intervals between primary reflections permits the construction of a time-depth plot similar to the time-depth plot from the well velocity survey (Amery, 1993).

The travel-times (T) of the sonic log and seismic waves of checkshots or surface seismic surveys through a formation can be estimated by the integration over the depth (z) from top (a) to bottom (b) of such a formation as follows:

The total time $$T = \int_a^b \Delta t dz \tag{2.23}$$

$$= \Delta t_{aveg} \left(\frac{\mu \sec}{ft}\right) \int_a^b dz$$

$$= \Delta t_{aveg} \left(\frac{\mu \sec}{ft}\right)(b-a)(ft)$$

$$= T\ (\mu . \sec\ )$$

where Δt_{aveg} is the one-way time rate through the formation thickness $(b - a)(ft)$. Equation (2.23) was used to calculate the total travel-times of the

sonic, checkshot, and seismic waves through ASA-MAI and G-RN Formations of La Concepcion field.

2.3 Depth Conversion

An earth imaging in depth can be obtained by first migrating a stacked section in time and converting the time-migrated section to depth along image rays using the approximate velocity-depth model (Hubral, 1977). Secondly, tracing the image ray from the surface on a depth model enables a lateral correction and a time-to-depth conversion from which samples in time-migrated sections may be moved to approximate a depth migration. Figure 2.12 illustrates the flowchart of the depth conversion using image ray.

2.4 Image Ray Application

The image ray is one of the significant rays in reflection seismology. The image ray was first recognized by Hubral (1977), who suggests that the image rays are vertical at the earth's surface. They can be associated with the minimum travel-time from the diffractor point to the earth's surface.

According to Hubral (1977), the ensemble of rays connecting D (Figure 2.13) with points on the surface of the earth includes two rays of special importance. One is the normal ray and the other is the ray emerging normally to the earth's surface which is the image ray. In migration, the primary reflection

element at time TN is mapped (moved or migrated) into an output element at time TM.

The image ray plays an important role in the theory of seismic imaging or time migration. Time-migration algorithms leave a residual error caused by simplifying assumptions. This error can be predicted by using the image rays. The image ray describes the subsurface locations from which scattered energy is received.

The lateral shift between the point of departure of the image ray at the reflector position and the point of the emergence of the image ray at the surface distance A-B in Figure 2.14 provides a measure of lateral velocity variation.

The image ray represents the apex (minimum time) of the diffraction, and time migration collapses energy to this point. Figure 2.15 (a) shows a point diffractor buried in a layered medium. Raypaths from the scatterer to the surface are bent at the interface between the first and second layers according to Snell's Law of Refraction. The image ray emerges at midpoint 240 with no shift. The zero-offset section is approximately hyperbolic as shown in Figure 2.15 (b). The velocity associated with this approximate hyperbola is the rms velocity (V_{rms}) down to the diffractor.

According to Yilmaz (2001) it is reasonable to assume that the zero-offset traveltime trajectory for a point diffractor in a horizontally layered earth model is a hyperbola. The apex of this approximate hyperbola coincides with the arrow as shown in Figure 2.15. In this case, there is no lateral velocity variation due to the

dipping boundary and, therefore, only time migration is needed to image a diffractor that is buried in a horizontally layered earth model. The result of time migration is shown in Figure 2.15 (c).

The image ray may bend in areas with lateral velocity variation but will arrive normal to the surface. Figure 2.16 (a) illustrates a point diffractor situated in the third layer. The travel-time trajectory is skewed so that *A* does not coincide with the lateral position *B* of the diffractor as shown on the zero offset section [Figure 2.16 (b)]. Note that the apex of the skewed traveltime trajectory *A* coincides with the surface position of the ray that emerges vertically. The image ray associated with the point diffractor in Figure 2.16 (a) is roughly at midpoint 200, but the diffractor itself is located beneath midpoint 240. Therefore, the lateral shift is equivalent to 40 midpoints. This shift occurs because there is lateral velocity variation. Therefore, depth migration is required. The results of time migration and depth migration are shown in Figures 2.16 (c) and 2.16 (d). The following section deals with spectrum evolution.

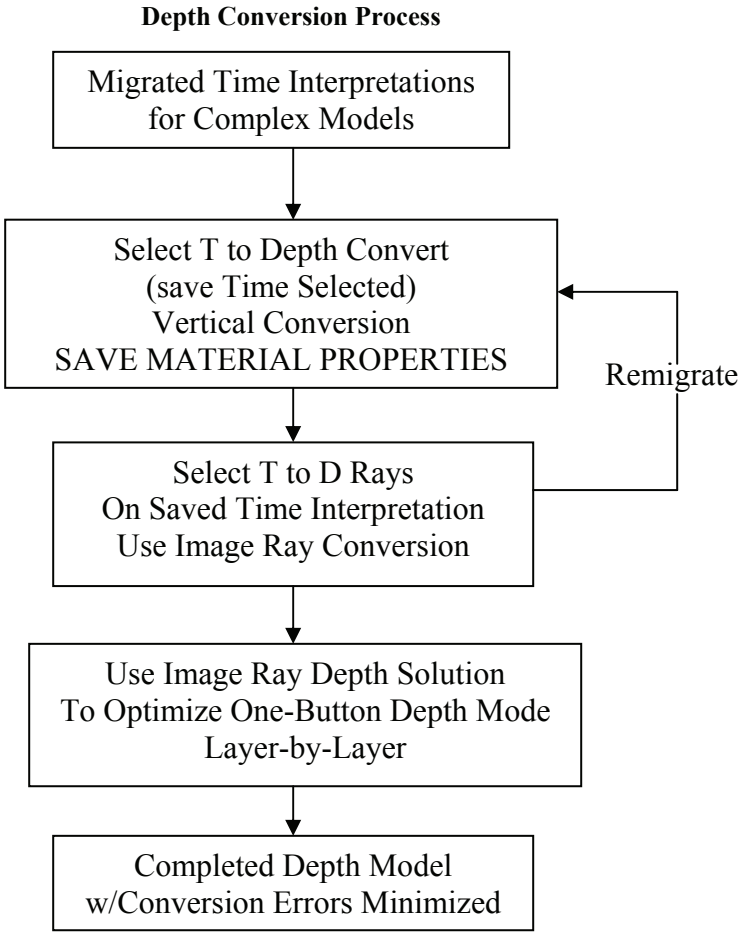

Figure 2.12 Flowchart for depth conversion using the image ray (from GX II User's Guide, 1995).

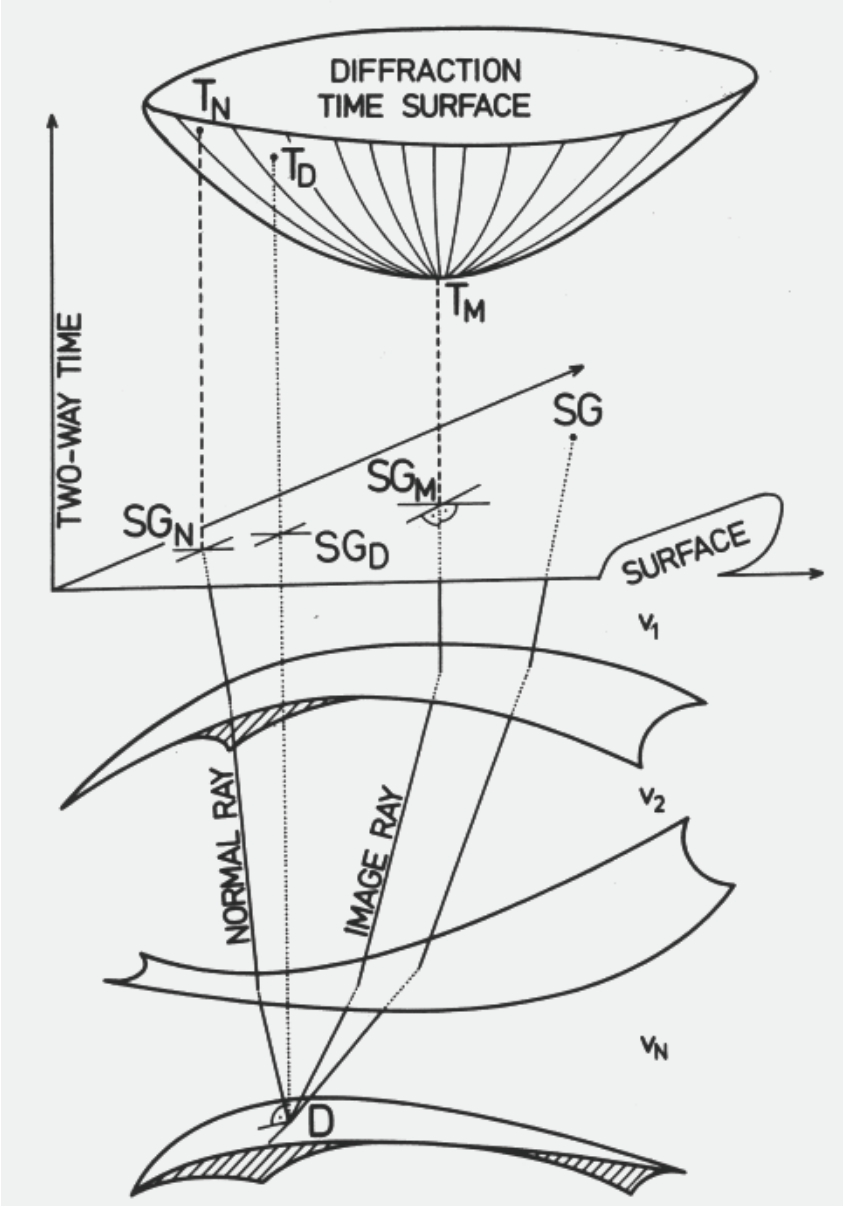

Figure 2.13 3-D curved layer model featuring a normal ray, image ray, and diffraction time surface for point scatterer D (from Hubral, page 85, 1977).

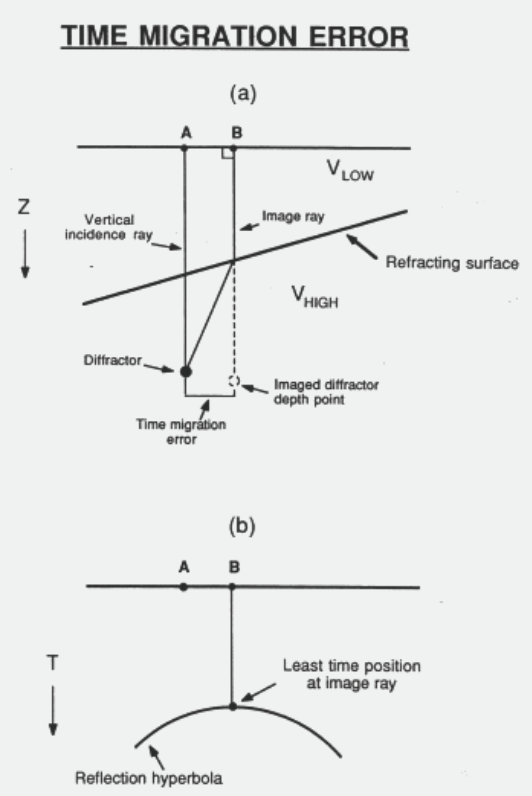

Figure 2.14 (a) Schematic illustrating the time-migration error as represented by the image ray. (b) Diffraction hyperbola associated with arrival diffractor. The image ray defines the least-time travel path from diffractor to recording surface (from Fagin, page 23, 1996).

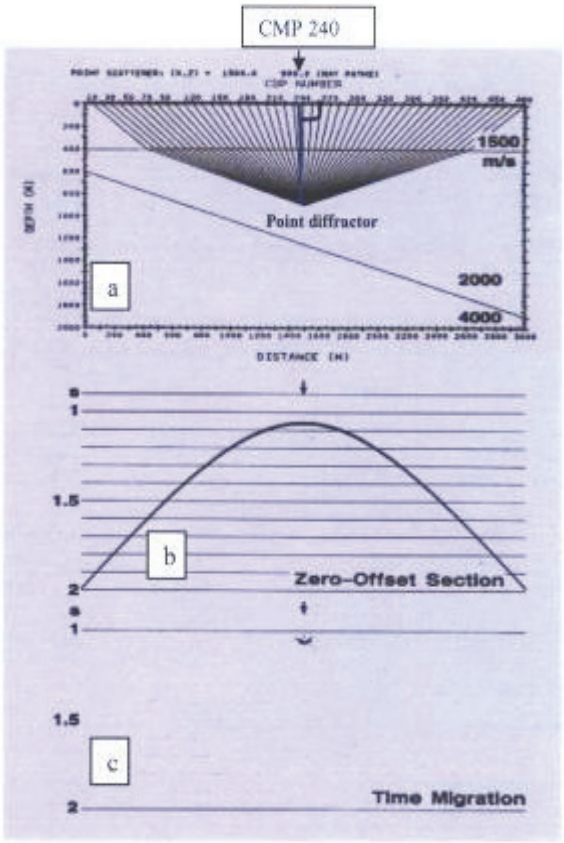

Figure 2.15 Response of a point diffractor in a layered medium (a) is approximately a hyperbola (b). Note that the image ray emerges vertically at the surface at midpoint 240 with no shift. Time migration (c) is adequate for imaging the diffractor. The arrows indicate surface projection of the lateral position of the diffractor (from Yilmaz, page 1223, 2001, emphasis added).

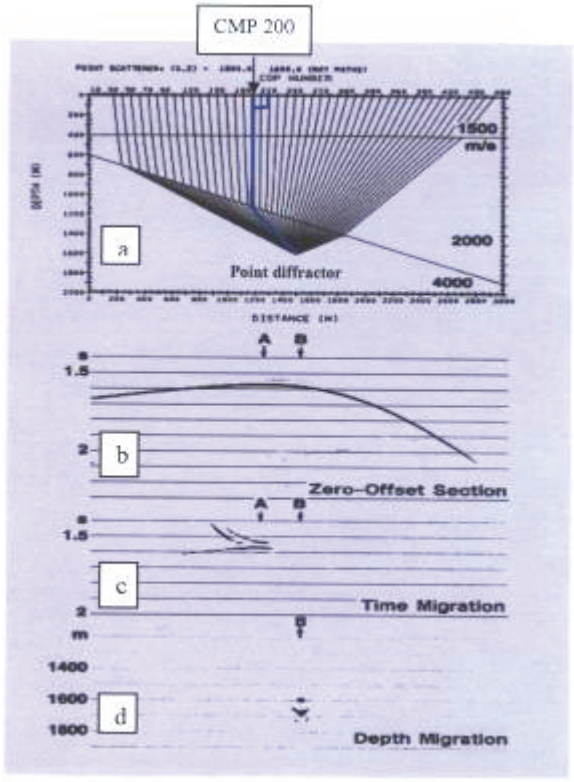

Figure 2.16 The response of a point diffractor buried in a medium with strong lateral velocity variation (a). (a) is skewed hyperbola with its apex shifted to the left of the true position (b). Note that the image ray emerges vertically at the surface at midpoint 200. Time migration (c) no longer is a valid process; instead, depth migration (d) is needed (from Yilmaz, page 1224, 2001, emphasis added).

2.5 Spectrum Evolution

The evolution of the amplitude spectrum of a signal can be modeled in the frequency domain plane wave attenuation. Assume that the seismic amplitude spectrum of a zero phase wavelet can be calculated using the Gaussian function. The Gaussian function can be defined as:

$$F(x) = ae^{-\frac{(x-b)^2}{c^2}} \tag{2.24}$$

where a, b, and c are constants and x is variable.

Equation (2.24) can be applied in estimating a seismic wavelet as follows:

$$W_o = ae^{-\frac{(F-Fp)^2}{\sigma^2}} \tag{2.25}$$

where a, F_p, and are the constants and represent the amplitude, peak frequency, and half width respectively, and F is the variable frequency. This assumes that F(x) is composed of W (the wavelet) and R (the reflectivity), where R must be random in time and white in amplitude.

At zero distance ($r_o = 0$) the amplitude a is considered to be un-decayed, then the wavelet W_o can be estimated as:

$$W_o = ae^{-\frac{(F-Fp)^2}{\sigma^2}} \tag{2.26}$$

This plots as:

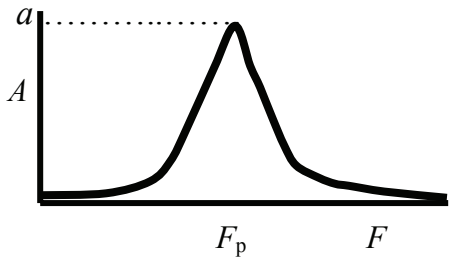

For a distance r_1, the wavelet amplitude decays by a factor ($\frac{-\pi F}{QV}$), then the wavelet W_1 is:

$$W_1 = W_o e^{-\frac{(F-Fp)^2}{\sigma^2}} e^{\frac{-\pi F}{QV_1} r_1} \tag{2.27}$$

This plots as:

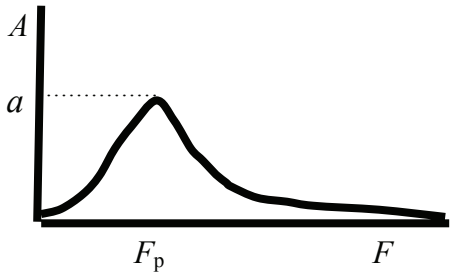

where Q is the seismic quality factor and V is the wave propagation velocity.

Similarly,

$$W_2 = W_1 e^{-\frac{(F-Fp)^2}{\sigma^2}} e^{\frac{-\pi F}{Q_2 V_2} r_2} \tag{2.28}$$

This plots as:

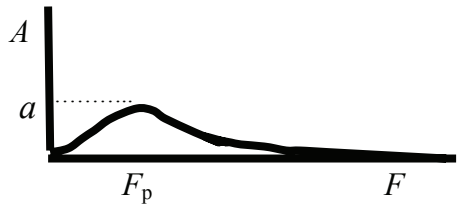

and

$$W_3 = W_2 e^{-\frac{(F-Fp)^2}{\sigma^2}} e^{\frac{-\pi F}{Q_3 V_3} r_3} \tag{2.29}$$

This plots as:

Generally, a wavelet at a distance r_n can be estimated as:

$$W_n = W_{n-1} e^{-\frac{(F-Fp)^2}{\sigma^2}} e^{\frac{-\pi t F}{Q n V_n} r_n} \tag{2.30}$$

One of the applications of equations (2.27-2.30) is calculating the seismic quality factor Q within a certain stratigraphic formation using the shifts in the peak frequency of the signals. The amplitude variations are modified by the seismic gain but the peak frequency is not.

In this section, a detailed study about seismic attributes and their applications, methods of estimating interval velocity and calculating the quality factor Q from seismic was presented. The following chapter deals with the three-dimensional seismic interpretation and applications of seismic attributes.

CHAPTER 3

3-D SEISMIC INTERPRETATION

The main purpose of conducting 3-D seismic interpretation in this area of study is to, first, emphasize the presence of faults and fractures associated with the seismic response of the ASA-MAI Formations, and G-RN Formations of La Concepcion field, and secondly, prepare an interpreted 2-D seismic time section to be used for 2-D seismic modeling that is discussed in detail in chapter three. This chapter presents two sections: picking horizons and defining faults followed by seismic attributes.

3.1 Picking Horizons and Defining Faults

For the purpose of conducting a 3-D seismic interpretation, a number of in-lines and crosslines were selected among the entire 3-D volume shown on the location map (Figure 1.2). Table 3.1 illustrates the selected inlines and crosslines to be used in this research.

The formation tops recorded at the Borehole C-270 are shown in Table 3.2. Tables 3.3 through 3.6 illustrate checkshot information of the Boreholes C-270, C-150, C-152, and C-153. Among the stratigraphic major markers which are recorded at these boreholes, only three formation tops of seismic sequences on the inline 164 (Figure 3.1) and crossline 703 **(**Figure 3.2) were selected and correlated

with the formation tops that are recorded at the Boreholes C-270, C-150, C-152, and C-153.

Table 3.1 The selected inlines and crosslines**.**

Inline	Cross line
100	21
148	69
164	117
180	141
228	189
244	261
260	272
276	309
262	405
308	508
340	645
365	653
372	703
388	717
404	813
419	...

Table 3.2 Stratigraphic major markers (Tops) at the Borehole C-270. Important information in bold.

Formation Name	Name of Interpreter				
	CONK	DMA	PECOM	VIMG	EOCEN
	DEPTH (ft)	DEPTH (ft)	DEPTH (ft)	DEPTH (ft)	DEPTH (ft)
TOPE ARENA BASAL MIOCENE	802.49	806.99			
TOPE EOCENO	892.51	884.37	892.51	907.56	
ARENA SUP A	**1992.97**	1999.22	1992.97	1384.03	1983.37
ARENA SUP B		2228.48		1987.93	2232.57
ARENA SUB C	2470.54	2545.09		2542.35	2815.76
ARENA SUP D	2769.35	2825.28			2978.14
ARENA SUP E		3018.15			3252.05
ARENA SUP F					3465.83
TOPE Mb. RAMILLETE	3612.34	3612.35	3612.34		3610.2
TOPE Mb. PUNTA GORDA	3767.4	3767.41	3767.4		3757.64
PG. 5					4132.56
PG. 4					4174.73
PG. 3					4264.24
PG. 2					4340.58
PG. 1					4412.83
TOPE Mb. ARENISCAS INFERIORES	4507.78	4507.79	4507.78		4508
TOPE GUASARE	**7410**	7410	7110		
TOPE MITO JUAN	8305.33	8305.33	8305.33		
TOPE Mb. SOCUY	10156.7	10156.7	10154		
TOPE LA LUNA	10273.85	10273.83	10273.85		
TOPE MARCA	10592.91	10592.9	10593		

TOPE LISURE	10682.86	10682.86	10899.3		10685.16
TOPE APON	11057.62	11057.62	11540.34		11092.68
TOPE Mb. PICHE	11058.75				
TOPE Mb. MACIQUES	11554.49	11554.49			11556.33
TOPE Mb. TIBU	11595.18	11595.18			11596.31
TOPE RIO NEGRO	11712	11712	11712		
TOPE BASEMENTO	**11742**	11742	11742		

Table 3.3 The Borehole C-270 checkshot two-way times.

Depth (ft)	Two-Way Time (m.sec)	Depth (ft)	Two-Way Time (m.sec)	Depth (ft)	Two-Way Time (m.sec)	Depth (ft)	Two-Way Time (m.sec)
0.00	0.00	3194.80	831.40	4861.70	1143.80	7743.60	1597.60
504.00	198.40	3244.40	841.80	4959.00	1161.00	1605.00	7792.50
554.00	210.60	3293.90	851.20	5007.60	1169.40	7939.30	1628.60
654.00	234.20	3343.40	859.80	5056.20	1177.40	7988.20	1635.60
1003.50	328.60	3392.90	869.40	5104.80	1186.00	8086.10	1652.20
1053.40	340.80	3491.80	889.60	5153.40	1194.20	8233.00	1674.00
1103.30	354.20	3541.20	899.20	5202.00	1202.60	8282.00	1681.00
1153.20	366.40	3590.50	908.40	5396.10	1236.40	8429.00	1705.60
1502.30	454.20	3639.90	918.40	5494.00	1252.20	8674.00	1745.20
1552.10	464.20	3689.20	928.20	5543.10	1260.20	8771.90	1763.00
1601.90	476.80	3738.40	938.60	5592.30	1268.00	8820.90	1771.80
1651.70	490.60	3787.60	948.20	5838.80	1307.80	8918.80	1789.00
2000.30	571.00	3836.70	957.20	5887.90	1316.20	9653.70	1923.80
2050.10	582.40	3885.80	967.00	6084.00	1350.20	10140.00	1985.00
2100.00	592.60	3934.70	976.00	6132.90	1357.80	10188.90	1990.40
2149.80	604.00	3983.60	985.00	6279.00	1380.20	10384.60	2012.40
2498.40	683.20	4032.50	994.60	6376.60	1396.00	10482.60	2022.80

2548.20	694.40	4130.20	1012.40	6523.00	1419.40	10678.90	2042.20
2598.10	706.00	4179.00	1022.00	6668.90	1443.00	10924.60	2066.00
2647.90	716.60	4276.50	1040.00	6815.10	1465.20	11170.70	2092.80
2747.40	739.00	4325.20	1048.80	6863.90	1472.60	11367.90	2115.60
2797.40	749.20	4374.00	1057.80	6961.50	1487.40	11463.60	2125.80
2847.00	759.20	4422.70	1066.60	7059.20	1502.00	11664.80	2146.00
2896.70	770.00	4471.50	1075.40	7205.90	1522.40		
2946.50	780.60	4520.30	1084.20	7254.80	1529.20		
2996.20	791.00	4569.10	1092.60	7303.70	1536.00		
3045.90	801.20	4666.60	1109.20	7352.60	1542.80		
3095.60	811.20	4715.30	1118.00	7450.40	1556.40		
3145.20	821.00	4764.10	1126.60	7645.80	1582.80		

Table 3.4 The Borehole C-150 checkshot two-way times.

Depth (ft)	Two Way Time (msec)	TWT + shift (msec)
0	0	0
600	192	196
1180	336	340
1700	464	468
2180	584	588
2680	696	700
3180	816	820
3650	920	924
4150	1020	1024
4600	1104	1108
4890	1168	1172
5100	1208	1212
5650	1312	1316

6150	1376	1380
6650	1460	1464
7100	1544	1548
7650	1616	1620
8100	1696	1700
8600	1784	1788
9150	1856	1860

Table 3.5 The Borehole C-152 checkshot two-way times.

Depth (ft)	Two Way Time (msec)	TWT + shift (msec)
0	0	0
500	120	192
1000	240	312
1500	360	432
2000	460	532
2500	580	652
3000	680	752
3500	800	872
4000	900	972
4500	1020	1092
5000	1100	1172
6000	1260	1332
7000	1420	1492
8000	1560	1632
9000	1720	1792
10000	1880	1952
11000	2000	2072
12000	2120	2192

Table 3.6 Checkshot two-way times at the Borehole C-153.

Depth (ft)	Two Way Time (msec)	TWT+shift (msec)
0	0	0
784	200	223.33
1784	420	443.33
2784	600	623.33
3284	728	751.33
3784	816	839.33
4283	918	941.33
4783	998	1021.33
5282	1074	1097.33
5782	1150	1173.33
6280	1232	1255.33
6777	1304	1327.33
7334	1386	1409.33
7754	1440	1463.33
8246	1516	1539.33
8732	1584	1607.33
9211	1668	1691.33
9704	1738	1761.33
10303	1832	1855.33
10988	1950	1973.33
11243	1980	2003.33
11503	2010	2033.33

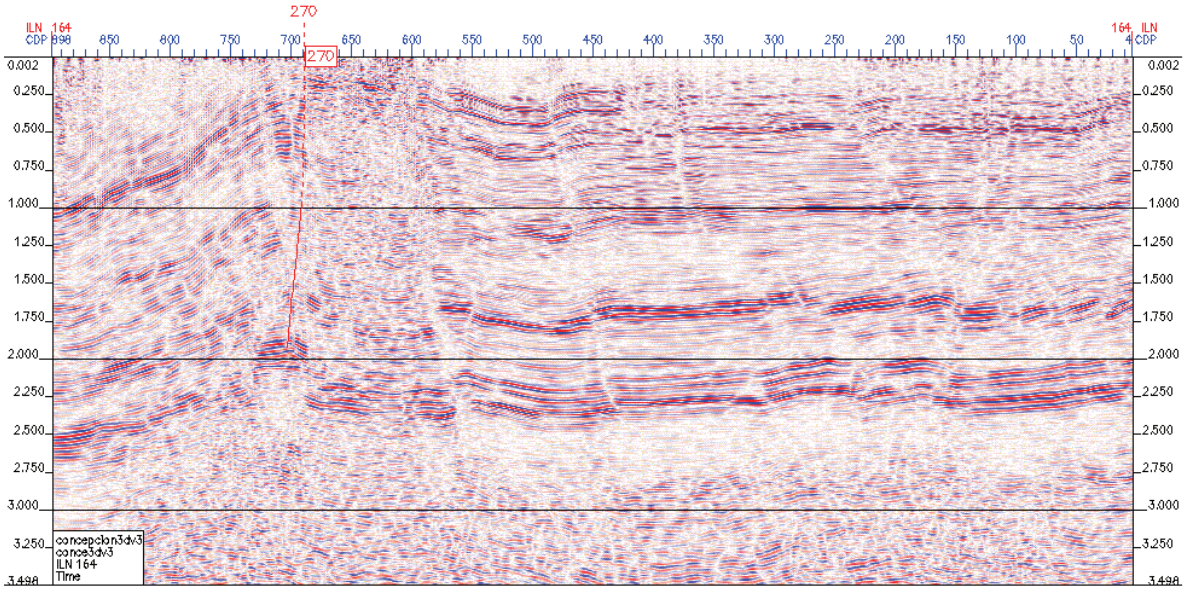

Figure 3.1 Pre-interpreted inline 164 and the Borehole C-270 location.

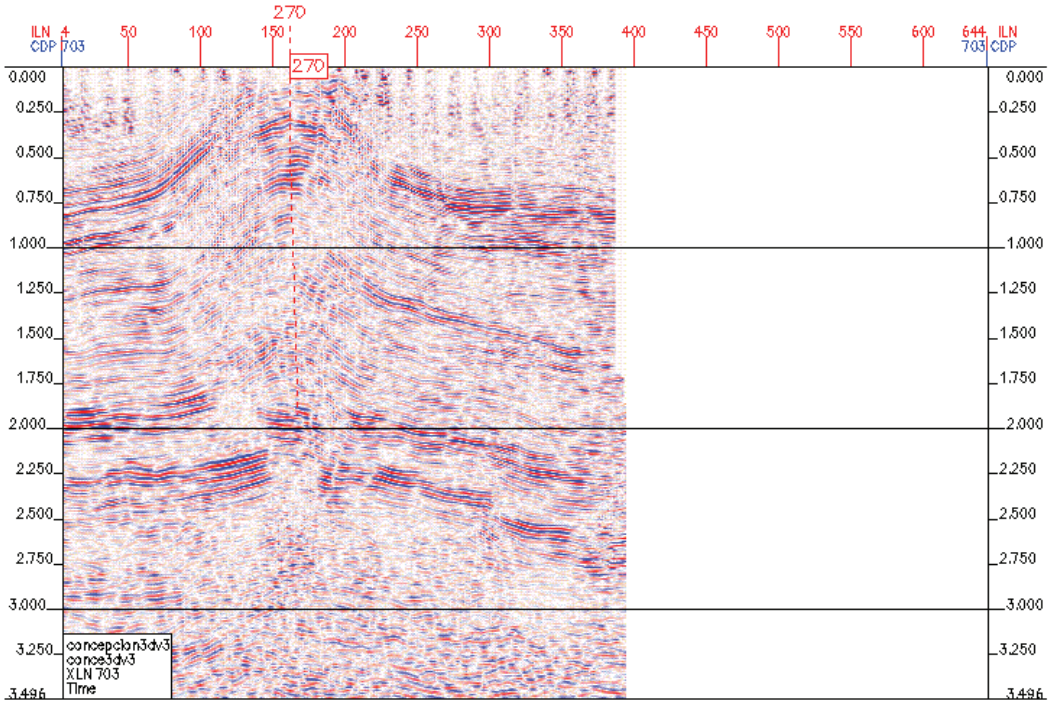

Figure 3.2 Pre-interpreted crossline 703 and the Borehole C-270 location.

These stratigraphic major markers (Tops) and checkshot two-way times recorded at the Borehole C-270, C-150, C-152, and C-153 are shown in Tables 3.7 and 3.8.

Table 3.7 Selected stratigraphic major markers (Tops) at the Borehole C-270.

Formation Top	Depth		Checkshot Time (m.sec)
	(Ft)	(Meter)	
ARENA SUP. A	1992. 97	607.47	571
GUASARE	7410.00	2258.00	1580
BASEMENT	11742 .00	3579.00	2226

Table 3.8 Stratigraphic major markers (Tops) and checkshot two-way times at the boreholes C-150, C-152, and C-153.

Formation Top Name	Borehole Name					
	C-150		C-152		C-153	
	Formation Top Depth (ft)	Checkshot (m.sec)	Formation Top Depth (ft)	Checkshot (m.sec)	Formation Top Depth (ft)	Checkshot (m.sec)
ARENA SUP A	3541.886	-------	1731.007	530	689.173	---------
GUASARE	10109.422	--------	8233.896	1520	7551.565	1504
BASEMENT	----------	---------	12426.810	---------	----------	---------

The tops of the Arena Basal Mioceno (Miocene ?), Arena Sup A, Guasare Formations, and the top of Basement were determined at the selected boreholes based on the checkshot top two-way times and tied with the selected inlines and crosslines across the area of study**.** Faults were defined on the bases of seismic discontinuities or seismic low coherence**.** The interpreted markers and faults are shown in Figures 3.3 and 3.4.

3.2 Seismic Attributes

The purpose of generating seismic attributes in this study is to emphasize the presence of faults and fractures that are associated with the seismic response of the rock formations of La Concepcion field. In this dissertation research, geometric (coherence) and instantaneous attributes are applied to the 3-D seismic data of La Concepcion field.

3.2.1 Geometric Attributes

The low coherence of the variance attribute cube is indicative of faults and fractures. Variance attribute cube study was applied to La Concepcion field by Cordozo (2001). Cordozo used 100 milliseconds for the operator window length with inline range of 3 and crossline range of 3 as well. Seismic amplitude time slice at 1750 msec. and variance time slice at 1750 msec for the Mito Juan Formation show a northeast-southwest trend of fractured zone (Figure 3.5).

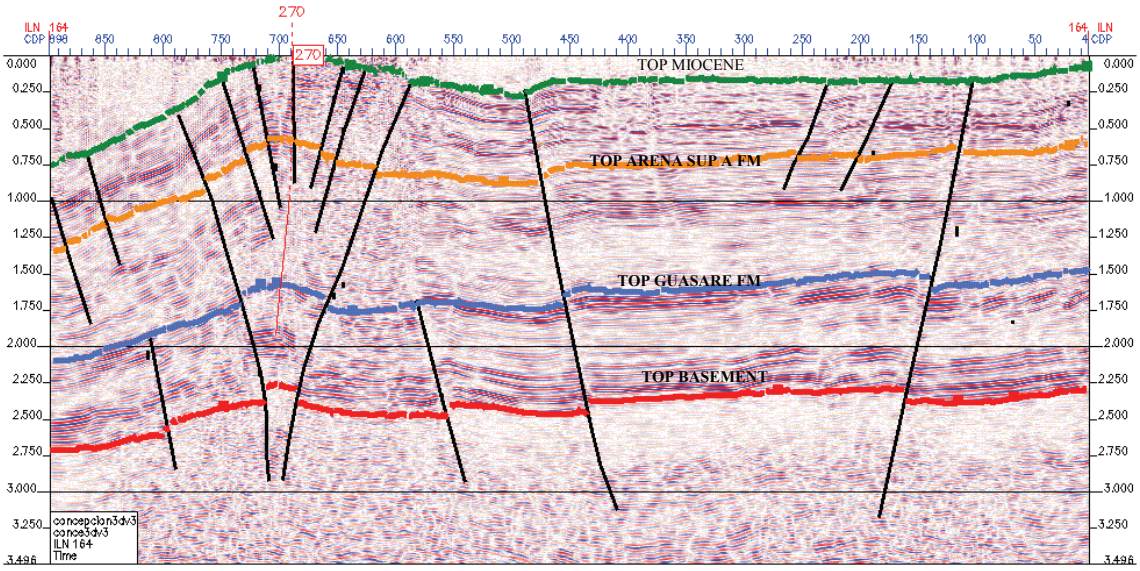

Figure 3.3 Interpreted inline 164.

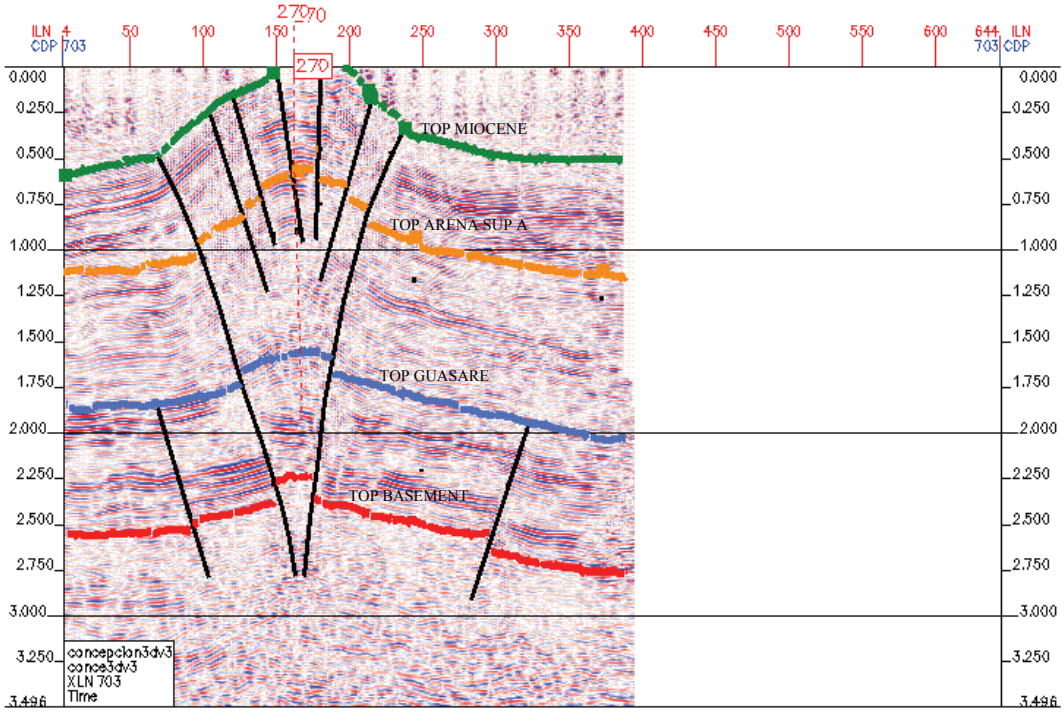

Figure 3.4 Interpreted crossline 703.

This dissertation research applied variance cube operator according to the setup shown below:

window length	:	60 ms
inline range	:	3
crossline range	:	3

Figures 3.6 through 3.9 are time cross section examples of the applied variance cube attributes for pre-interpreted and interpreted inline164 (Figures 3.1 and 3.3), and pre-interpreted and interpreted crossline 703 (Figures 3.2 and 3.4). It is obviously seen that the interpreted faults are exactly located in the zones of low coherence.

A seismic amplitude time slice at 952 msec within the ASA-MAI Formation is taken and displayed in Figure 3.10.a. Similarly, the variance time slice was taken at 952 ms as shown in Figure 3.10.b. The difference between the two pictures is clearly seen. The variance cube shown in Figure 3.10.b strongly emphasizes the low coherence zones along a northeast trend. These low coherence zones are indicative of highly fractured areas. The interpreted faults are clearly located in the fractured zones as shown in Figure 3.11

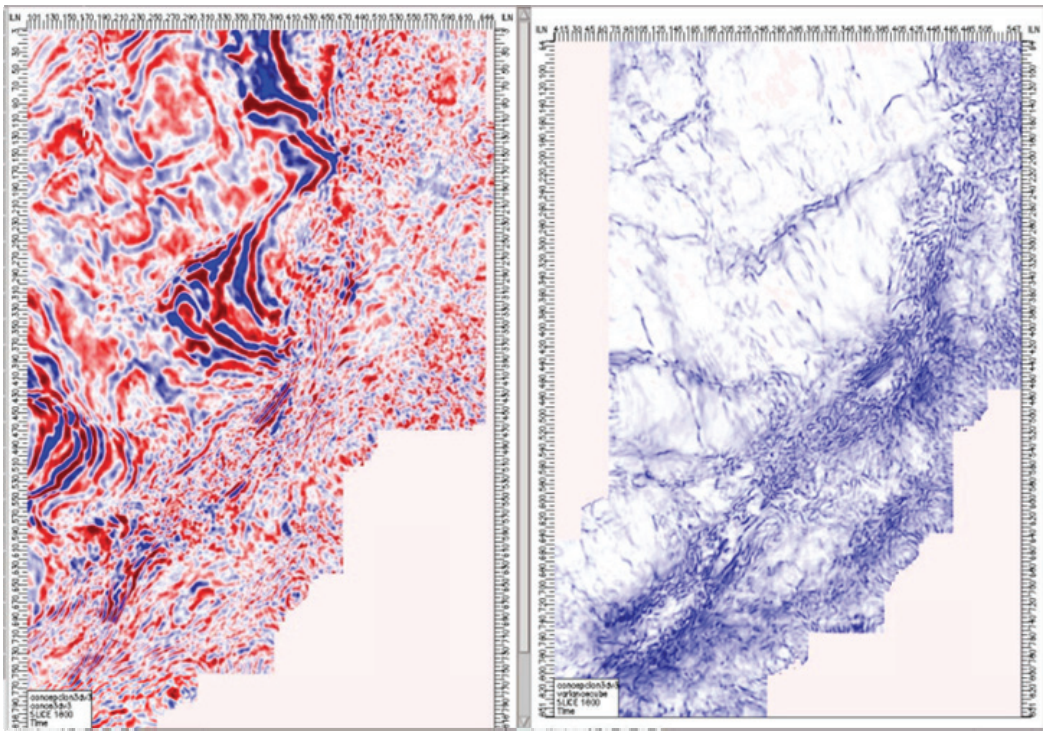

(a) (b)

Figure 3.5 Seismic amplitude time slice at 1750 msec (a) and Variance time slice at 1750 msec (b) for the Mito Juan Formation (from Cardozo, 2001)..

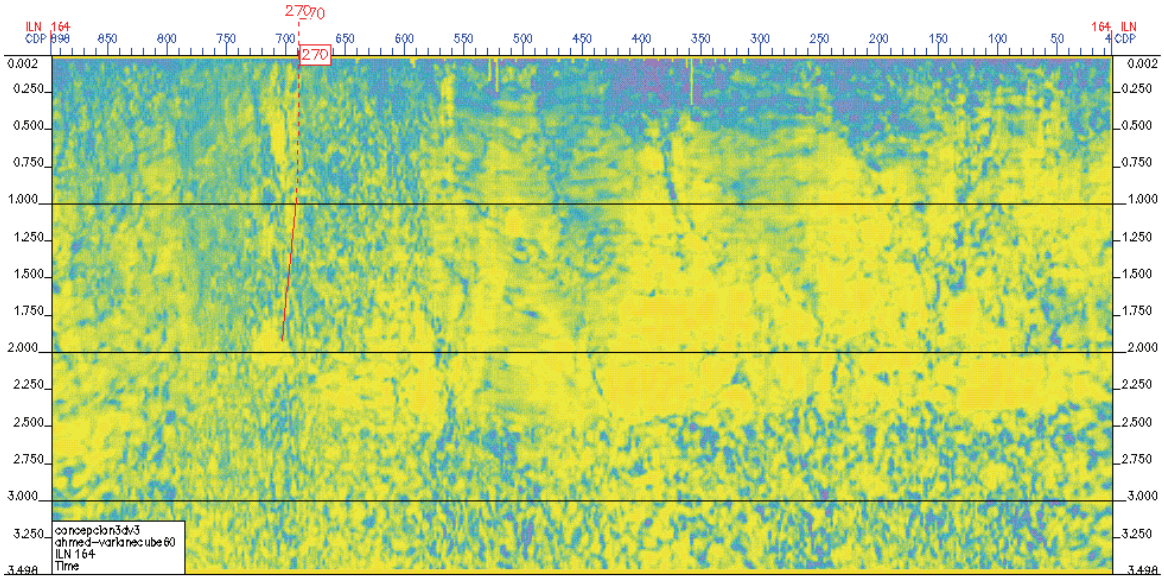

Figure 3.6 Inline 164 variance cube.

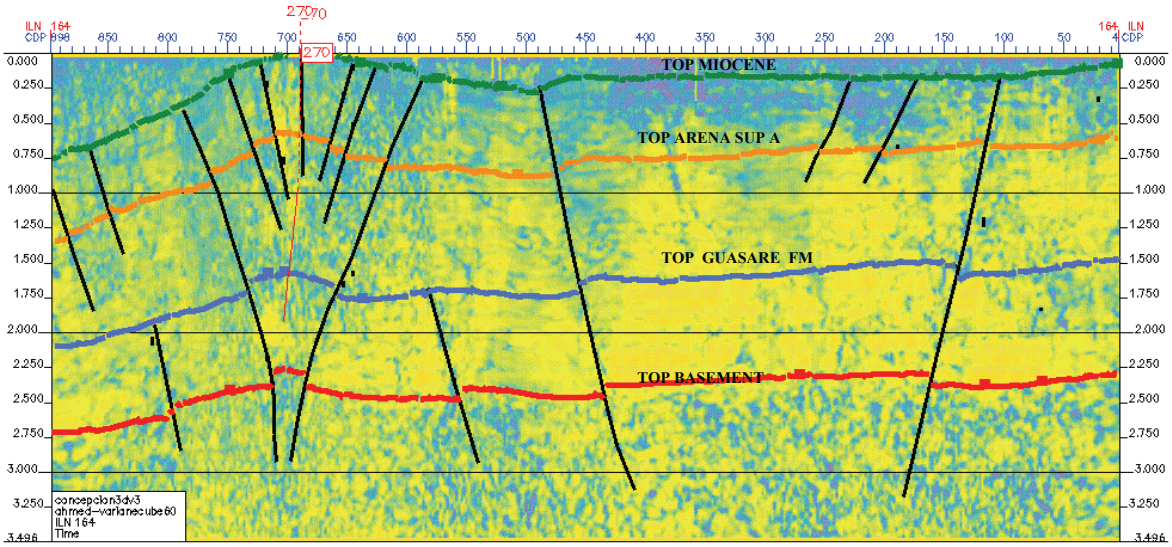

Figure 3.7 Interpreted section of inline 164 with variance cube.

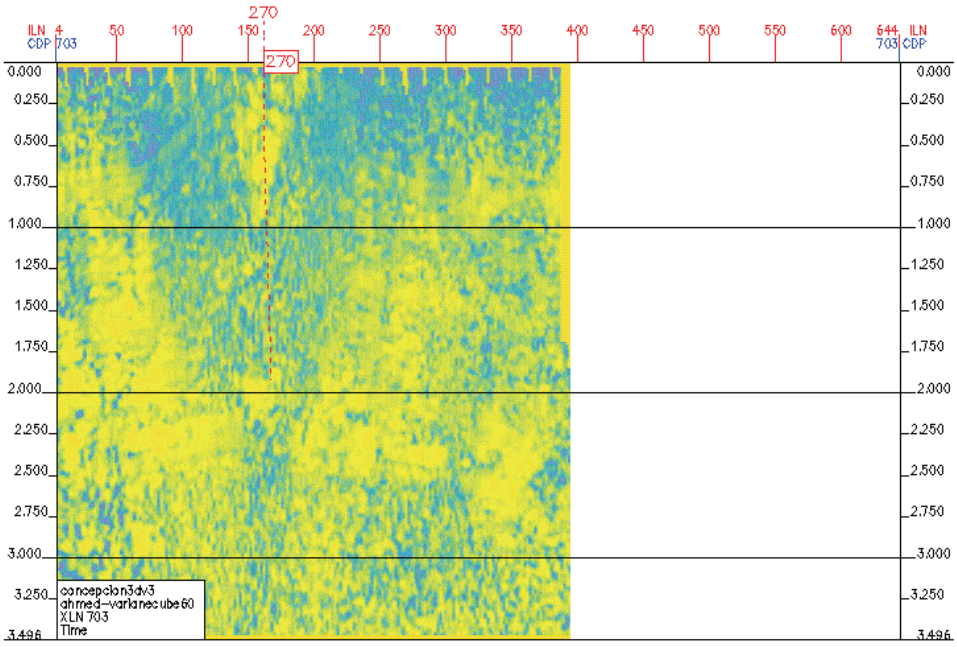

Figure 3.8 Pre-interpreted section of crossline 703 with variance cube.

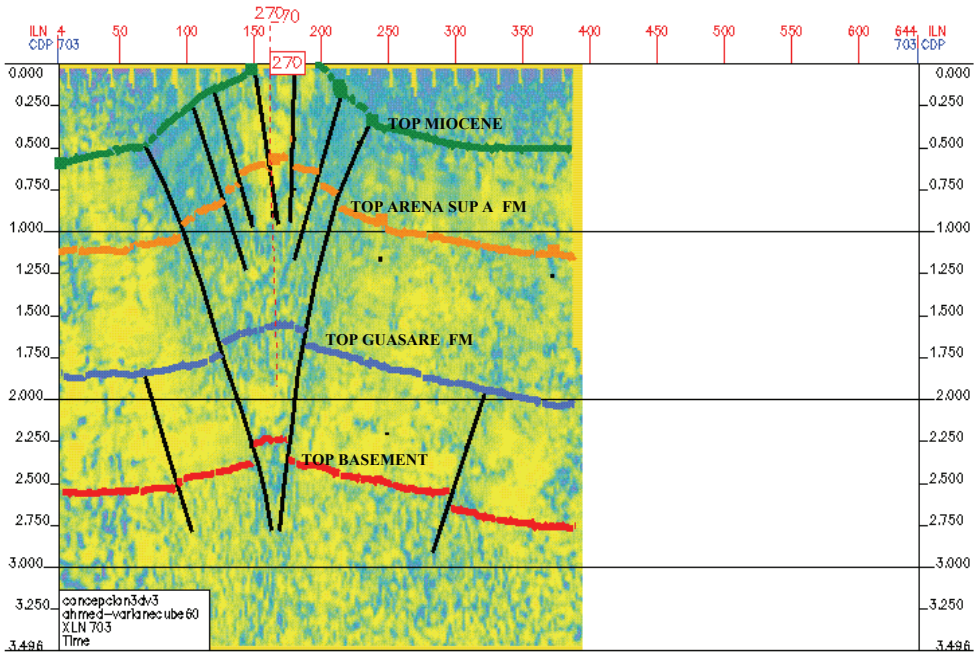

Figure 3.9 Interpreted section of crossline 703 with variance cube.

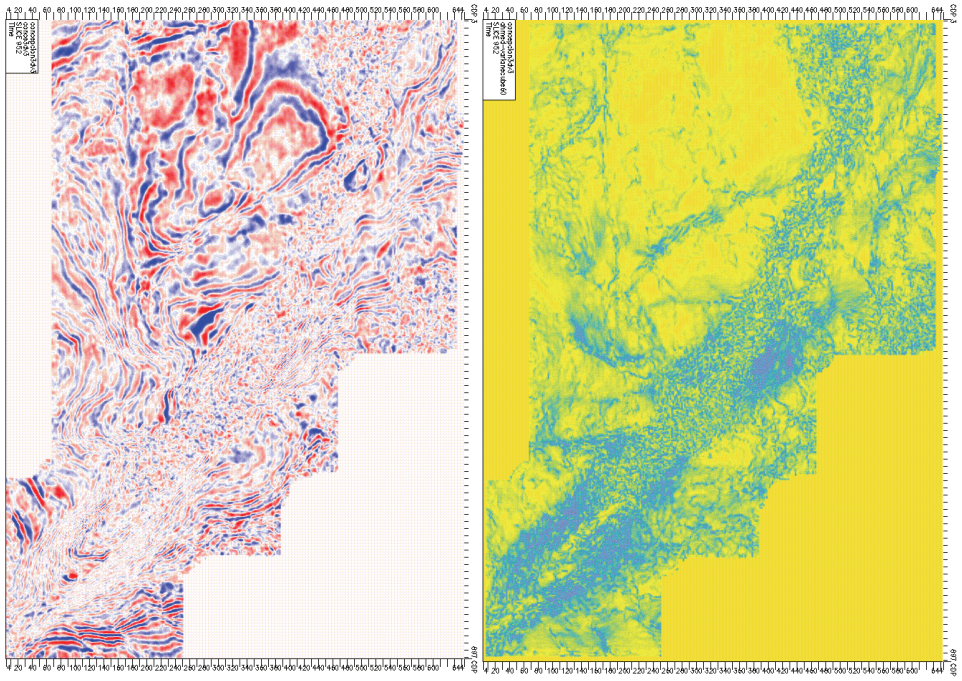

(a) **(b)**

Figure 3.10 Amplitude time slice at 952msec (a) and variance time slice at 952 msec (b) for the ASA-MAI Formation.

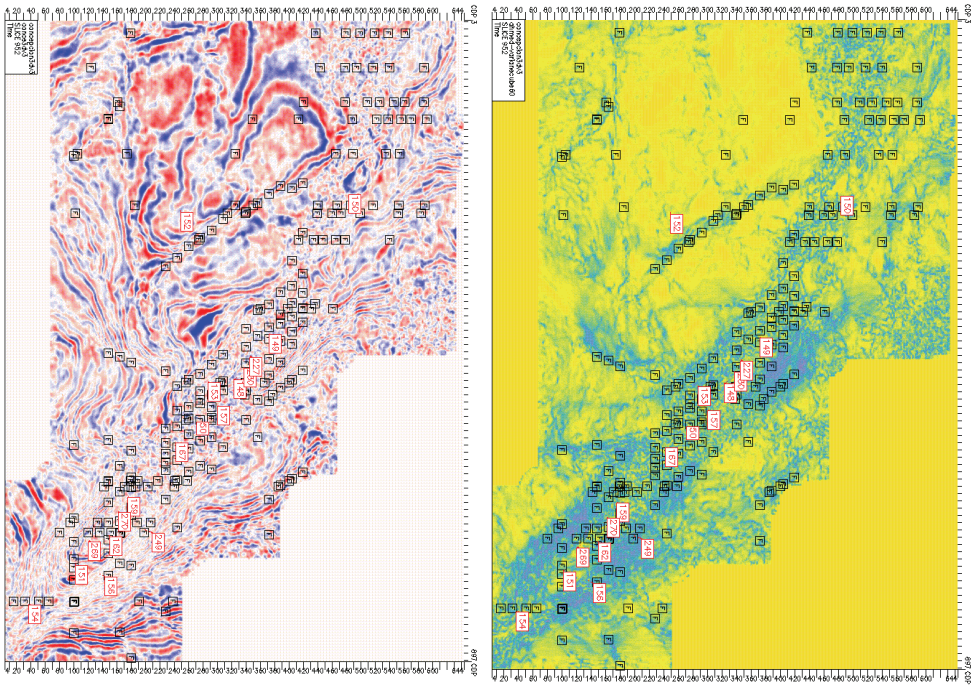

Figure 3.11 Amplitude (left) and variance cube (right) time slice at 952 msec for the ASA-MAI Formation showing fault and well locations.

3.2.2 Instantaneous Attributes

Instantaneous frequency attribute is any value that can be calculated at a point rather than an average over an entire interval. Frequency attribute of low value is of great importance as to be considered as a good hydrocarbon indicator.

This dissertation research applied instantaneous frequency to La Concepcion field in order to help locate faults and fractures at different subsurface horizons. Figures 3.12 through 3.15 show instantaneous frequencies at four horizon slices. Northeast-southeast major fault and fracture trends shown on each figure are indicated by low frequency values. However, the low

frequency anomaly trends at the two lower horizons are inconsistent with those trends indicated on the variance attributes (Figures 3.10 and 3.11).

3.3 Summary and Conclusions

An application of variance cube attribute to La Concepcion 3-D seismic data delineates the location of fault and fracture zones along a northeast-southwest general trend. Interval velocity estimation from the surface seismic survey, and interval velocity update using the image ray perturbation analysis are discussed in detail in chapter four.

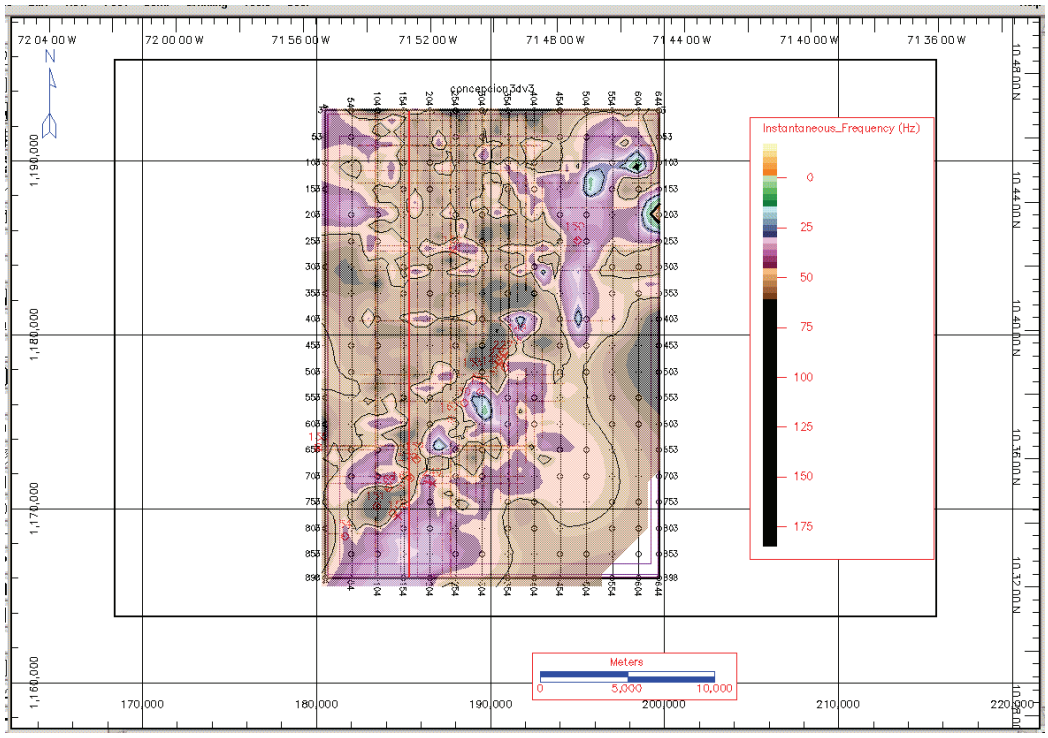

Figure 3.12 Instantaneous frequency at the Top of Miocene seismic horizon.

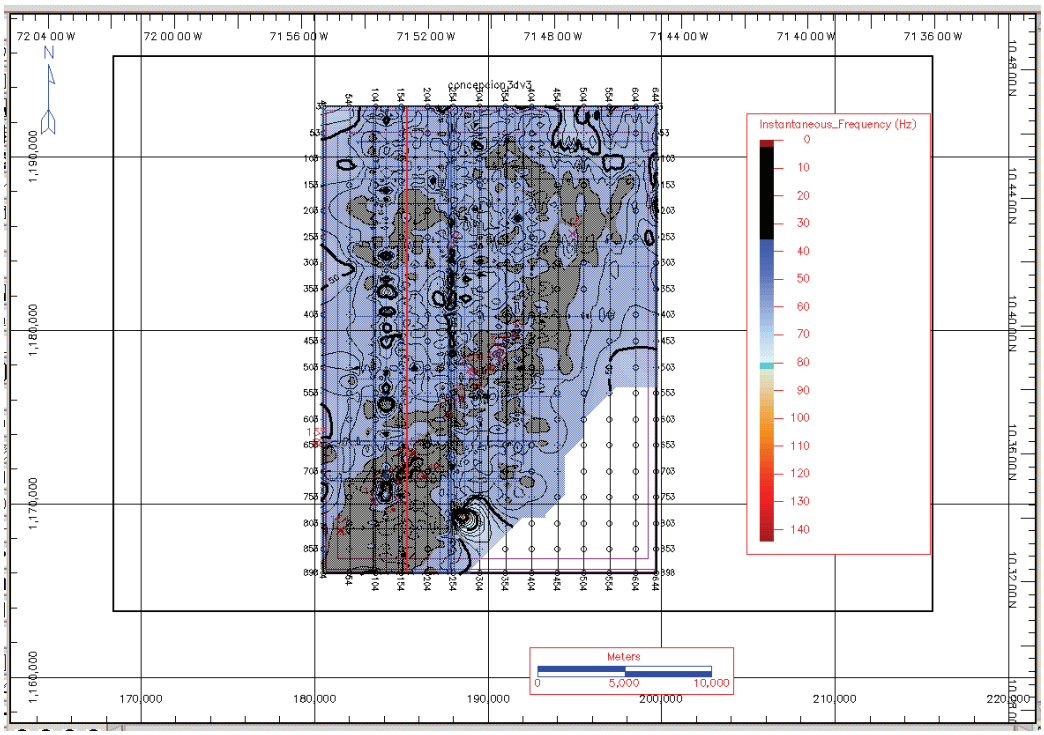

Figure 3.13 Instantaneous frequency at the Top of Arena Sup A seismic horizon.

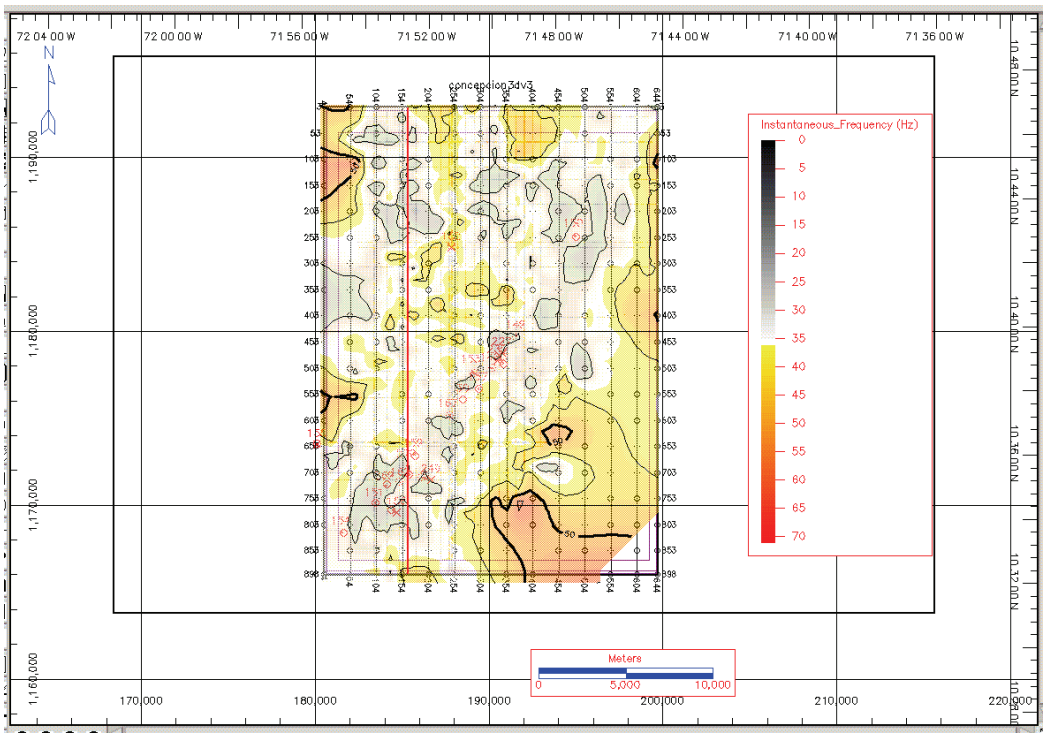

Figure 3.14 Instantaneous frequencies at the Top of the Guasare seismic horizon.

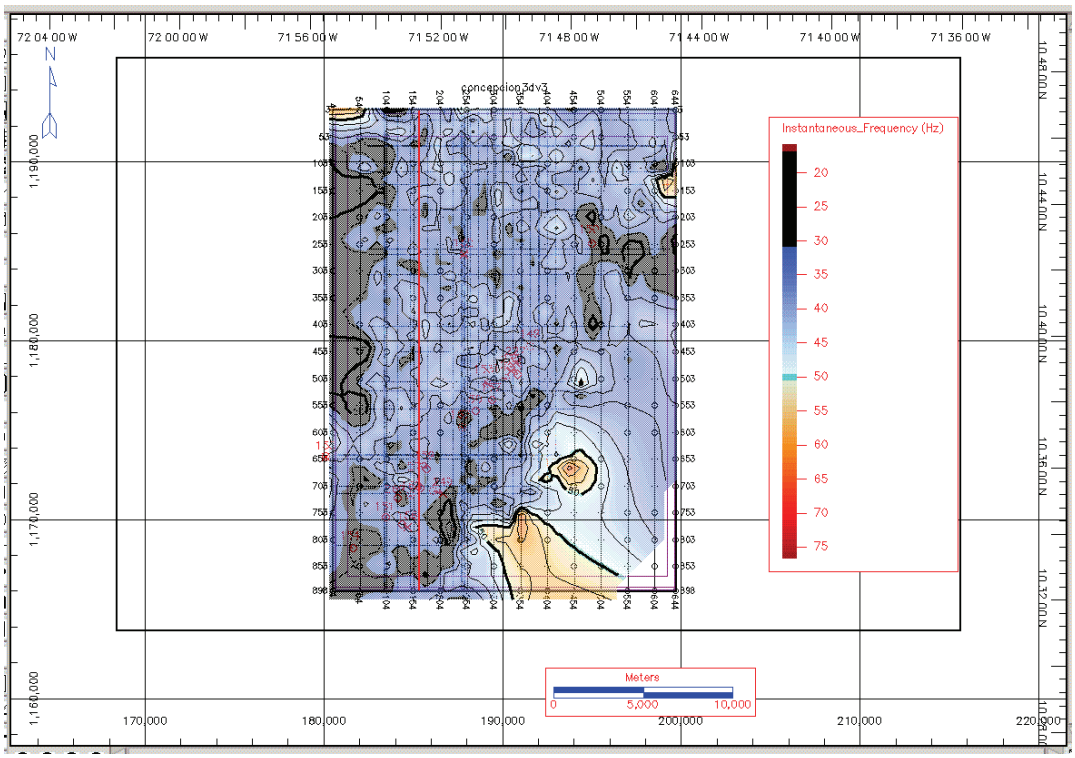

Figure 3.15 Instantaneous frequency at the Top of Basement seismic horizon.

CHAPTER 4

INTERVAL VELOCITY

This chapter presents the interval velocity estimation from seismic data. The estimated interval velocities are updated using image ray perturbation analysis through the depth conversion method. The following sections cover the interval velocity estimation method, observations, velocity update, velocity-depth check, and conclusions.

4.1 Interval Velocity Estimation from Seismic Data

The interval velocities at the CMP gathers of the surface seismic survey are estimated from V_{rms} and the two-way travel-times T at the top and bottom of each depth interval across the time sections of the rock formations using Dix's equation:

$$V_{\text{int}} = \sqrt{\frac{V^2_{rms(n)} T_{0,n} - V^2_{rms,n-1} T_{0,n-1}}{T_0 - T_{0,n-1}}} \tag{4.1}$$

and the rock formation thickness h is:

$$h = \tfrac{1}{2} V_n \Delta T \tag{4.2}$$

where ΔT is the two-way interval time.

The interval velocity, formation thickness, and depth calculated at CMP 693 gather of inline 164 through the Miocene Formations, the ASA-MAI and G-RN Formations are shown in Table 4.1. The interval velocities at CMP 693 are posted on the time section of inline 164 (Figure 4.1).

Table 4.1 Interval velocity at CMP gather 693 of inline 164**.** Highlighted data is indicative of interval velocity value for the ASA-MAI Formations.

Two-Way Times *T*(sec)	*t* (sec)	*Vrms* (m/sec)	$V_{Dix\ int}$ (m/sec)	$V_{Dix\ int}$ (ft/sec)	Thickness (meters)	Depth (meters)	Depth (ft)
0.000		1850	0.00	0.00	0.00	0.00	0.00
0.200	0.200	1964	1964.00	6441.92	196.40	196.40	644.19
0.384	0.184	2120	2277.48	7470.13	209.53	405.93	1331.44
0.562	0.178	2273	2572.26	8437.01	228.93	634.86	2082.34
0.650	0.088	2350	2792.11	9158.11	122.85	757.71	2485.29
0.766	0.116	2400	2662.86	8734.18	154.45	912.16	2991.88
0.892	0.126	2550	3319.10	10886.65	209.10	1121.26	3677.74
1.082	0.190	2656	**3105.65**	10186.53	295.04	1416.30	4645.46
1.180	0.098	2751	3638.58	11934.55	178.29	1594.59	5230.25
1.470	0.290	2950	3649.48	11970.31	529.18	2123.76	6965.94
1.648	0.178	3000	3384.80	11102.15	301.25	2425.01	7954.04
1.818	0.170	3121	4113.45	13492.13	349.64	2774.65	9100.87
1.954	0.136	3109	2943.89	9655.97	200.18	2974.84	9757.47
2.028	0.074	3161	4312.90	14146.32	159.58	3134.42	10280.89
2.114	0.086	3223	4440.88	14566.09	190.96	3325.37	10907.23
2.208	0.094	3280	4369.73	14332.72	205.38	3530.75	11580.87
5.000	2.792	5000	6021.85	19751.67	8406.50	11937.26	39154.20

4.2 Observations

The recorded depths at the Borehole C-270 do not match the computed depths using the checkshot recorded arrival times at the Borehole C-270 and interval velocities at CMP 693 gather nearby the Borehole C-270 within the fractured zone. Table 4.2 below illustrates the difference between recorded and computed depths at CMP 693 gather using the interval velocity calculated from observed velocity V_{rms}. This difference between recorded and computed depths probably originates due to the time migration error. Time migration uses rms velocity (V_{rm}) and assumes a straight raypath without taking into account any other assumption that can take care of the bending raypath. In contrast to time migration, depth migration or depth conversion methods use interval velocity and take into account the assumption of bending raypath (image ray) which bends in accordance with Snell's Law**.** Using image ray perturbation technique through depth conversion method can correct the computed depths by relocating the correct depths and update the interval velocities.

4.3 Velocity Update (Image Ray Perturbation Analysis)

This study used the image ray perturbation analysis as an interval velocity estimation through depth conversion method. Three steps are followed in order to obtain an accurate depth section from a time section using image ray for the depth conversion method.

Step 1: An interval velocity grid which covers the entire section of the seismic line is needed. Therefore, interval velocities at nine more selected CMP gathers of inline 164 were calculated and are presented in Tables 4.3 through 4.11.

The interval velocities for the four defined formations were calculated at the ten CMP gathers of inline 164 as shown in Table 4.12 and Figure 4.3**.**

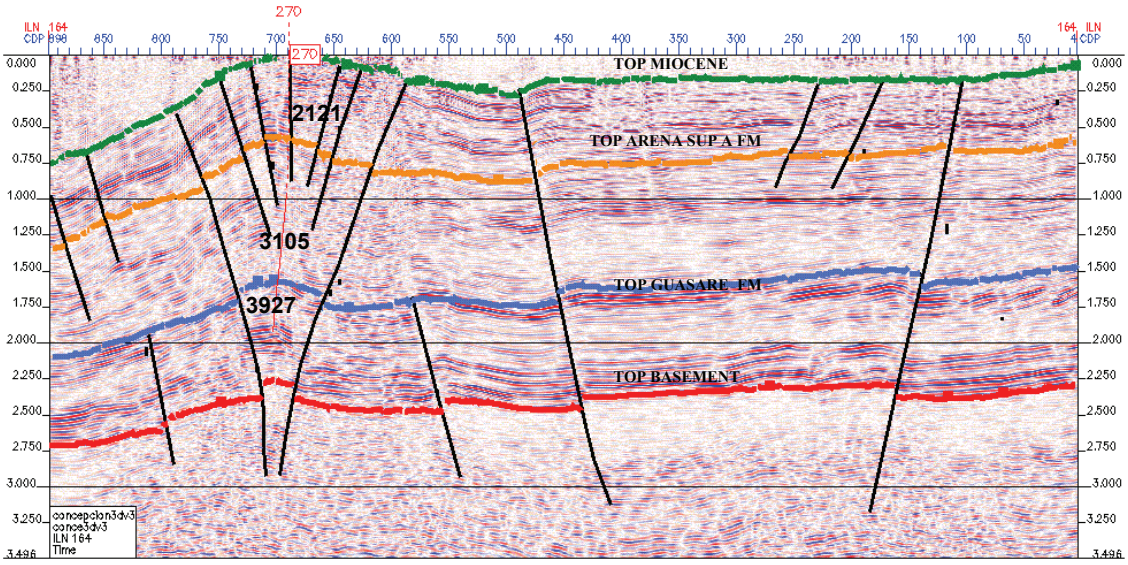

Figure 4.1 Inline 164 with interval velocities at the CMP gather 693.

Table 4.2 The difference between recorded and computed depth at CMP gather 693 of inline 164. Important data in bold.

Top Formation Name	Recorded Depth (meters)	Observed Thickness (meters)	Checkshot Travel-times (m.sec)	Estimated Interval Velocity (m/sec)	Computed Depth (meters)
Arena Sup-A Fm	**608**	608	571	**2121**	**605**
Guasare Fm	**2258**	1650	1580	**3105**	**2172**
Basement	**3579**	1321	2250	**3927**	**3487**

Table 4.3 Interval velocity at CMP gather 693 of inline 164.

Two-Way Time T (sec)	Δt (sec)	V_{rms} (m/sec)	$V_{Dix\ int}$ (m/sec)	Thickness h (meters)	Depth d (meters)
0.00	0.00	1850	0.00	0.00	0.00
0.22	0.22	1999	1999.00	220.89	152.10
0.41	0.19	2135	2286.10	212.61	364.71
0.58	0.17	2267	2558.71	214.93	579.64
0.84	0.26	2436	2768.61	365.46	945.10
1.03	0.19	2600	3217.19	310.46	1255.55
1.23	0.20	2718	3262.18	324.59	1580.14
1.54	0.30	2932	3673.24	558.33	2138.47
1.78	0.24	3120	4110.00	501.42	2639.89
1.96	0.18	3228	4128.99	379.87	3019.76
2.18	0.22	3408	4719.37	519.13	3538.89
2.35	0.16	3605	5602.32	459.39	3998.28
5.00	2.65	5000	5968.20	7916.82	11915.10

Table 4.4 Interval velocity at CMP 141 gather of inline 164.

Two-Way Time *T*(sec)	*t* (sec)	*Vrms* (m/sec)	*Vint* (m/sec)	Thickness h(meters)	Depth d(meters)
0.00	0.00	1850	0.00	0.00	0.00
0.25	0.25	2017	2017.00	254.14	254.14
0.41	0.16	2132	2299.49	186.26	440.40
0.56	0.14	2240	2528.68	179.54	619.94
0.77	0.22	2418	2821.59	307.55	927.49
0.91	0.14	2533	3092.55	216.48	1143.97
1.07	0.15	2600	2971.19	225.81	1369.78
1.22	0.15	2760	3692.17	280.60	1650.38
1.42	0.20	2890	3587.53	355.17	2005.55
1.78	0.36	3192	4172.94	751.13	2756.68
1.93	0.15	3351	4819.42	371.10	3127.78
2.19	0.26	3461	4193.32	540.94	3668.71
2.29	0.11	3620	6028.62	319.52	3988.23
2.40	0.10	3705	5240.30	272.50	4260.73
5.00	2.60	5000	5948.88	7739.49	12000.22

Table 4.5 Interval velocity at CMP 213 gather of inline 164.

Two-Way Time *T*(sec)	*t* (sec)	*Vrms* (m/sec)	*Vint* (m/sec)	Thickness (meters)	Depth (meters)
0.000	0.000	1850	0.00	0.00	0.00
0.222	0.222	1969	1969.00	218.56	218.56
0.384	0.162	2093	2251.86	182.40	400.96
0.578	0.194	2270	2584.86	250.73	651.69
0.724	0.146	2386	2798.43	204.29	855.98
0.856	0.132	2502	3061.04	202.03	1058.00
1.090	0.234	2650	3132.38	366.49	1424.49
1.230	0.140	2798	3755.86	262.91	1687.40
1.464	0.234	2981	3800.70	444.68	2132.08
1.692	0.228	3160	4128.42	470.64	2602.72
1.860	0.168	3300	4471.98	375.65	2978.37
2.128	0.268	3450	4350.81	583.01	3561.38
2.320	0.192	3600	4967.96	476.92	4038.30
5.000	2.680	5000	5951.70	7975.27	12013.58

Table 4.6 Interval velocity at CMP 405 gather of inline 164.

Two-Way Time *T*(sec)	Δ*t* (sec)	*Vrms* (m/sec)	*Vint* (m/sec)	Thickness h(meters)	Depth d(meters)
0.000	0.000	1850	0.00	0.00	0.00
0.286	0.286	2070	2070.00	296.01	296.01
0.380	0.094	2150	2376.90	111.71	407.72
0.590	0.210	2337	2641.95	277.40	685.13
0.820	0.230	2519	2934.70	337.49	1022.62
1.112	0.292	2650	2987.32	436.15	1458.77
1.266	0.154	2700	3036.70	233.83	1692.59
1.556	0.290	3050	4253.01	616.69	2309.28
1.722	0.166	3106	3588.68	297.86	2607.14
1.836	0.114	3142	3642.77	207.64	2814.78
1.998	0.162	3256	4343.70	351.84	3166.62
2.224	0.226	3401	4483.35	506.62	3673.24
2.392	0.168	3600	5603.86	470.72	4143.96
5.000	2.608	5000	6003.57	7828.65	11972.61

Table 4.7 Interval velocity at CMP 453 gather of inline 164.

Two-Way Time *T*(sec)	Δt (sec)	*Vrms* (m/sec)	*Vint* (m/sec)	Thickness h(meters)	Depth d(meters)
0.000	0.000	1850	0.00	0.00	0.00
0.323	0.323	2083	2083.00	336.40	13.03
0.437	0.114	2194	2481.68	141.46	477.86
0.578	0.141	2316	2658.79	187.44	328.90
0.677	0.099	2402	2852.81	141.21	328.66
0.805	0.128	2493	2927.63	187.37	328.58
0.991	0.186	2550	2783.27	258.84	446.21
1.153	0.162	2600	2887.07	233.85	492.70
1.286	0.133	2850	4464.78	296.91	530.76
1.405	0.119	2890	3291.40	195.84	492.75
1.635	0.230	3028	3762.67	432.71	628.55
1.799	0.164	3114	3868.21	317.19	749.90
1.947	0.148	3208	4185.07	309.70	626.89
2.275	0.328	3386	4293.28	704.10	1013.79
2.449	0.174	3462	4334.76	377.12	1081.22
5.000	2.551	5000	6123.25	7810.20	8187.33

Table 4.8 Interval velocity at CMP 549 gather of inline 164.

Two-Way Time *T*(sec)	Δ*t* (sec)	*Vrms* (m/sec)	*Vint* (m/sec)	Thickness h(meters)	Depth d(meters)
0.000	0.000	1850	0.00	0.00	0.00
0.202	0.202	1862	1862.00	188.06	13.03
0.220	0.018	1982	3017.43	27.16	215.22
0.346	0.126	2092	2271.33	143.09	170.25
0.478	0.132	2188	2421.64	159.83	302.92
0.630	0.152	2303	2632.10	200.04	359.87
0.690	0.060	2345	2747.51	82.43	282.46
0.806	0.116	2427	2866.69	166.27	248.69
0.980	0.174	2536	2989.51	260.09	426.36
1.114	0.134	2628	3221.94	215.87	475.96
1.270	0.156	2800	3808.80	297.09	512.96
1.462	0.192	2906	3527.83	338.67	635.76
1.634	0.172	3032	3943.68	339.16	677.83
1.762	0.128	3102	3886.35	248.73	587.88
1.978	0.216	3200	3908.71	422.14	670.87
2.188	0.210	3293	4065.90	426.92	849.06
2.272	0.084	3343	4451.77	186.97	613.89
2.378	0.106	3408	4584.76	242.99	669.91
5.000	2.622	5000	6094.25	7989.56	8176.54

Table 4.9 Interval velocity at CMP 645 gather of inline 164.

Two-way Time *T*(sec)	Δ*t* (sec)	*Vrms* (m/sec)	*Vint* (m/sec)	Thickness h(meters)	Depth d(meters)
0.000	0.000	1850	0.00	0.00	0.00
0.289	0.289	1863	1863.00	269.20	269.20
0.531	0.121	2239	2618.21	158.40	427.61
1.014	0.242	2650	3038.35	366.88	794.49
1.239	0.113	2785	3326.09	187.09	981.58
1.571	0.166	3036	3830.13	317.90	1299.48
1.782	0.106	3091	3473.23	183.21	1482.69
1.965	0.092	3139	3572.85	163.46	1646.15
2.178	0.107	3215	3845.93	204.80	1850.95
2.254	0.038	3242	3937.86	74.82	1925.77
2.333	0.040	3271	4011.04	79.22	2004.98
2.452	0.059	3348	4604.46	136.98	2141.97
5.000	1.274	5000	6186.38	3940.72	6082.69

Table 4.10 Interval velocity at CMP 741 gather of inline 164.

Two-way Time *T*(sec)	Δt (sec)	*Vrms* (m/sec)	*Vint* (m/sec)	Thickness h(meters)	Depth d(meters)
0.000	0.000	1800	0.00	0.00	0.00
0.258	0.258	2100	2100.00	270.90	270.90
0.462	0.204	2170	2255.42	230.05	500.95
0.628	0.166	2305	2644.69	219.51	720.46
0.810	0.182	2400	2702.28	245.91	966.37
0.918	0.108	2516	3256.87	175.87	1142.24
1.150	0.232	2700	3329.81	386.26	1528.50
1.280	0.130	2850	3935.34	255.80	1784.30
1.396	0.116	2900	3403.29	197.39	1981.69
1.698	0.302	3019	3517.14	531.09	2512.77
1.780	0.082	3080	4146.12	169.99	2682.77
2.050	0.270	3180	3773.51	509.42	3192.19
5.000	3.604	5000	5605.90	10101.83	12083.51

Table 4.11 Interval velocity at CMP 813 gather of inline 164.

Two-Way Time *T*(sec)	Δ*t* (sec)	*Vrms* (m/sec)	*Vint* (m/sec)	Thickness (meters)	Depth (meters)
0.000		1800	0.00	0.00	0.00
0.199	0.199	1928	1928.00	191.84	191.84
0.355	0.156	2043	2180.91	170.11	361.95
0.481	0.126	2135	2375.12	149.63	511.58
0.633	0.152	2243	2554.86	194.17	705.75
0.746	0.113	2300	2596.26	146.69	852.44
0.915	0.169	2429	2931.36	247.70	1100.14
1.101	0.186	2550	3076.72	286.14	1386.27
1.219	0.118	2625	3242.23	191.29	1577.56
1.344	0.125	2700	3344.35	209.02	1786.59
1.478	0.134	2750	3208.68	214.98	2001.57
1.955	0.477	3115	4041.82	963.97	2965.54
2.165	0.210	3192	3835.35	402.71	3368.25
2.411	0.246	3250	3721.67	457.76	3826.02
5.000	2.589	5000	6200.39	8026.41	11852.43

Table 4.12 Average interval velocities of the selected CMP gathers of inline 164. Important data in bold.

CMP Number	813	741	693	645	549	453	405	213	141	93
Distance (meters)	2582	4577	6337	7276	10210	13026	14317	19950	22062	23471
Recent Fm Velocity (m/s)	1970	1800	Missing	1850	1850	1850	1850	1850	1850	1850
Miocene Fm Velocity (m/s)	2614	2177	**2121**	2240	2546	2519	2363	2268	2282	2281
Arena Sup A-Mb. Areniscas Inferiores Fm Velocity (m/s)	3218	3255	**3105**	3182	3387	3271	3303	3309	3233	3230
Guasare – Rio Negro Fm Velocity (m/s)	3866	3960	**3927**	3978	4140	4089	4015	4317	4804	4640
Basement Velocity (m/s)	6200	5606	**6022**	6186	6094	6123	5804	5460	5594	5968

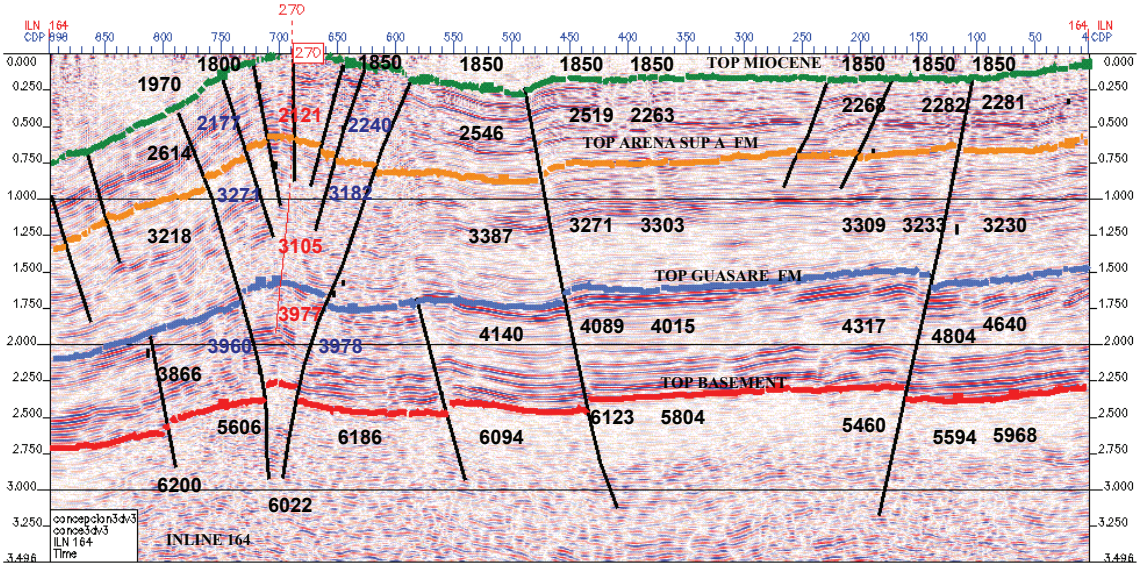

Figure 4.2 Estimated interval velocity grid of the selected CMP gathers.

Step 2: The interpreted time section of inline 164 (Figure 4.2) is digitized as shown in Figure 4.3.

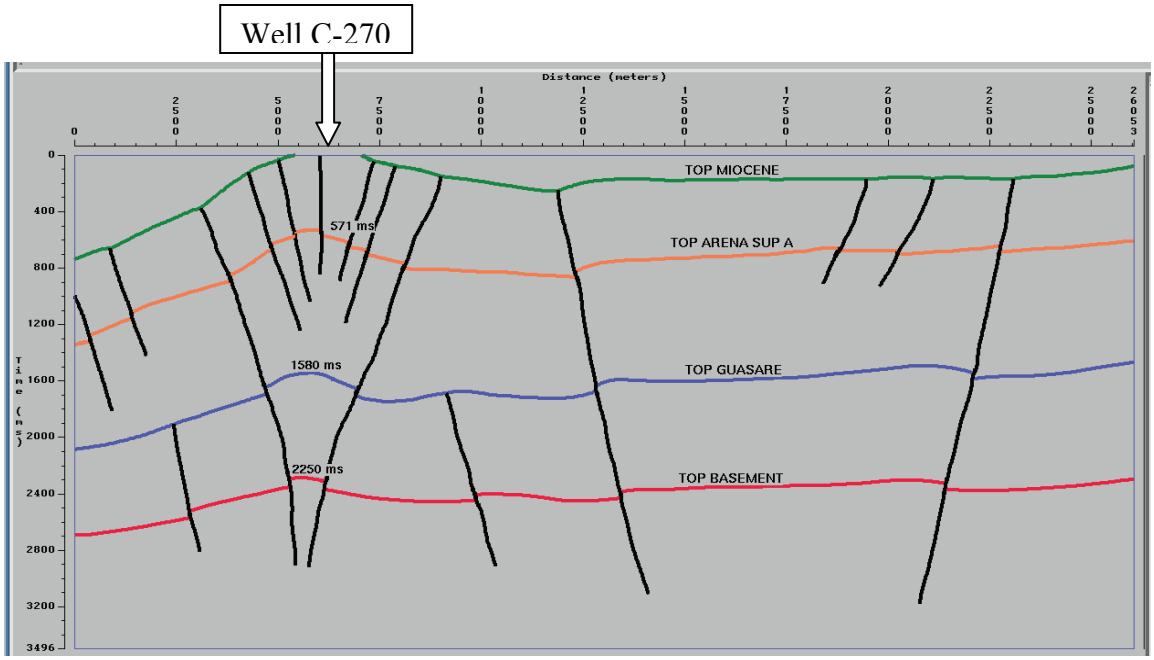

Figure 4.3 Digitized time section of seismic inline 164.

Step 3: The depth conversion technique is applied on the digitized time section of Figure 4.3 using the interval velocity grid of Table 4.12**.** The best way to update interval velocity at and around the Borehole C-270 or CMP 693 of inline 164 is to apply image ray perturbation as a velocity analysis. This technique was developed using an interactive process of depth conversion method, updating interval velocities of the formations at and around CMP 693 for every run of depth conversion until the computed depths match the recorded depths. The interval velocities applied for the last depth conversion run and at which the computed depths match the depths at the well occur are considered as the updated interval velocities. Figures 4.4 through 4.6 show the image ray depth model, ray tracing, and synthetic traces using the estimated velocities, whereas the image ray depth model, ray tracing, and synthetic traces using the updated velocities are shown in Figures 4.7 through 4.9. Table 4.13 shows the updated interval velocities obtained from the layer migration modeling.

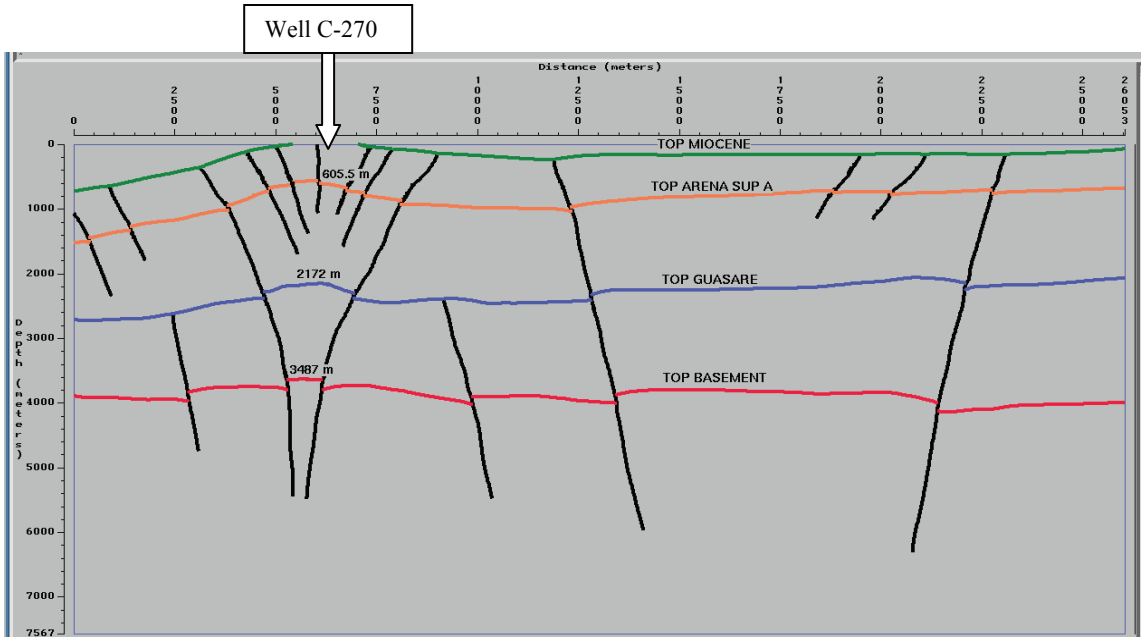

Figure 4.4 Image ray depth section for seismic inline 164 using estimated interval velocities. Note: the converted depths do not match the recorded depths at the Borehole C-270.

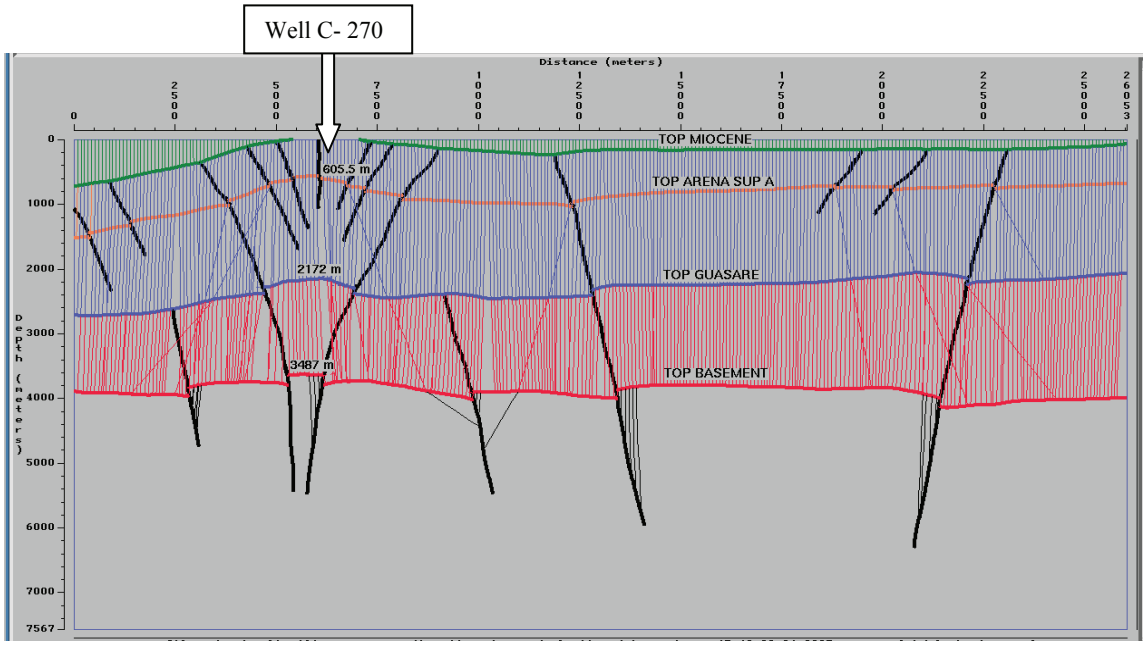

Figure 4.5 Image ray tracing for inline 164 using estimated interval velocities.

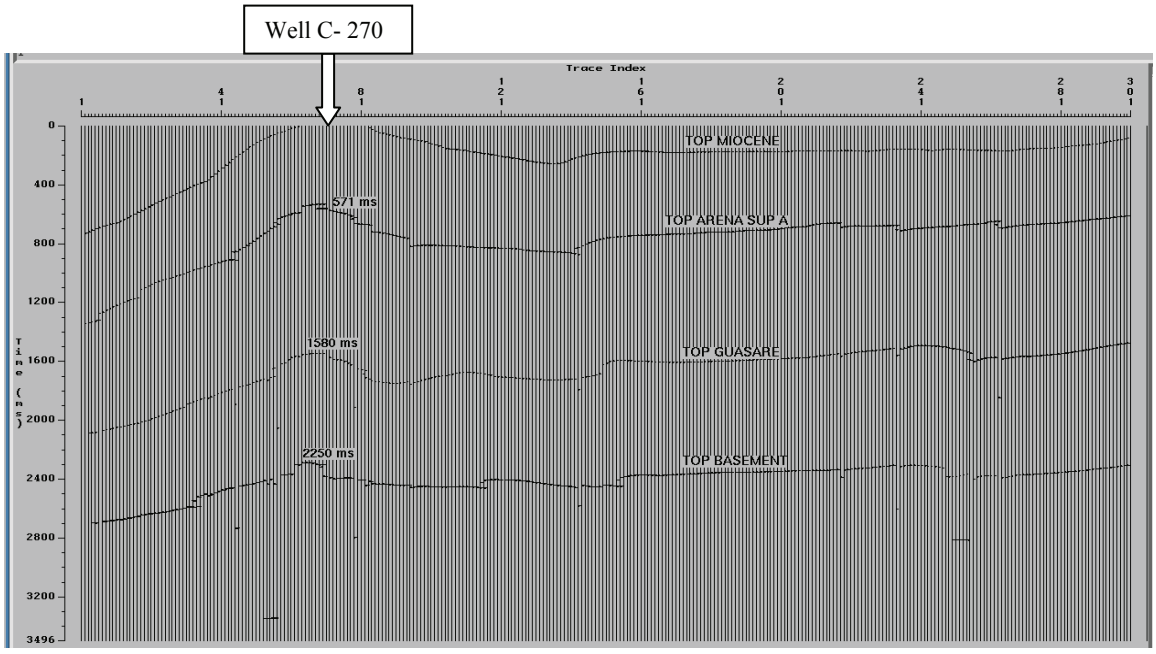

Figure 4.6 Synthetic traces for inline 164 using estimated velocities.

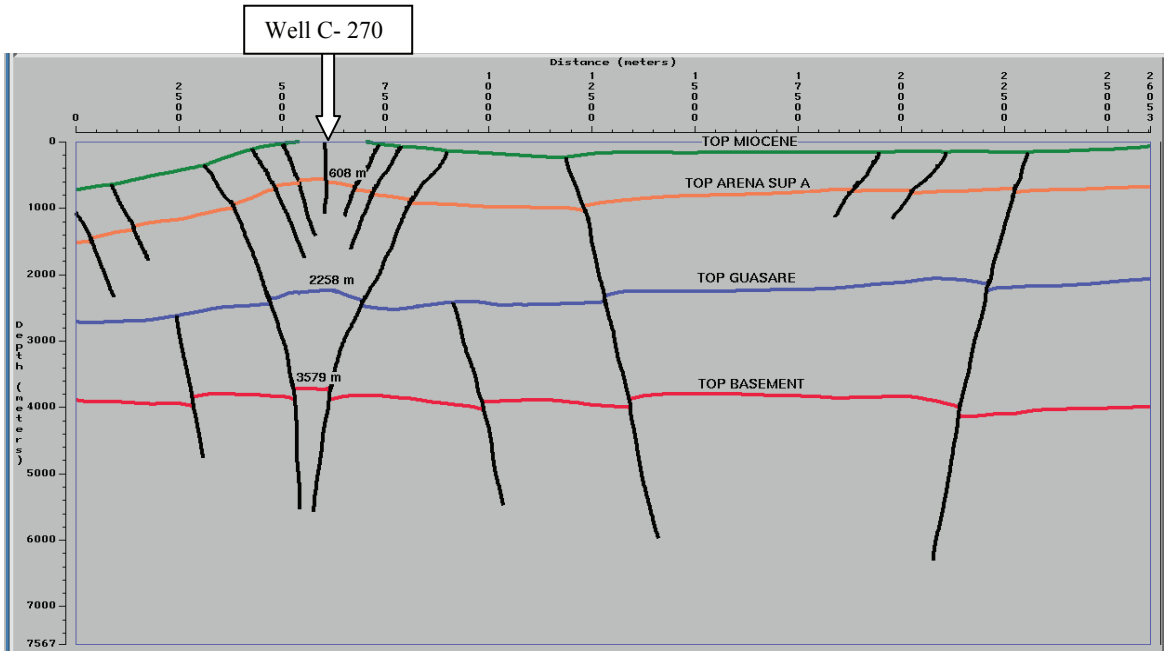

Figure 4.7 Image ray depth section for inline 164 using updated interval velocities. Note: a good match between recorded and converted depths.

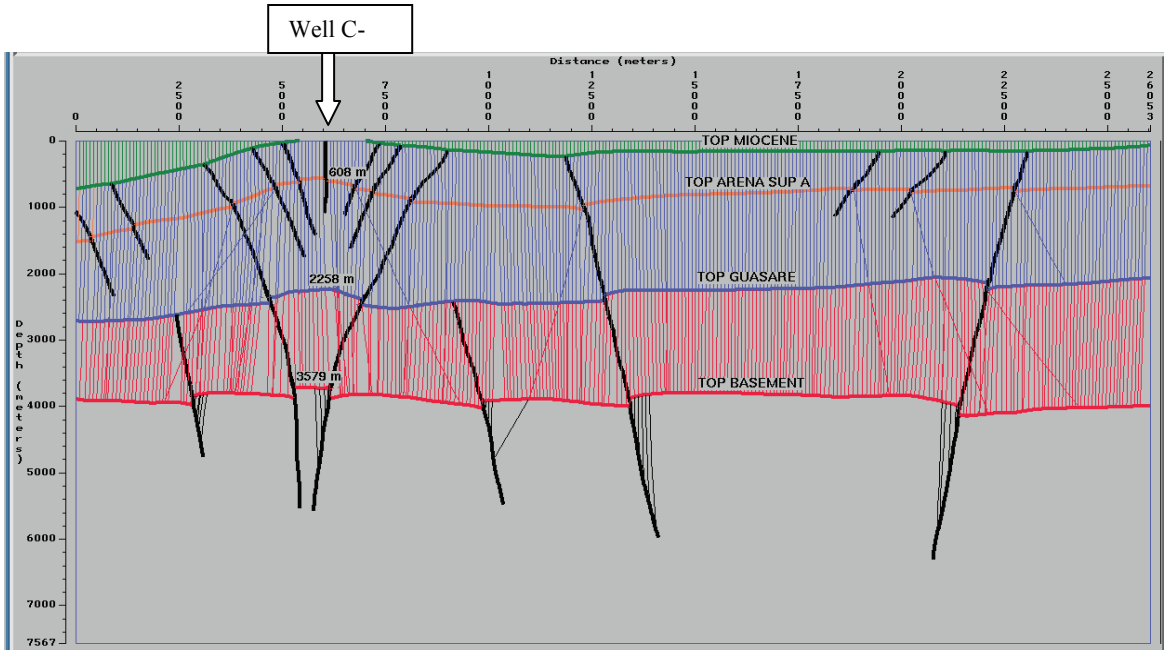

Figure 4.8 Ray traces for inline 164 using updated interval velocities.

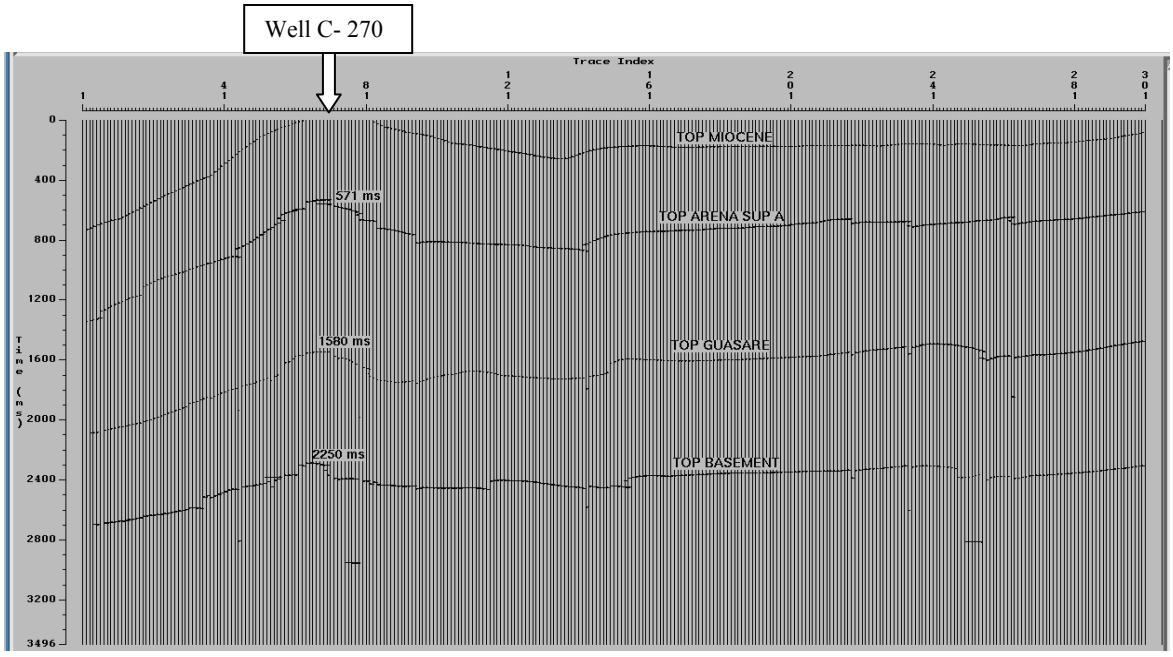

Figure 4.9 Synthetic traces for inline 164 using updated interval velocities.

Table 4.13 Updated interval velocities for inline 164. Updated values highlighted.

CMP Number	813	741	693	645	549	453	405	213	141	93
Distance (meters)	2582	4577	6337	7276	10210	13026	14317	19950	22062	23471
Recent Fm Velocity (m/s)	1970	1800	Missing	1850	1850	1850	1850	1850	1850	1850
Miocene Fm Velocity (m/s)	2614	2177 ***2184***	2121 ***2128***	2240 ***2247***	2546	2519	2363	2268	2282	2281
Arena Sup A –Mb. Areniscas Inferiores Fm Velocity (m/s)	3218	3255 ***3428***	3105 ***3272***	3182 ***3351***	3387	3271	3303	3309	3233	3230
Guasare – Rio Negro Fm Velocity (m/s)	3866	3960	3927 ***3943***	3978	4140	4089	4015	4317	4804	4640
Basement Velocity (m/s)	6200	5606	6022	6186	6094	6123	5804	5460	5594	5968

4.4 Velocity-Depth Check

Using the two-way times at CMP 693 nearby the Borehole C-270 and the updated interval velocities, the computed depths are exactly the same as the recorded depths as shown in Table 4.14.

Table 4.14 Data showing good match between recorded depths at the Borehole C-270 and computed depths. Estimated and updated velocity values in bold.

FROMATION TOP NAME	Recorded Depth (meters)	Observed Thickness (meters)	Estimated Interval Velocity (m/sec)	Two-way Travel-times to Top (m.sec)	Updated Or Input Interval Velocity (m/sec)	Computed Depth (meters
ARENA SUP-A UNIT	608	608	**2121**	571	**2128.00**	608
GUSARE FM	2258	1650	**3105**	1580	**3272.00**	2258
BASEMENT	3579	1321	**3927**	2250	**3943.28**	3579

4.5 Summary and Conclusions

The interval velocities were estimated from the 3-D seismic data of La Concepcion field. The image ray perturbation method was applied as an interval velocity update technique. It is concluded that the image-ray perturbation analysis serves as an interval velocity estimation method indicates the seismic

waves traveling through the ASA-MAI Formations near the fracture zone are affected the most. The following chapter covers the prediction of fracture effects on the seismic response of the ASA-MAI Formations and G-RN Formations.

CHAPTER 5

PREDICTION OF FRACTURE EFFECTS

This chapter covers the investigation study of the factors that are affecting or associated with the velocity anomaly and attenuation of the surface seismic survey through the ASA-MAI Formations, and G-RN Formations of La Concepcion field. The following sections present detailed information on borehole data review, velocity analysis, peak frequency, and conclusions.

5.1 Borehole Data Review

The Borehole C-270 includes a dataset of gamma-ray, density, and sonic logs (las format files). In order to precisely determine the evidence of the log variations through the rock formations in the borehole, depth cross-plots of gamma-ray, sonic, and density logs through ASA-MAI Formations, and G-RN Formations) are presented in Figures 5.1 through 5.6. The shale baseline on gamma-ray log through the ASA-MAI Formations (Figure 5.1) is about 80 API. From 2600 ft to 3000 ft gamma-ray log depicts a low value of about 50 API suggesting a thin permeable zone. The gamma-ray log across G-RN Formations (Figure 5.2) shows too spiky zones: from 7500 to 8400 ft and from 10300 ft to 11600 ft. Two permeable zones are shown on the log: from 8400 ft to 8600 ft with about 70 API, and from 8900 ft to 10300 ft with about 55 API. The sonic

log through ASA-MAI Formations (Figure 5.3) exhibits a general trend with a slightly high time rate at an average of 115 μ sec/ft recorded from 2000 ft to 2800 ft and an average of 90 - 100 μ sec/ft recorded from 3800 ft to 4700 ft. The sonic log through the G-RN Formations (Figure 5.4) shows a high sonic time rate zone of an average value of 90 μ sec/ft recorded from about 8400 ft to 10300 ft. The bulk density log through the G-RN Formations (from 2900 ft to 3000 ft, Figure 5.5) shows a zone of low density value: about 2 gm/cc. However, the density increases to about 2.45 gm/cc from 3000 ft to 7400 ft. Figure 5.6 represents the bulk density log through G-RN Formations. An average density value of about 2.55 gm/cc can be estimated across the depth from 8900ft to 10300 ft.

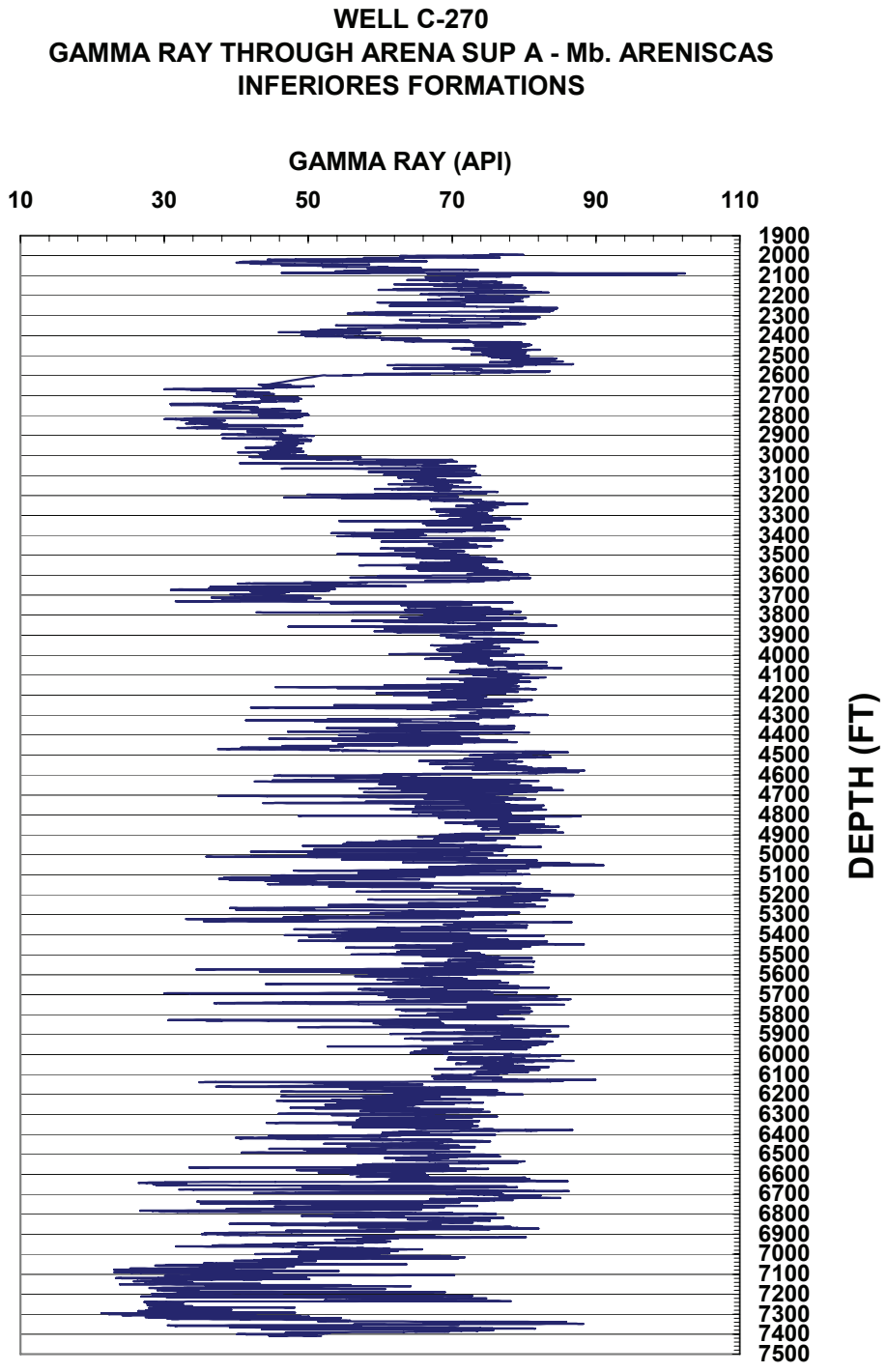

Figure 5.1 Gamma-ray log through the Arena Sup A – Mb. Areniscas Inferiores (ASA-MAI) Formations.

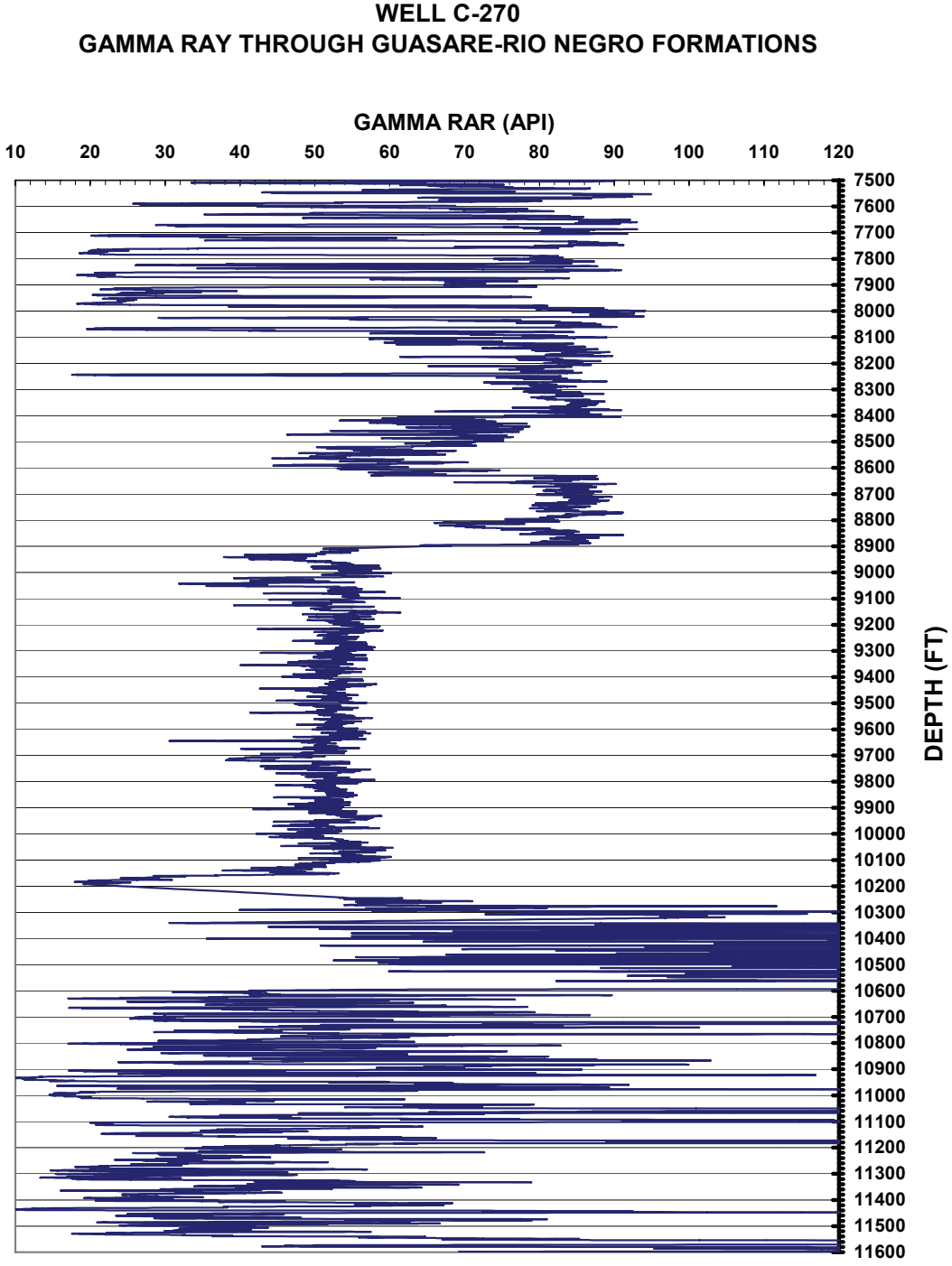

Figure 5.2 Gamma-ray log through the Guasare – Rio Negro (G-RN) Formations.

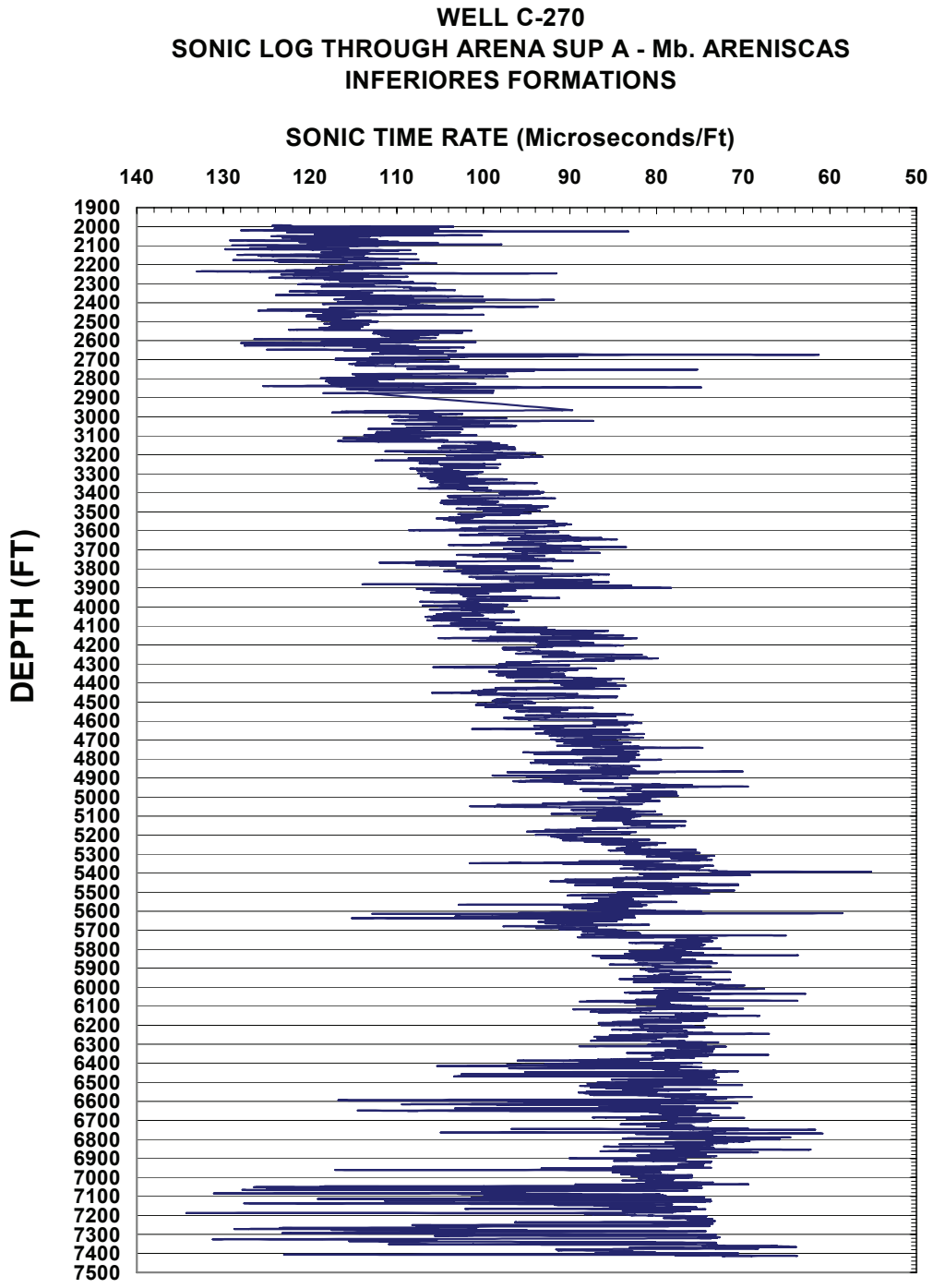

Figure 5.3 Sonic log through the Arena Sup A – Mb. Areniscas Inferiores (ASA-MAI) Formations.

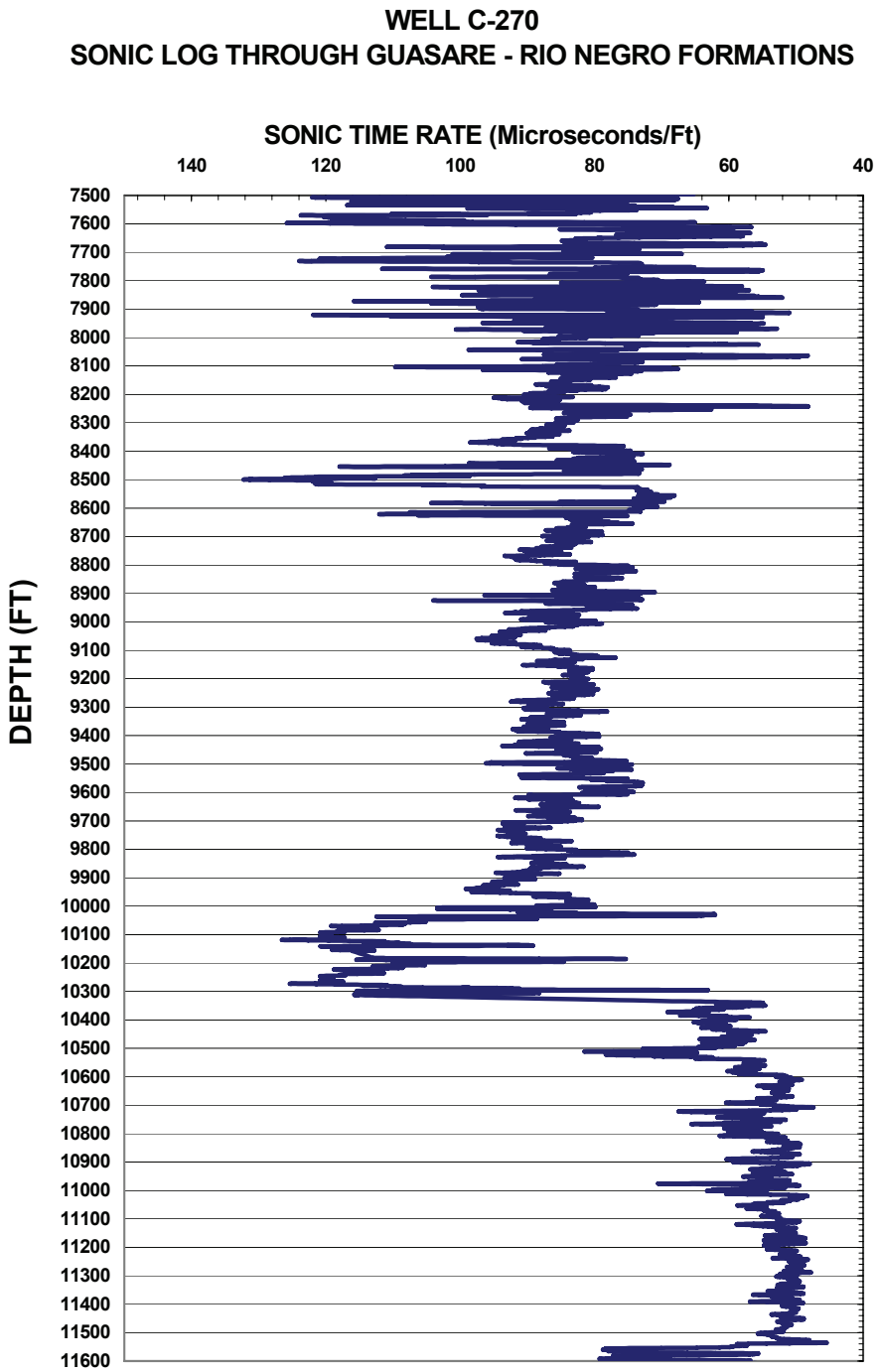

Figure 5.4 Sonic log through the Guasare – Rio Negro (G-RN) Formations.

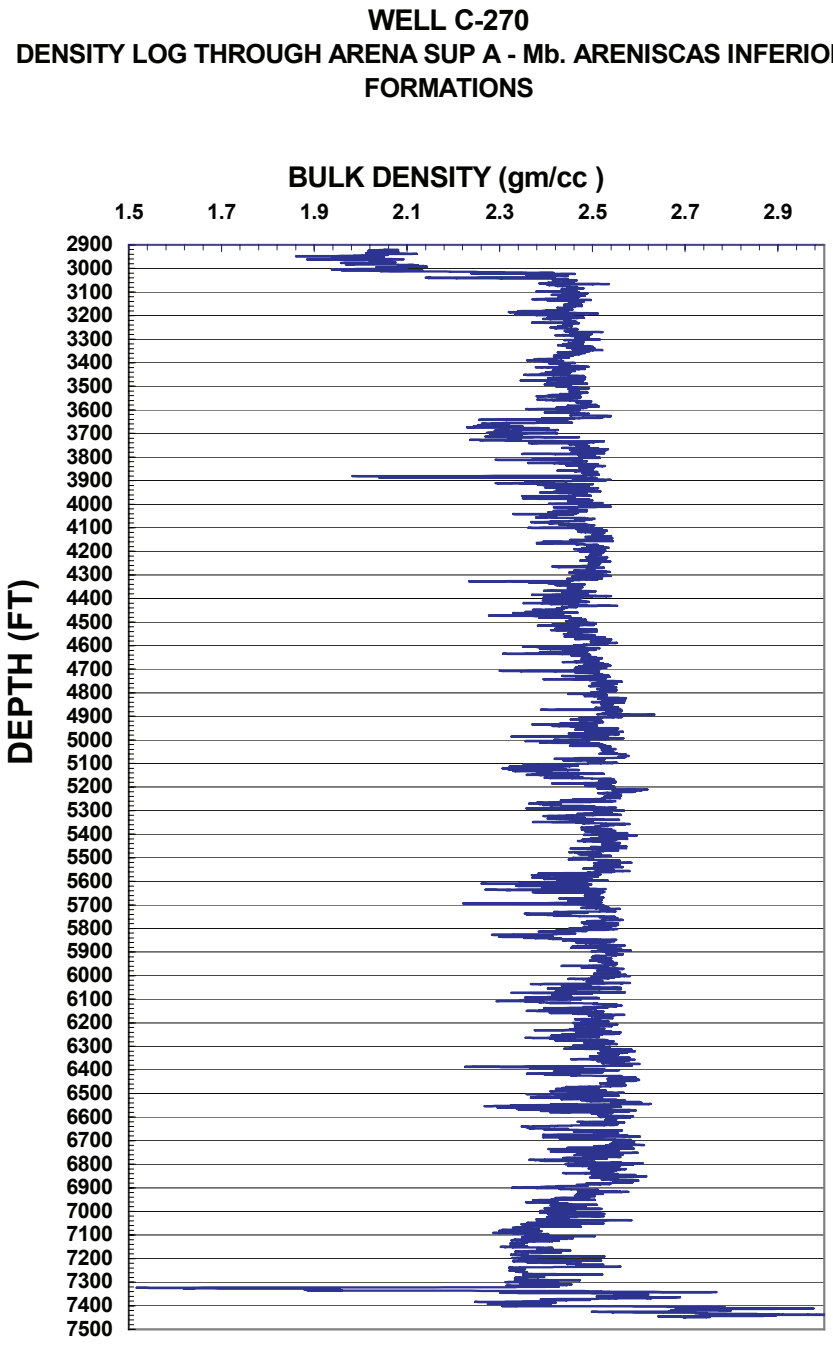

Figure 5.5 Bulk density log through the Arena Sup A – Mb. Areniscas Inferiores (ASA-MAI) Formations.

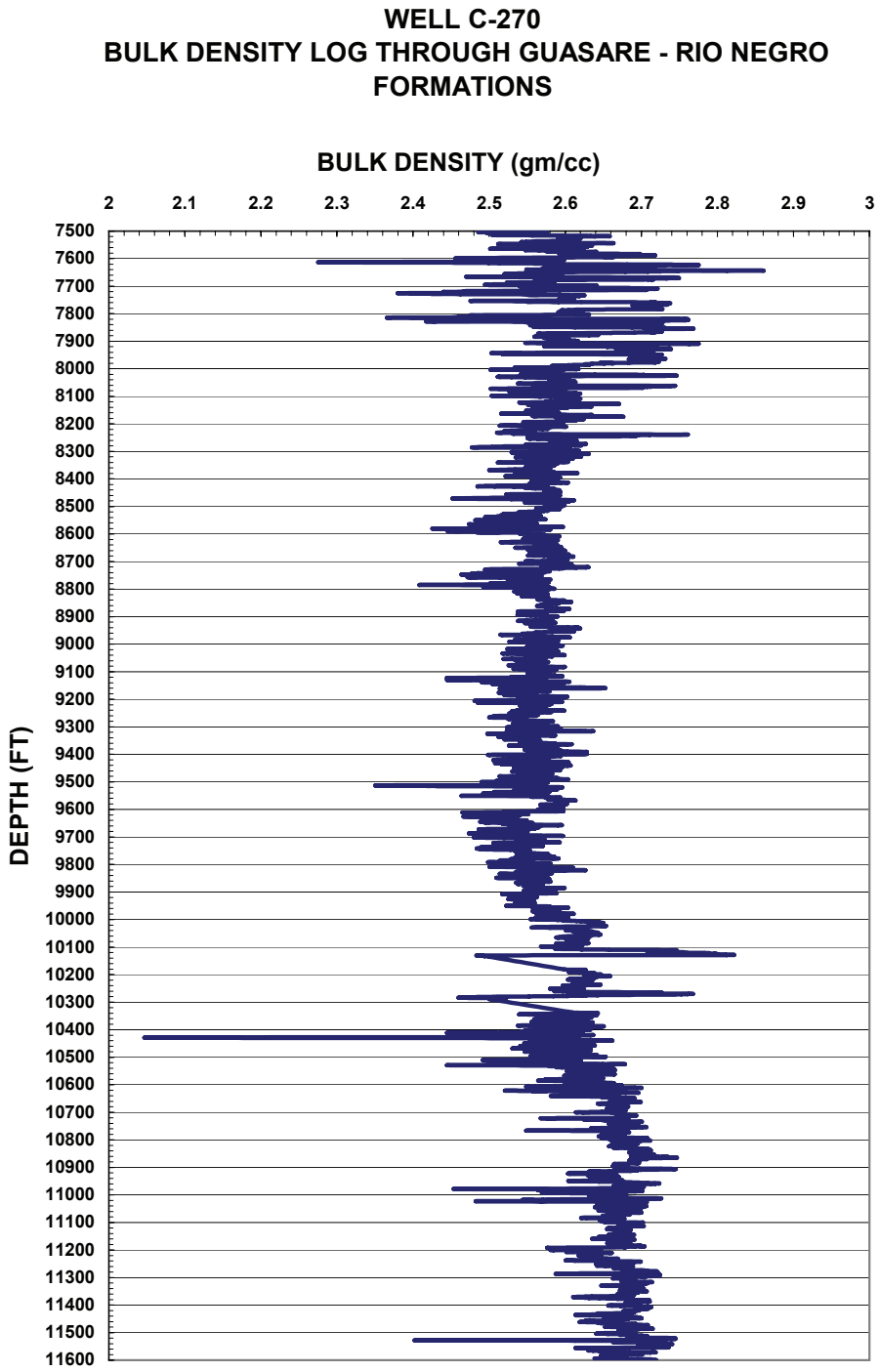

Figure 5.6 Bulk density log through the Guasare – Rio Negro (G-RN) Formations.

5.2 Velocity Analysis

Velocity dataset of LaConcepcion field consists of text files of checkshot two-way times, two-way times and root-mean square velocities from the 3-D seismic survey. The checkshot two-way times at the Borehole C-270 and the root-mean square velocity (V_{rms}) at CMP 693 of inline 164 through the ASA-MAI and G-RN Formations are shown in Tables 5.1 through 5.4 and used in calculating the interval velocities at the Borehole C-270 and CMP 693 using the Dix's formula.

The interval velocity through ASA-MAI and G-RN Formations at the Borehole C-270 is estimated from the checkshot two-way times as follows:

$$V_{\text{int}} = 2\left(\frac{d_n - d_{n-1}}{T_n - T_{n-1}}\right) \tag{5.1}$$

where d_n and d_{n-1} are the depth to the top and bottom of the interval, and T_{n-1} and T_n are the two-way times at the top and bottom of the interval.

The Dix's formula is used to calculate the interval velocities through ASA-MAI and G-RN Formations at the CMP 693 of inline 164 from the root-mean square velocities V_{rms} and the two-way travel-times T as follows:

$$V_{\text{int}} = \sqrt{\frac{V^2_{rms(n)}T_{0,n} - V^2_{rms,n-1}T_{0,n-1}}{T_0 - T_{0,n-1}}} \tag{5.2}$$

where V_{n} is the interval velocity of the rock formation, $V_{\text{rms (n)}}$ and $V_{\text{rms (n-1)}}$ are the root-mean square velocities at the base and top of the rock formation, T_0 and $T_{\text{n-1}}$ are the two-way times to the base and top of the rock formation. Equation (5.2) is referred to as the Dix's formula.

The other way to find interval velocity is the inverse of sonic log. In this study, the sonic log at Borehole C-270 is used to estimate the interval velocity through ASA-MAI and G-RN Formations. The interval velocity from the sonic log, interval velocities from the checkshot two-way times at the Borehole C-270 and that from the surface seismic survey at CMP 693 of inline164 were calculated and plotted versus depth through ASA-MAI and G-RN Formations as shown in Figures 5.7 and 5.8.

The interval velocity comparisons through ASA-MAI Formations (Figure 5.7) shows two low velocity zones, and the interval velocity comparisons through the G-RN Formations (Figure 5.8) shows one low velocity zone.

Table 5.1 Borehole C-270 checkshot two-way times and velocity through the ASA-MAI Formations.

Depth (ft)	Two-way Time (m.sec)	V_{int} (ft/sec)	V_{aveg} (ft/sec)	V_{Dix} (ft/sec)	V_{Dix} (m/sec)
1651.70	490.60	6733.39	6733.39	6733.39	2052.86
2000.30	571.00	8671.64	7006.30	8483.49	2586.43
2050.10	582.40	8736.84	7040.18	8567.16	2611.94
2100.00	592.60	9784.31	7087.41	9398.52	2865.40
2149.80	604.00	8736.84	7118.54	8582.72	2616.68
2498.40	683.20	8803.03	7313.82	8659.38	2640.05
2548.20	694.40	8892.86	7339.29	8753.84	2668.85
2598.10	706.00	8603.45	7360.06	8511.61	2595.00
2647.90	716.60	9396.23	7390.18	9176.30	2797.65
2747.40	739.00	8883.93	7435.45	8761.31	2671.13
2797.20	749.20	9764.71	7467.16	9486.72	2892.29
2847.00	759.20	9960.00	7500.00	9647.24	2941.23
2896.70	770.00	9203.70	7523.90	9046.89	2758.20
2946.50	780.60	9396.23	7549.32	9210.38	2808.04
2996.20	791.00	9557.69	7575.73	9347.14	2849.74
3045.90	801.20	9745.10	7603.34	9503.72	2897.48
3095.60	811.20	9940.00	7632.15	9664.93	2946.63
3145.20	821.00	10122.45	7661.88	8915.11	2992.41
3194.80	831.40	9538.46	7685.35	9354.40	2851.95
3244.40	841.80	9538.46	7708.24	9358.99	2853.35
3293.90	851.20	10531.91	7739.43	10150.67	3094.72
3343.40	859.80	11511.63	7777.16	10882.57	3317.86
3392.90	869.40	10312.50	7805.15	9999.53	3048.64
3491.80	889.60	9792.08	7850.27	9593.05	2924.71
3541.20	899.20	10291.67	7876.33	10001.08	3049.11

3590.50	908.40	10717.39	7905.11	10337.92	3151.81
3639.90	918.40	9880.00	7926.61	9682.80	2952.07
3689.20	928.20	10061.22	7949.15	9834.62	2998.36
3738.40	938.60	9461.54	7965.91	9341.24	2847.94
3787.60	948.20	10250.00	7989.03	9994.91	3047.23
3836.70	957.20	10911.11	8016.51	10516.37	3206.21
3885.80	967.00	10020.41	8036.81	9820.06	2993.92
3934.70	976.00	10866.67	8062.91	10495.25	3199.77
3983.60	985.00	10866.67	8088.53	10502.15	3201.88
4032.50	994.60	10187.50	8108.79	9971.06	3039.96
4130.20	1012.40	10977.53	8159.23	10602.88	3232.59
4179.00	1022.00	10166.67	8178.08	9968.41	3039.15
4276.50	1040.00	10833.33	8224.04	10508.70	3203.87
4325.20	1048.80	11068.18	8247.90	10699.69	3262.10
4374.00	1057.80	10844.44	8269.99	10531.73	3210.89
4422.70	1066.60	11068.18	8293.08	10711.65	3265.75
4471.50	1075.40	11090.91	8315.98	10735.20	3272.93
4520.30	1084.20	11090.91	8338.50	10741.07	3274.72
4569.10	1092.60	11619.05	8363.72	11150.02	3399.40
4666.60	1109.20	11746.99	8414.35	11256.84	3431.96
4715.30	1118.00	11068.18	8435.24	10747.90	3276.80
4764.10	1126.60	11348.84	8457.48	10971.41	3344.94
4861.70	1143.80	11348.84	8500.96	10980.07	3347.58
4959.00	1161.00	11313.95	8542.64	10964.03	3342.69
5007.60	1169.40	11571.43	8564.39	11170.96	3405.78
5056.20	1177.40	12150.00	8588.75	11612.63	3540.44
5104.80	1186.00	11302.33	8608.43	10974.17	3345.78
5153.40	1194.20	11853.66	8630.72	11403.95	3476.81
5202.00	1202.60	11571.43	8651.26	11194.22	3412.87
5396.10	1236.40	11485.21	8728.73	11139.94	3396.32

5494.00	1252.20	12392.41	8774.96	11845.61	3611.47
5543.10	1260.20	12275.00	8797.18	11768.73	3588.03
5592.30	1268.00	12615.38	8820.66	12027.42	3666.90
5838.80	1307.80	12386.93	8929.19	11878.76	3621.57
5887.90	1316.20	11690.48	8946.82	11361.83	3463.97
6084.00	1350.20	11535.29	9012.00	11248.62	3429.46
6132.90	1357.80	12868.42	9033.58	12280.37	3744.02
6279.00	1380.20	13044.64	9098.68	12423.17	3787.55
6376.60	1396.00	12354.43	9135.53	11922.75	3634.99
6523.00	1419.40	12512.82	9191.21	12056.23	3675.68
6668.90	1443.00	12364.41	9243.10	11957.18	3645.48
6815.10	1465.20	13171.17	9302.62	12581.09	3835.70
6863.90	1472.60	13189.19	9322.15	12606.55	3843.46
6961.50	1487.40	13189.19	9360.63	12615.45	3846.17
7059.20	1502.00	13383.56	9399.73	12770.79	3893.53
7205.90	1522.40	14382.35	9466.50	13504.01	4117.08
7254.80	1529.20	14382.35	9488.36	13520.13	4121.99
7303.70	1536.00	14382.35	9510.03	13528.01	4124.39
7352.60	1542.80	14382.35	9531.50	13535.77	4126.76
7450.40	1556.40	14382.35	9573.89	13547.21	4130.25

Table 5.2 CMP gather 693 two-way times and calculated velocity and depth through the ASA-MAI Formations.

Two-way times (sec)	t (sec)	Vrms (m/sec)	Vint (m/sec)	Vint (ft/sec)	Thickness (meters)	Cumulative Depth (meters)	Thickness (ft)	Cumulative Depth (ft)
0.384	0.384	2120	2120.00	6953.60	407.04	1335.09	1335.09	1335.09
0.562	0.178	2273	2572.26	8437.01	228.93	750.89	750.89	2085.98
0.650	0.088	2350	2792.11	9158.11	122.85	402.96	402.96	2488.94
0.766	0.116	2400	2662.86	8734.18	154.45	506.58	506.58	2995.52
0.892	0.126	2550	3319.10	10886.65	209.10	685.86	685.86	3681.38
1.082	0.190	2656	3105.65	10186.53	295.04	967.72	967.72	4649.10
1.180	0.098	2751	3638.58	11934.55	178.29	584.79	584.79	5233.90
1.470	0.290	2950	3649.48	11970.31	529.18	1735.69	1735.69	6969.59

Table 5.3 Borehole C-270 checkshot two-way times and velocity through the G-RN Formations.

Depth (ft)	Two-way Time(m.sec)	V_{int} (ft/sec)	V_{aveg} (ft/sec)	V_{Dix} (ft/sec)	V_{Dix} (m/sec)
7352.60	1542.80	9531.50	9531.50	9531.50	2905.95
7450.40	1556.40	14382.35	9573.89	13547.21	4130.25
7645.80	1582.80	1480.03	9661.11	13865.13	4227.17
7743.60	1597.60	13216.22	9694.04	12733.68	3882.22
7792.50	1605.00	13216.22	9710.28	12740.48	3884.29
7939.30	1628.60	12440.68	9749.85	12141.80	3701.77
7988.20	1636.60	12225.00	9761.95	11973.06	3650.32
8086.10	1652.20	12551.28	9788.28	12240.41	3731.83
8233.00	1674.00	13477.06	9836.32	12969.25	3954.04
8282.00	1681.00	14000.00	9853.66	13369.22	4075.98

8429.00	1705.60	11951.22	9883.91	11768.40	3587.93
8674.00	1745.20	12373.74	9940.41	12126.45	3697.09
8771.90	1763.00	11000.00	9951.11	10949.37	3338.22
8820.90	1771.80	11136.36	9956.99	11073.42	3376.04
8918.80	1789.00	11383.72	9970.71	11294.83	3443.54
9653.70	1923.80	10903.56	10036.07	10866.39	3312.92
10140.00	1985.00	15892.16	10216.62	14809.60	4515.12
10188.90	1990.40	18111.11	10238.04	16305.17	4971.09
10384.60	2012.40	17790.91	10320.61	16127.44	4916.90
10482.60	2022.80	18846.15	10364.45	16818.63	5127.63
10678.90	2042.20	20237.11	10458.23	17691.72	5393.82
10924.60	2066.00	20647.06	10575.61	17991.24	5485.13
11170.70	2092.80	18365.67	10675.36	16655.03	5077.75
11337.90	2115.60	17288.25	10746.74	15994.98	4876.52
11466.60	2125.80	19352.94	10788.03	17344.31	5287.90
11664.80	2146.00	19623.76	10871.20	17543.00	5348.48

Table 5.4 CMP gather 693 two-way times and calculated velocity and depth through G-RN Formations.

Two-times (sec)	t (sec)	V_{rms} (m/sec)	V_{int} (m/sec)	V_{int} (ft/sec)	Thickness (meters)	Cumulative Depth (meters)	Thickness (ft)	Cumulative Depth (ft)
1.648	1.648	3000.00	3000.00	9840.00	2472.00	2472.00	8108.16	8108.16
1.818	0.170	3121.00	4113.45	13492.13	349.64	2821.64	1146.83	9254.99
1.954	0.136	3109.00	2943.89	9655.97	200.18	3021.83	656.61	9911.60
2.028	0.074	3161.00	4312.90	14146.32	159.58	3181.41	523.41	10435.01
2.114	0.086	3223.00	4440.88	14566.06	190.96	3372.36	626.34	11061.35
2.208	0.094	3280.00	4369.73	14332.72	205.38	3577.74	673.64	11734.99

INTERVAL VELOCITY COMPARISONS FROM 1900-7410 FT (THE ARENA SUP A – Mb. ARENISCAS INFERIORES)

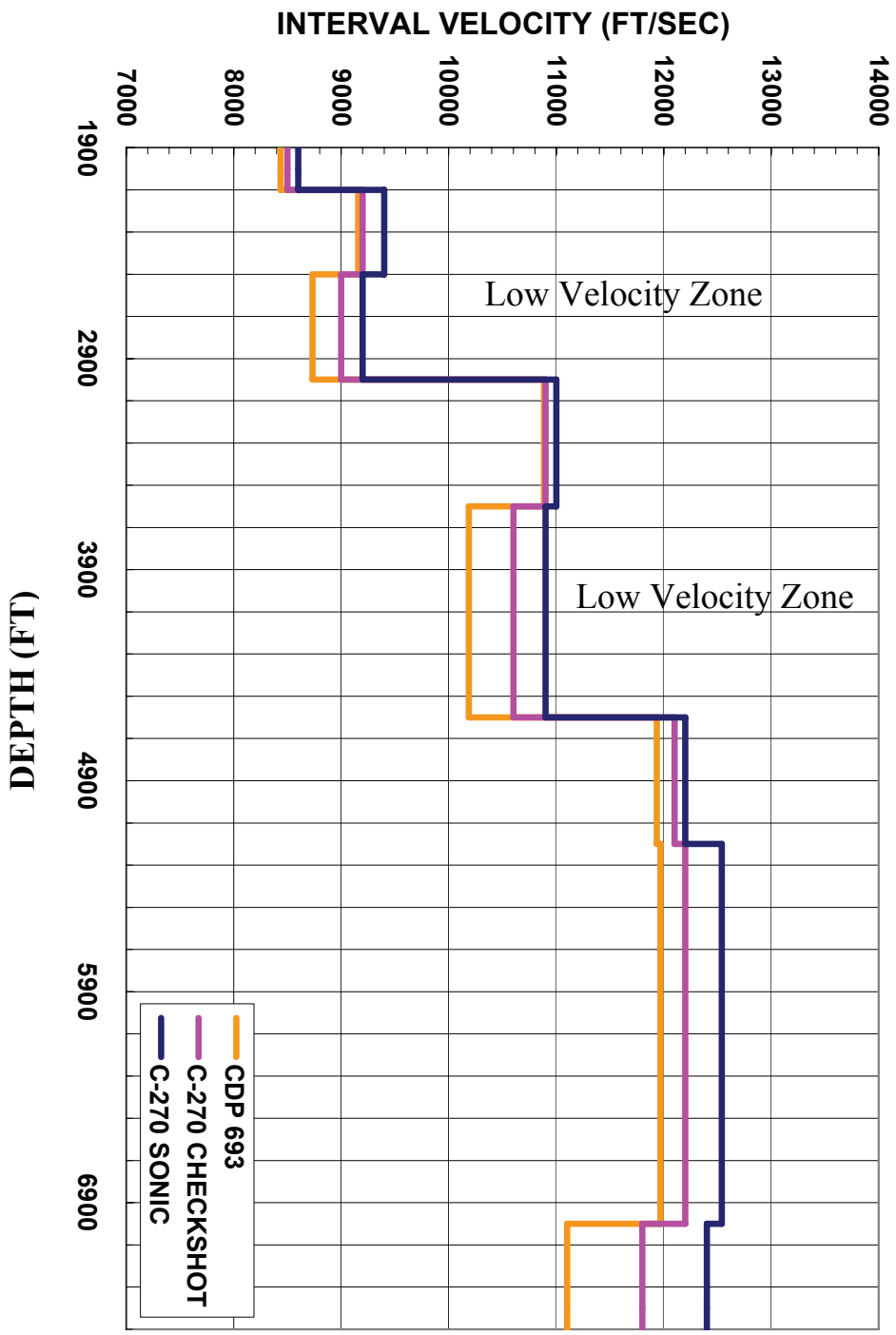

Figure 5.7 Interval velocity comparisons through the Arena Sup A – Mb. Areniscas Inferiores (ASA-MAI) Formations.

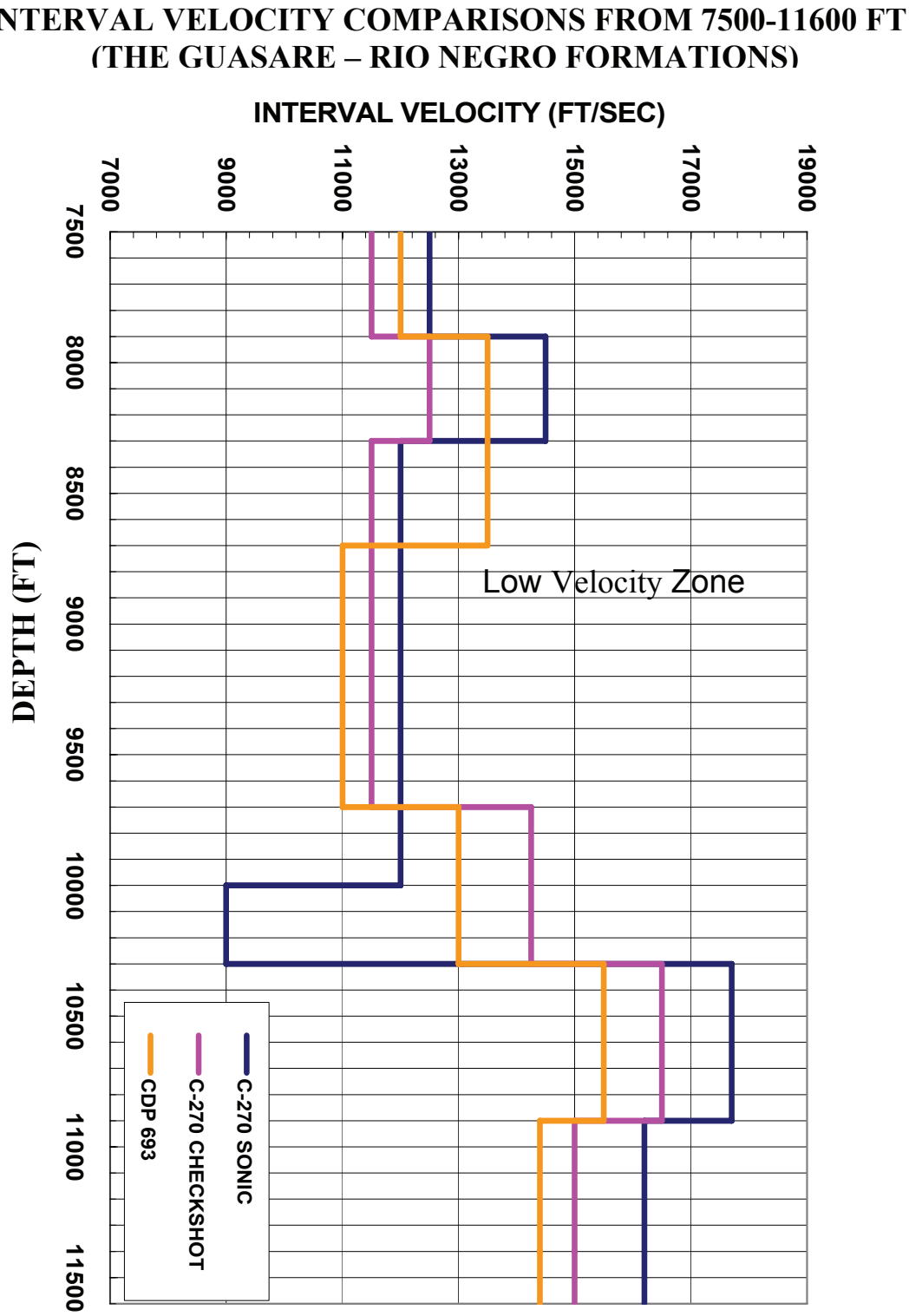

Figure 5.8 Interval velocity comparisons through the Guasare – Rio Negro (G-RN).

The results from the above section show that the interval velocity comparisons through the ASA-MAI Formations (Figure 5.7) indicate two low velocity zones, and the interval velocity comparisons through G-RN Formations (Figure 5.8) shows one low velocity zone as a result of fault and fracture effects on the seismic response. The following section presents the peak frequency technique in order to validate the existence of fracture effects on the seismic response of the ASA-MAI and G-RN Formations.

5.3 Windowed Fourier Transform

Application of the Fourier transform analysis on the CMP gathers was chosen for estimating the waveform attenuation owing to the effects of faults/ fractures fluid saturation effects. This section deals with the determination of the value of the peak frequency and monitoring its shift toward the origin owing to the seismic wave attenuation in each amplitude-frequency spectrum time window.

What is important for the Fourier transform application is not the average frequency but the peak frequency at the highest amplitude for a distinct frequency, as its inverse transform is a composite waveform. Therefore, owing to the incipient noise, we chose to be consistent by taking the average of the top three peaks (Figure 5.9). Doing so allows the approximation of the dominant frequency without the bias of using only one discrete peak that may not accurately reflect the transform.

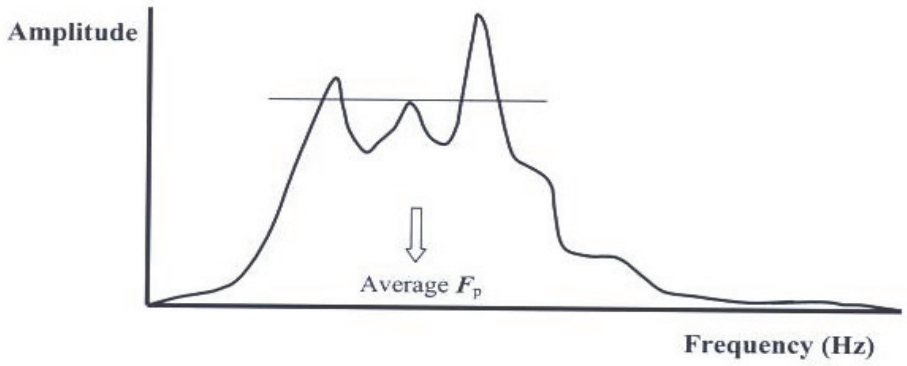

Figure 5.9 Operational procedure for selecting mean peak frequency: take the average of top three peaks.

Due to the lack of CMP gathers for the inline 164, this study used inline 249 (Figure 5.10) as the nearest for which the CMP gathers are available. Figure 5.10 shows the locations of the selected six CMP gathers for the Fourier transforming analysis, and the live CMP gathers are shown in Figure 5.11.

These selected CMP gathers cover the unfractured zones, fractured zone, and fault zones. For each CMP gather the amplitude-frequency spectrum was conducted at five rock formations or time windows (Figures 5.12 through 5.17). Since the uppermost window (Miocene Formations) of each CMP gather is small, its amplitude-frequency spectrum was chosen to be the reference for the middle two windows (ASA-MAI Formations), and the lower two windows (G-RN Formations). The values of the peak frequency of the six CMP gathers (Figure 5.11) are summarized in Table 5.5.

The CMP gathers 600 and 558 (Figure 5.11) of the inline 249 cover the highly fractured zone. The seismic waves of the surface seismic survey are strongly attenuated as indicated by the low amount of the peak frequency values at CMP gathers as shown in Table 5.5.

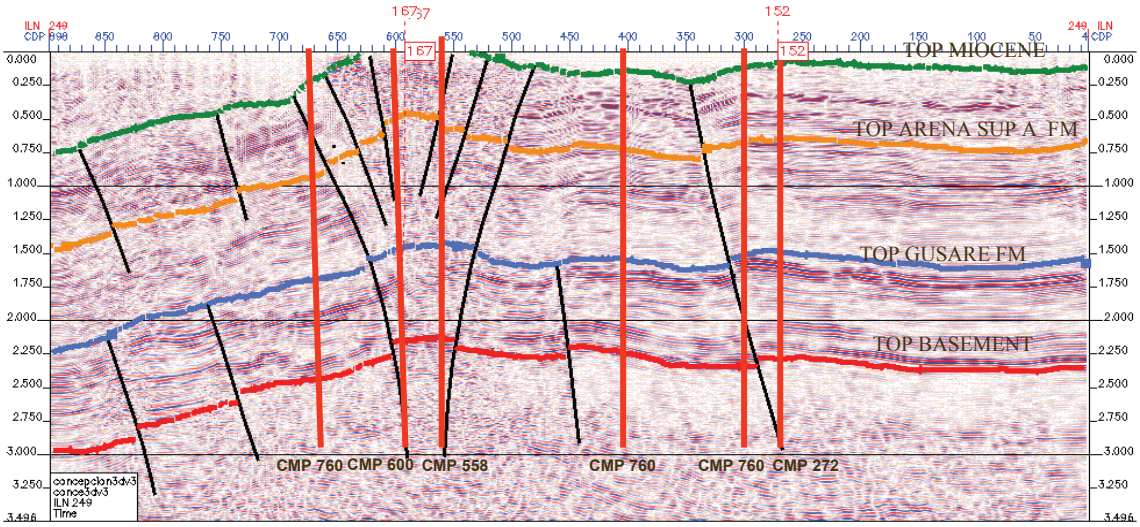

Figure 5.10 Seismic inline 249 showing the locations of the selected CMP gathers for the windowed Fourier transform.

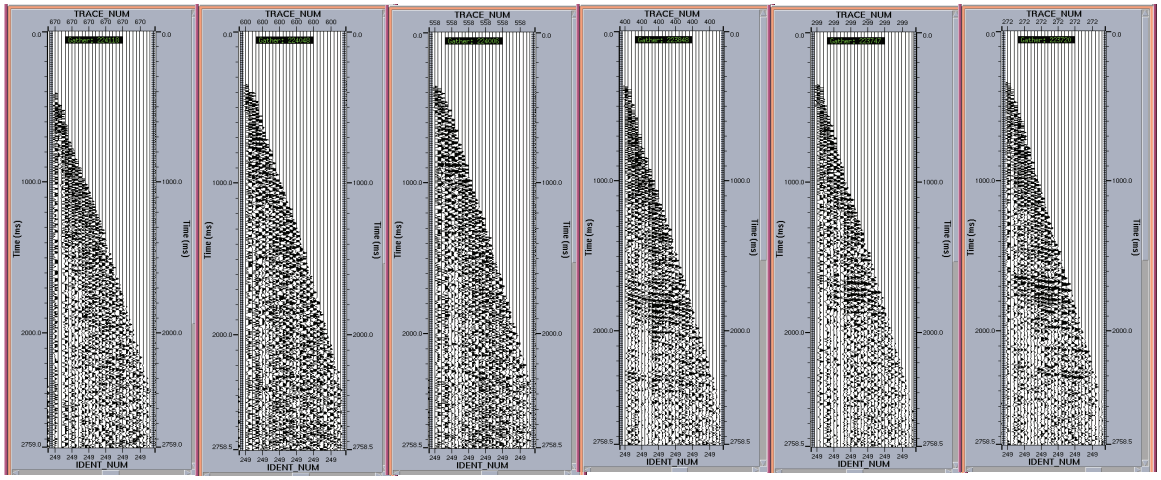

CMP 670 CMP 600 CMP 558 CMP 400 CMP 300 CMP 272

Figure 5.11 The selected CMP gathers of the seismic inline 249 shown in Figure 5.10.

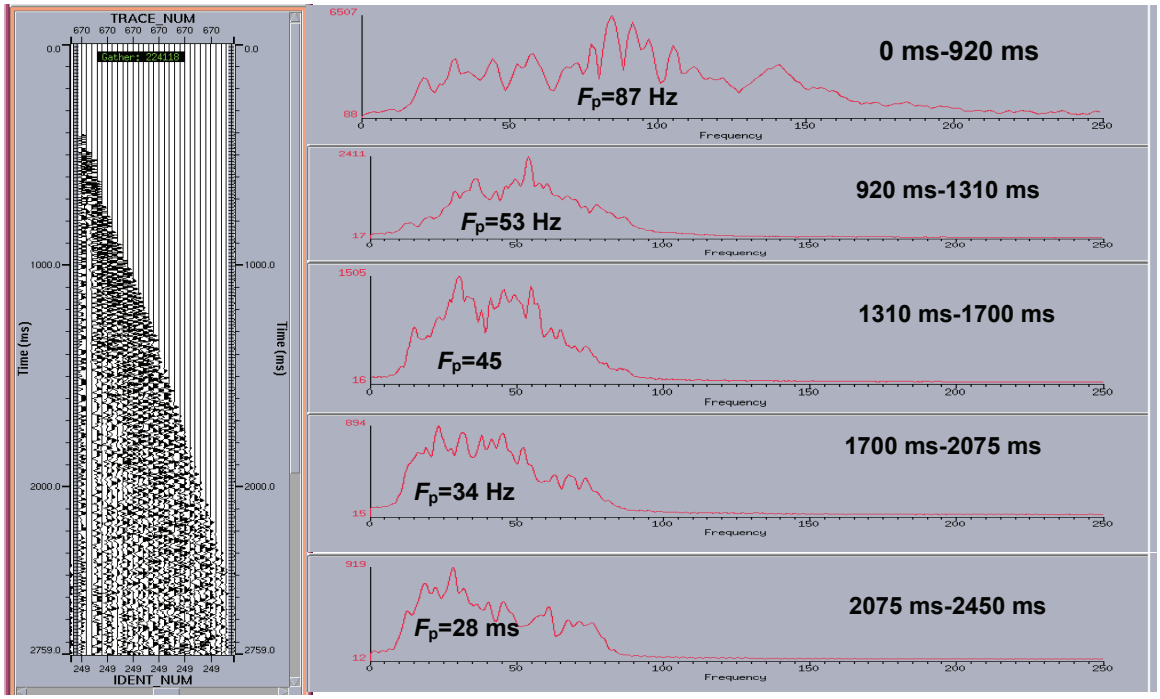

Figure 5.12 Peak frequency shift for CMP 670 of inline 249. (unfractured zone).

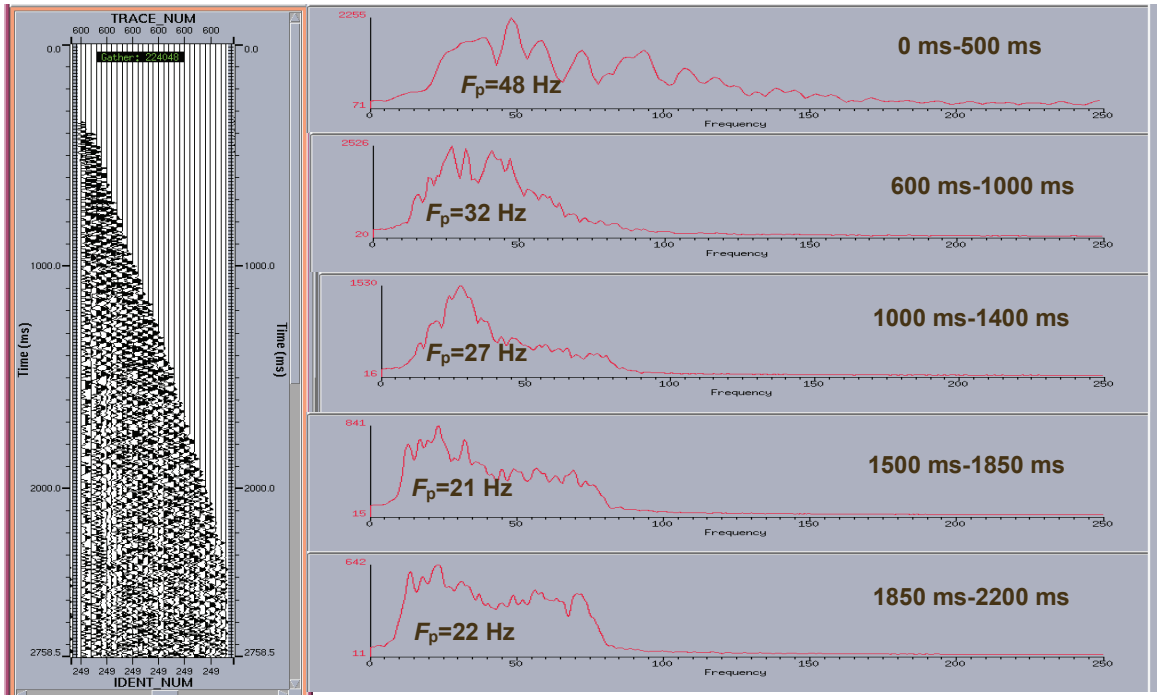

Figure 5.13 Peak frequency shift for CMP 600 of inline 249. (fractured zone).

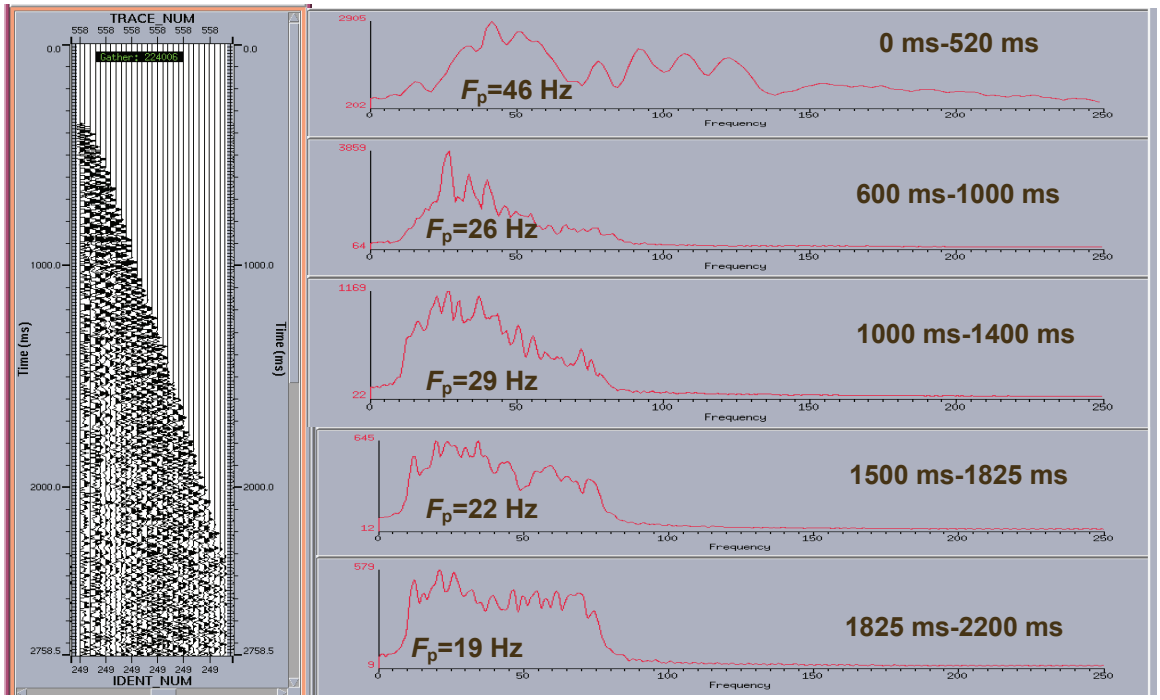

Figure5.14 Peak frequency shift for CMP 558 of inline 249. (fractured zone).

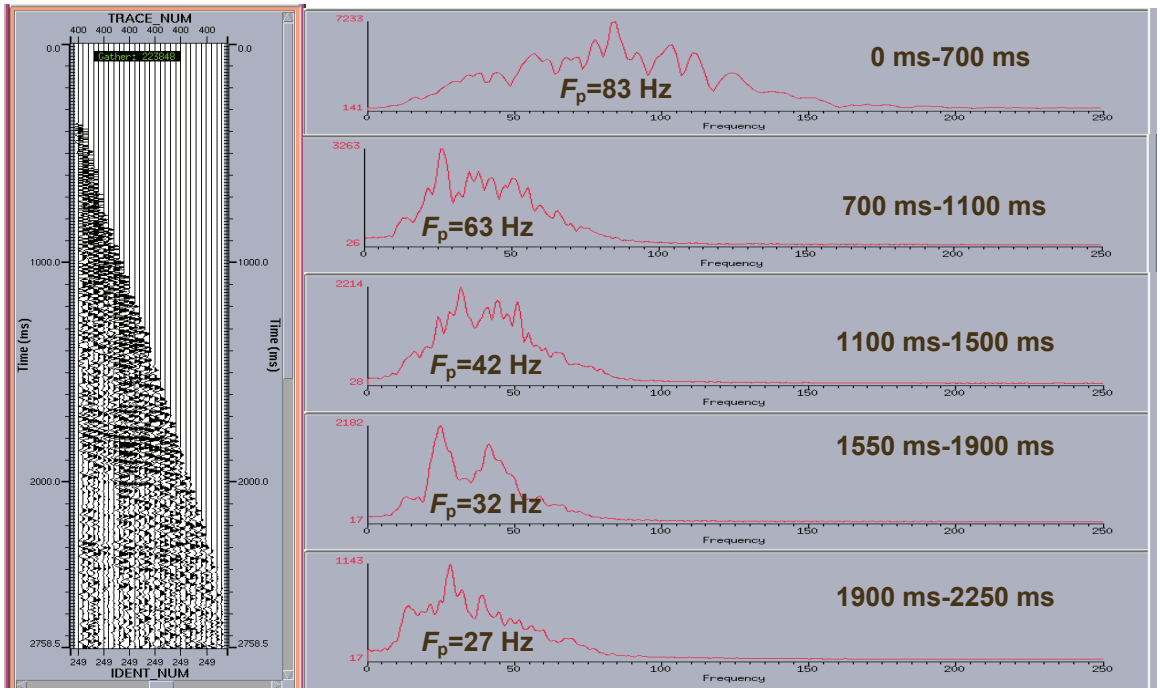

Figure 5.15 Peak frequency shift for CMP 400 of inline 249. (unfractured zone).

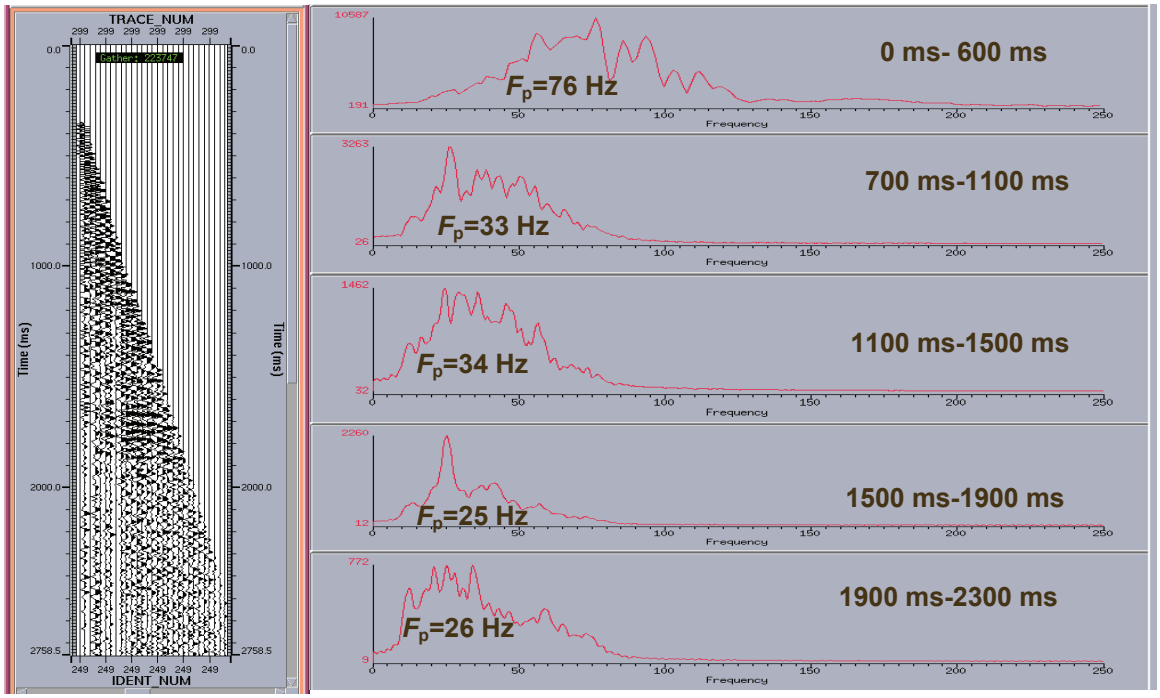

Figure 5.16 Peak frequency shift for CMP 300 of inline 249. (fault zone).

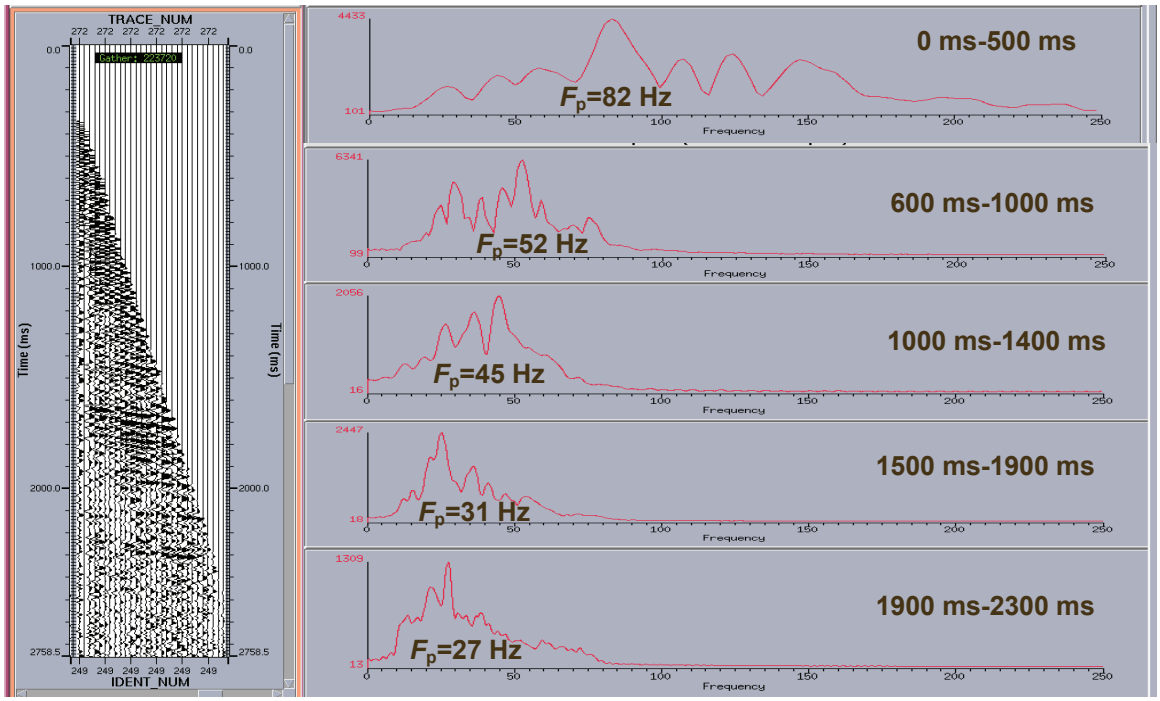

Figure 5.17 Peak frequency shift for CMP 272 of inline 249. (unfractured zone).

Table 5.5 Peak frequency for CMP gathers of inline 249. Peak frequencies (F_p) are indicative of relative attenuation in different time windows. Important data in bold. (for approximate time reference, see Figures 5.12-5.17).

Name of Formation	Peak Frequency (Hz)	CMP Number					
		670 Unfractured Zone	600 Fractured Zone	558 Fractured Zone	400 Unfractured Zone	300 Fault Zone	272 Unfractured Zone
Miocene Formations	F_p	87	**48**	**51**	83	**70**	82
Arena Sup A – Mb. Areniscas Inferiores Formations (Upper Window)	F_p	53	**32**	**26**	52	**53**	52
Arena Sup A – Mb. Areniscas Inferiores Formations (Lower Window)	F_p	45	**27**	**26**	42	**34**	45
Guasare – Rio Negro Formations (Upper Window)	F_p	34	**21**	**22**	32	**25**	31
Guasare – Rio Negro Formations (Lower Window)	F_p	28	**22**	**19**	27	**26**	27

5.4 Summary and Conclusions

Interval velocities from the surface seismic survey, checkshot two-way times, and sonic time rate were estimated through the ASA-MAI and G-RN Formations and the peak frequency shifts for six selected CMP gathers were estimated at five time windows for each of the above rock formations. The

interval velocity comparisons indicate low velocity zones through the ASA-MAI and G-RN Formations and suggest possible fluid effects proximal to permeable fault zones. The Fourier transform analysis through the ASA-MAI and G-RN Formations of La Concepcion field reveals that the peak frequency shifts at the fractured zones are lower than those at the unfractured zones, suggesting fluid effects or leaking faults. The magnitude of fracture effects on the seismic waves propagating through the ASA-MAI and G-RN Formations of La Concepcion field is discussed in details in chapter six.

CHAPTER 6

MAGNITUDE OF FRACTURE EFFECTS

6.1 Total Travel-times Through The Arena Sup A – Mb. Areniscas Inferiores (ASA-MAI) And Guasare – Rio Negro (G-RN) Formations

The total amount of travel-times $\Delta t(\mu \sec)$ it takes the sonic log, checkshot seismic waves, and the surface seismic waves to pass through ASA-MAI Formations, and the G-RN Formations can be taken as a measure of the magnitude of fractures effects on the seismic velocity of the surface seismic survey through La Concepcion field rock formations.

In the following sections the researcher calculates the amount of the total travel-times of the sonic log, checkshot seismic waves, and the CMP gather 693 of the inline 164 of the surface seismic survey through ASA-MAI Formations, and G-RN Formations and compare the results.

6.1.a. i. Sonic Total Travel-times Through The Arena Sup A – Mb. Areniscas Inferiores (ASA-MAI) Formations

The sonic log plot at the Borehole C-270 is shown in Figure 5.2. The total traveltime it takes the acoustic wave to pass through the through ASA-MAI Formations is calculated from sonic log text file using the following integral equation:

$$\Delta T_{total}(\mu \sec) = \int_{z1}^{z2} \Delta T dz \tag{6.1}$$

$$= \Delta T \int_{z1}^{z2} dz$$

$$= \Delta T(Z2 - z1)$$

$$= \Delta T(7410 ft - 1991 ft)$$

$$= \Delta T(5419 ft)$$

$$= \left(\frac{\sum_{i=1}^{n} \Delta T_i}{n} \right) 5419 \quad ft$$

$$= \left(\frac{1971008 \quad \mu \sec}{21323 \quad ft} \right) * \ 5419 \quad ft$$

$$= \ 92 \ \left(\frac{\mu \ \sec}{ft} \right) * \ 5419 \quad ft$$

$$= 498548 \mu \sec .$$

$$= 0.498548 \sec .$$

$$= 498 m. \sec .$$

where Z is the thickness of the formation, and n is the number of T samples, and T is the time rate of the sonic log through ASA – MAI Formations and estimated as 92.4359 *(sec/ft)*.

6.1.a.ii. Checkshot Total Travel-times Through The Arena Sup A – Mb. Areniscas Inferiores (ASA-MAI) Formations

The checkshot total travel-times $\Delta T(\mu \sec)$ of the well C-270 through ASA – MAI Formations can be calculated using equation (6.1) as follows:

$$\Delta T_{total}(\mu \sec) = \Delta T(\mu \tfrac{\sec}{ft}) * 5410\, ft$$

$$= 94\left(\tfrac{\mu \sec}{ft}\right) * 5419\, ft$$

$$= 509386 \mu \sec.$$

$$= 0.509 \sec.$$

$$= 509 m.\sec.$$

6.1.a.iii. Seismic Total Travel-times Through The Arena Sup A – Mb. Areniscas Inferiores (ASA-MAI) Formations

The total traveltime $\Delta T(\mu \sec)$ it takes the seismic waves to travel through ASA-MAI Formations at CMP 693 of inline 164 is calculated from the two-way times using equation (6.1) and displayed in Table 6.2 :

$$\Delta T_{total}(\mu \sec) = \Delta T(\mu \tfrac{\sec}{ft}) * 5419\, ft$$

$$= 99\left(\tfrac{\mu \sec}{ft}\right) * 5419\, ft$$

$$= 535590\ \mu \sec .$$

$$= 0.535590\ \sec .$$

$$= 536 m.\sec .$$

The average time rate, and average interval velocity of sonic log, checkshot, and seismic survey through ASA-MAI Formations are compared below:

$$(\Delta t_{ave})_{sonic} < (\Delta t_{ave})_{checkshot} < (\Delta t_{ave})_{seismic.}$$

$$92\ \mu\ sec/ft < 94\ \mu\ sec/ft < 99\ \mu\ sec/ft$$

and

$$(\Delta t_{total})_{sonic} < (\Delta t_{total})_{checkshot} < (\Delta t_{total})_{seismic.}$$

$$498548\ \mu\ sec. < 509386\ \mu\ sec. < 535590\ \mu\ sec.$$

$$498 m.\ sec. < 509\ m.\ sec. < 536\ m.\ sec.$$

The corresponding average of interval velocities through ASA-MAI Formations are:

$$(V_{int})_{sonic} > (V_{int})_{checkshot} > (V_{int})_{seismic}$$

$$10869 \text{ ft/sec.} > 10638 \text{ ft/sec.} > 10101 \text{ ft/sec.}$$

$$3314 \text{ m/sec.} > 3243 \text{ m/sec.} > 3079 \text{ m/sec.}$$

The above calculations of the total travel-times were made for the sonic, checkshot and seismic waves. Results show that the seismic waves travel trough ASA-MAI Formations take longer time than sonic and checkshots.

6.1.b. i. Sonic Total Travel-times Through The Guasare – Rio Negro (G-RN) Formations

Following the same procedure, the total travel-times it takes the acoustic wave to pass through G-RN Formations is calculated from sonic log text file using the integral equation (6.1):

$$\Delta T_{total}(\mu \sec) = \int_{z1}^{z2} \Delta T dz$$

$$= \Delta T \int_{z1}^{z2} dz$$

$$= \Delta T(Z2 - z1)$$

$$= \Delta T(11600\,ft - 7500\,ft)$$

$$= \Delta T(4190\,ft)$$

$$= \left(\frac{\sum_{i=1}^{n} \Delta T_i}{n} \right) * 4100 \quad ft$$

$$= \left(\frac{747251 \quad \mu \sec}{11153 \quad ft} \right) * 4100 \quad ft$$

$$= 67\ \left(\frac{\mu\ \text{sec}}{ft}\right) * 4100\quad ft$$

$$= 274700\,\mu\,\text{sec}.$$

$$= 0.274700\,\text{sec}.$$

$$= 275m.\text{sec}.$$

where Z is the thickness of the formation, and n is the number of T samples, and T is the time rate of the sonic log through G-RN Formations and is estimated as 67 *(sec/ft)*.

6.1.b.ii. Checkshot Total Travel-times Through The Guasare –Rio Negro (G-RN) Formations

The Checkshot total traveltime $\Delta T(\mu\,\text{sec})$ of the well C-270 through the G-RN Formations can be calculated using equation (6.1) as follows:

$$\Delta T_{total}(\mu\,\text{sec}) = \Delta T(\mu\,\tfrac{\text{sec}}{ft}) * 4100\,ft$$

$$= 71\left(\frac{\mu\,\text{sec}}{ft}\right) * 4100\,ft$$

$$= 291100\,\mu\,\text{sec}.$$

$$= 0.291100\,\text{sec}.$$

$$= 291m.\text{sec}.$$

6.1.b.iii. Seismic Total Travel-times Through The Guasare – Rio Negro (G-RN) Formations

The total travel-times $\Delta T(\mu \sec)$ it takes the seismic waves to travel through G-RN Formations at CMP 693 of inline 164 is calculated from the two-way times using equation (6.1).

$$\Delta T_{total}(\mu \sec) = \Delta T(\mu \tfrac{\sec}{ft}) * 4100\, ft$$

$$= 72\left(\tfrac{\mu \sec}{ft}\right) * 4100\, ft$$

$$= 295200\ \mu \sec .$$

$$= 0.295 \sec .$$

$$= 295 m.\sec .$$

The average time rate, and average interval velocity of sonic log, checkshot, and seismic survey through G-RN Formations are compared below:

$$(\Delta t_{ave})_{sonic} < (\Delta t_{ave})_{checkshot} < (\Delta t_{ave})_{seismic}$$

$$67\ \mu sec/ft < 71\ \mu sec/ft < 72\ \mu sec/ft$$

and

$$(\Delta t_{total})_{sonic} < (\Delta t_{total})_{checkshot} < (\Delta t_{total})_{seismic.}$$

280730 μ *sec.* < 298495 μ *sec.* < 301680 μ *sec.*

281 *m. sec.* < 298 *m. sec.* < 302 *m. sec.*

The corresponding of interval velocities through G-RN Formations are:

$$(V_{int})_{sonic} > (V_{int})_{checkshot} > (V_{int})_{seismic}$$

14925 ft/sec. > 14084 ft/sec. > 13889 ft/sec.

4550 m/sec. > 4294 m/sec. > 4234 m/sec.

The above calculations of the total travel-times were made for the sonic, checkshot and seismic waves. Results indicate that it take the seismic waves to travel through G-RN Formations longer time than sonic and checkshots. The following section presents details about the seismic quality factor Q as a method of predicting the physical properties of the faults.

6.2. Quality Factor *Q*

The seismic quality factor $Q_{seismic}$ of the seismic waves passing through the ASA-MAI and G-RN Formations of La Concepcion field is calculated using the peak frequency shifts and amplitude frequency spectrum from the six selected CMP gathers of inline 249. The values of $Q_{seismic}$ were calculated using equations (2.27) and (2.31). For each amplitude frequency spectrum, there is one value of $Q_{seismic}$. This $Q_{seismic}$ is determined at the peak frequency value. The amplitude (wavelet) of each amplitude frequency spectrum is normalized to one at the peak frequency.

The plots of the normalized amplitude spectra are shown in Figures 6.1 through 6.6, and the values of the peak frequency and the calculated quality factor $Q_{seismic}$ within the Miocene, ASA-MAI , and G-RN Formations are summarized in Table 6.1.

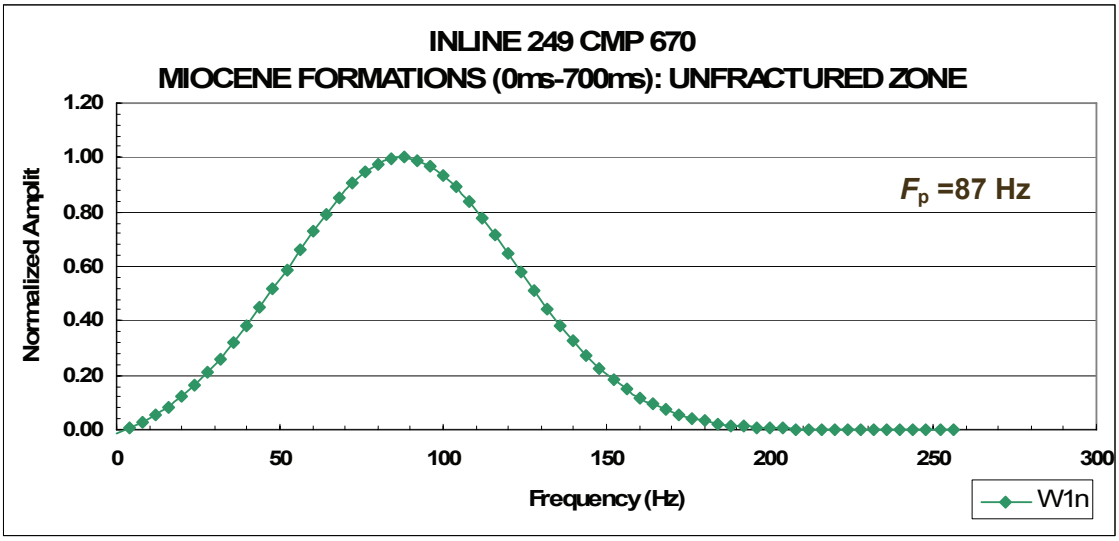

Figure 6.1.a Normalized amplitude-frequency spectrum for 0.0 ms -700 ms of CMP 670 of inline 249 (unfractured zone).

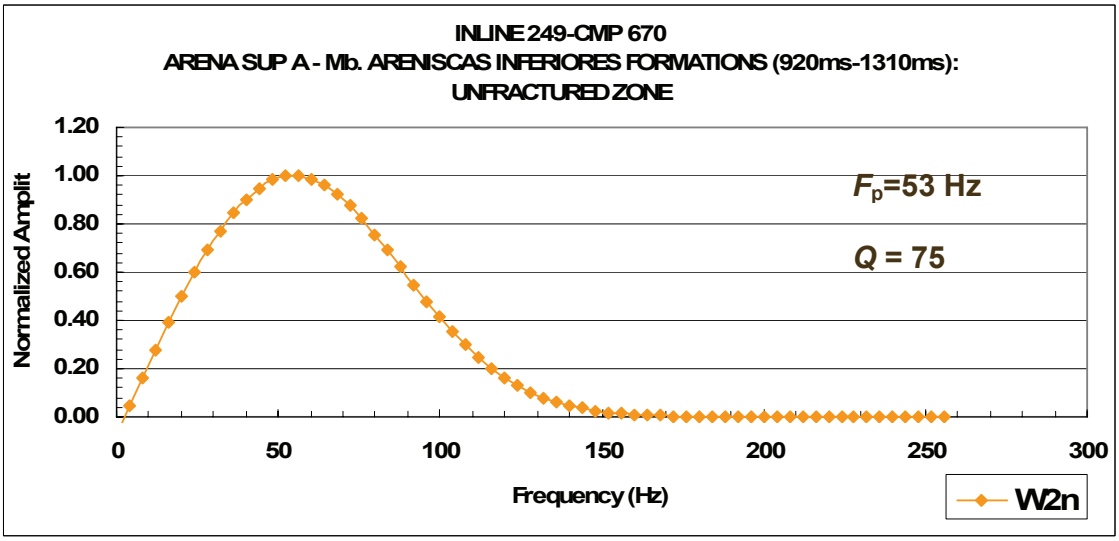

Figure 6.1.b. Normalized amplitude-frequency spectrum for 920 ms -1310 ms of CMP 670 of inline 249 (unfractured zone).

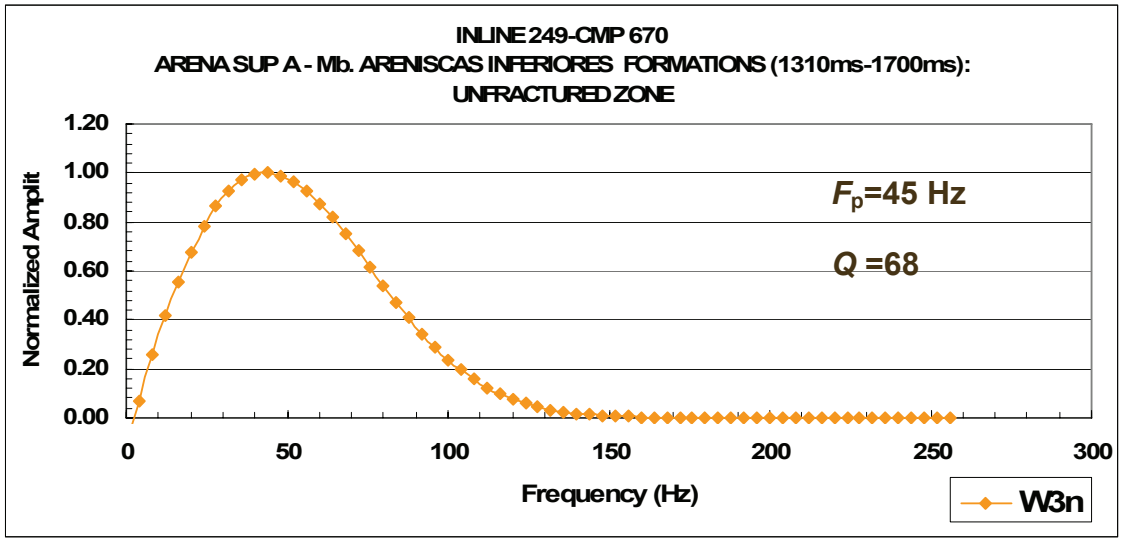

Figure 6.1.c. Normalized amplitude-frequency spectrum for 1310 ms -1700 ms of CMP 670 of inline 249 (unfractured zone).

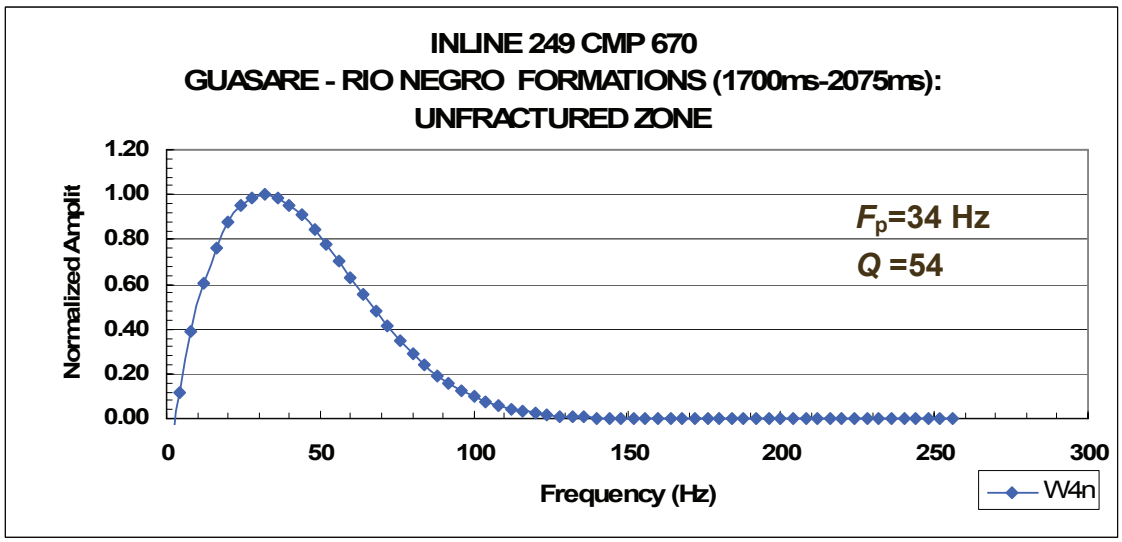

Figure 6.1.d. Normalized amplitude-frequency spectrum for 1170 ms -2075 ms of CMP 670 of inline 249 (unfractured zone).

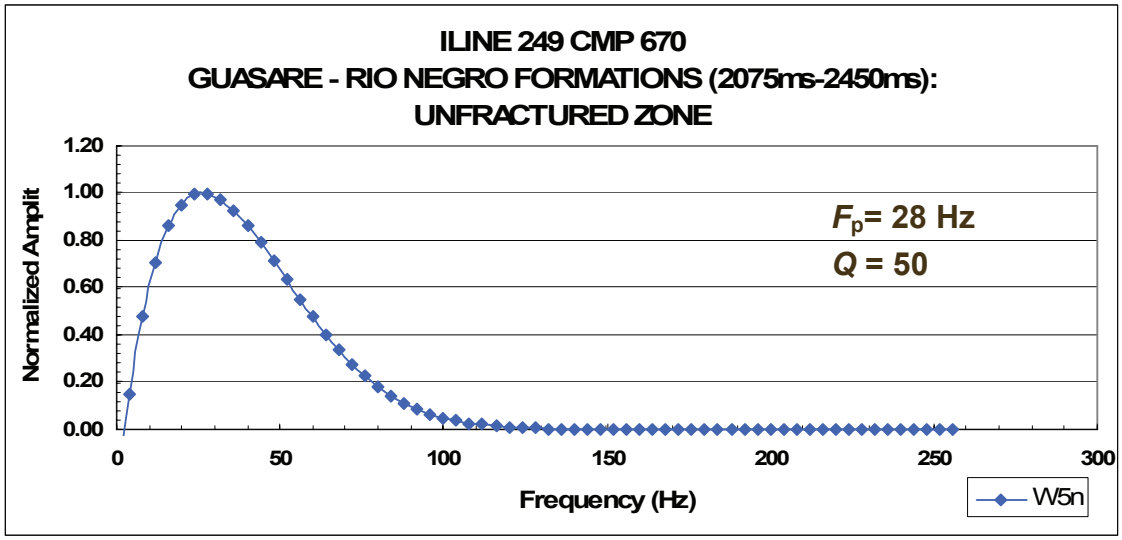

Figure 6.1.e. Normalized amplitude-frequency spectrum for 2075 ms -2450 ms of CMP 670 of inline 249 (unfractured zone).

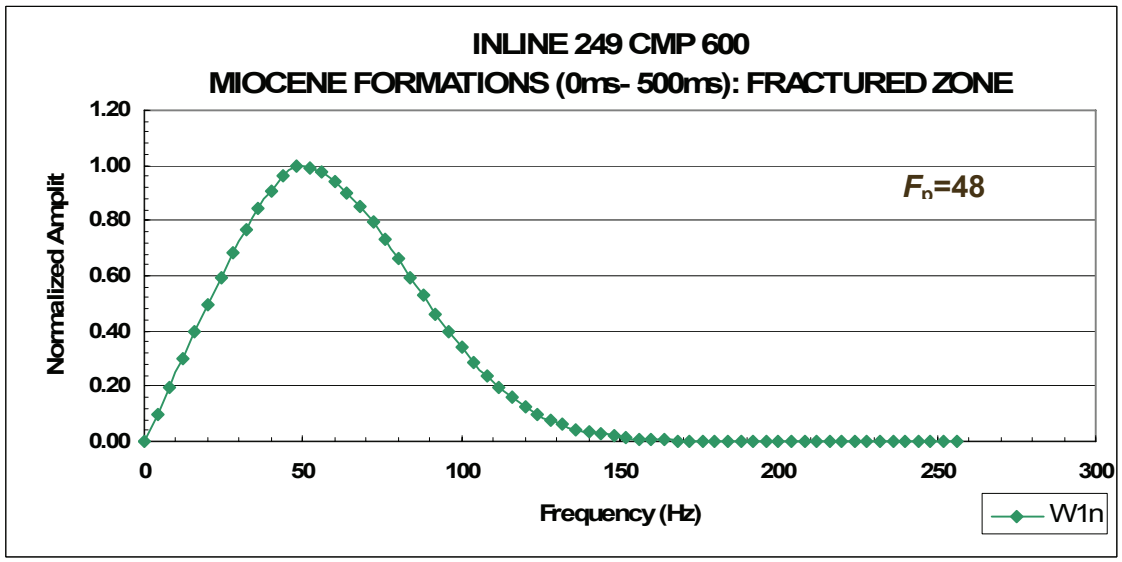

Figure 6.2.a. Normalized amplitude-frequency spectrum for 0.0 ms -500 ms of CMP 600 of inline 249 (fractured zone).

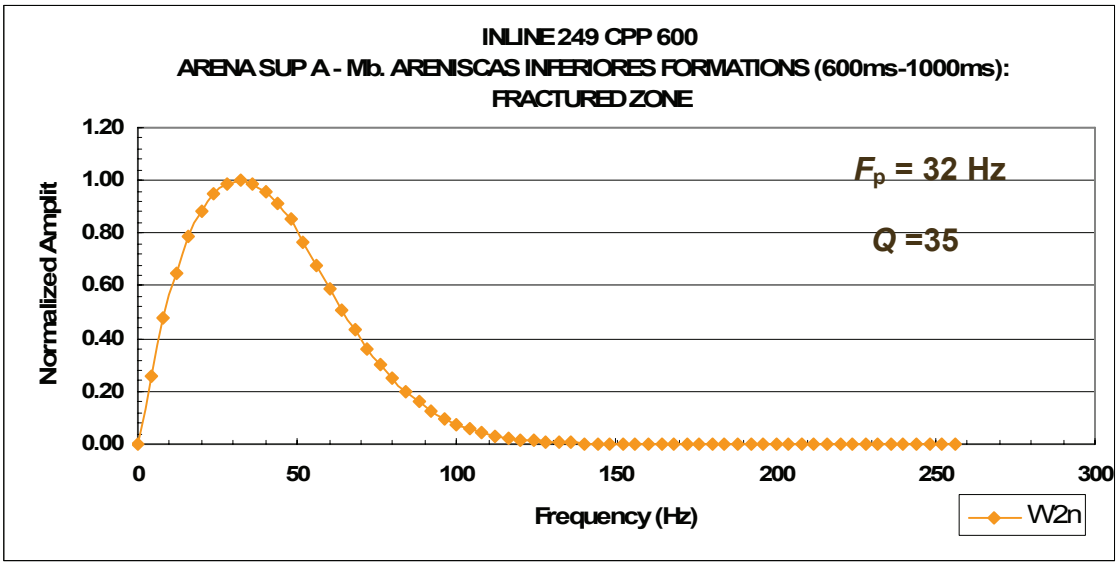

Figure 6.2.b. Normalized amplitude-frequency spectrum for 600 ms -1000 ms of CMP 600 of inline 249 (fractured zone).

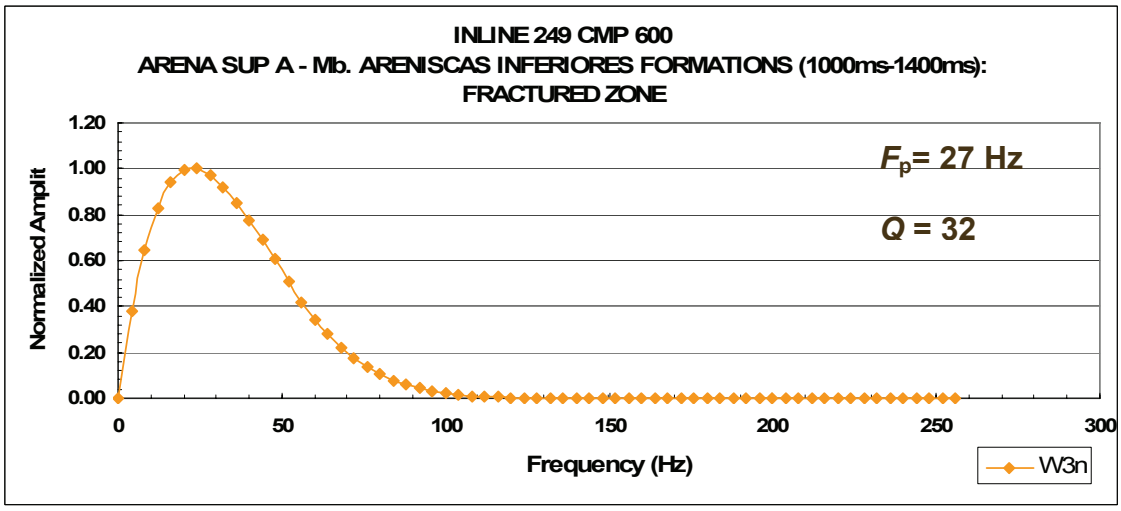

Figure 6.2.c. Normalized amplitude-frequency spectrum for 1000 ms -1400 ms of CMP 600 of inline 249 (fractured zone)**.**

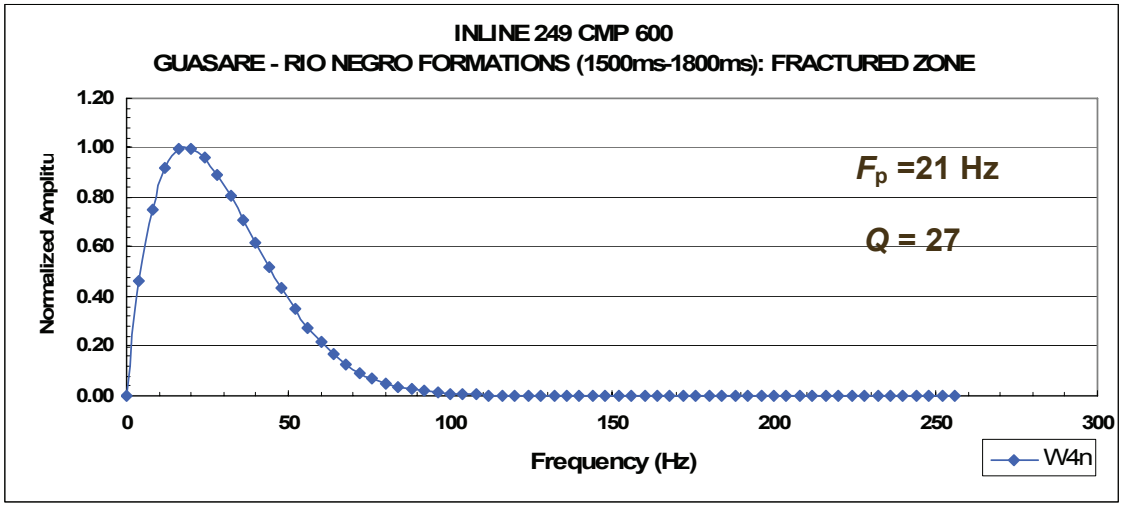

Figure 6.2.d. Normalized amplitude-frequency spectrum for 1500 ms -1800 ms of CMP 600 of inline 249 (fractured zone).

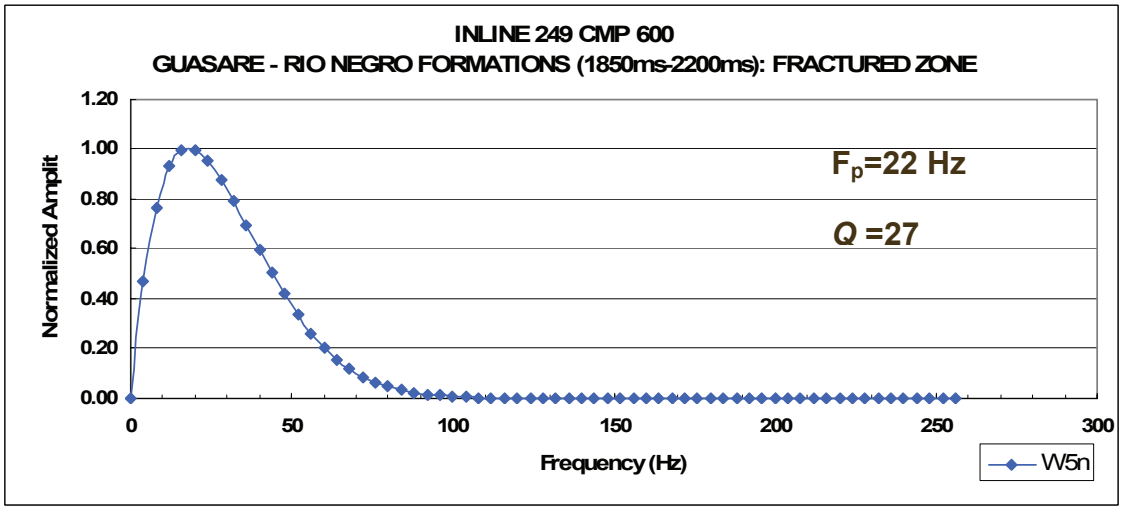

Figure 6.2.e. Normalized amplitude-frequency spectrum for 1850 ms -2200 ms of CMP 600 of inline 249 (fractured zone).

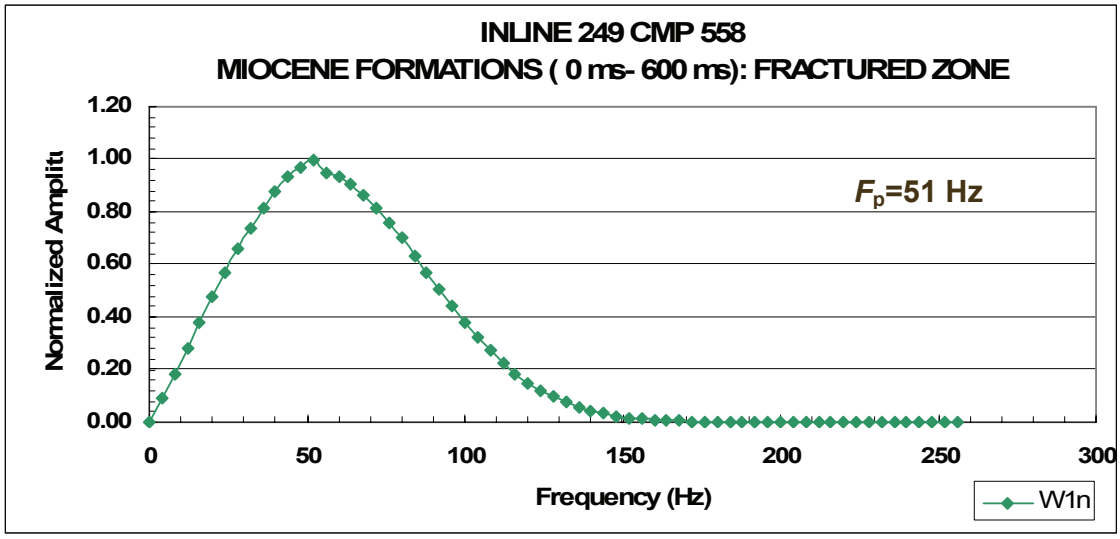

Figure 6.3.a. Normalized amplitude-frequency spectrum for 0.0 ms -600 ms of CMP 588 of inline 249 (fractured zone).

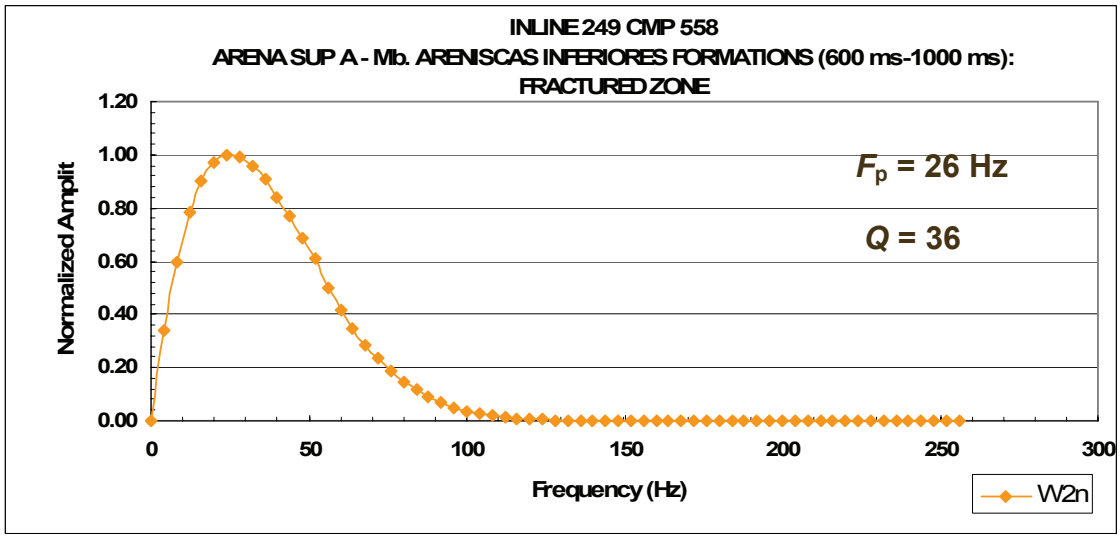

Figure 6.3.b. Normalized amplitude-frequency spectrum for 600 ms -1000 ms of CMP 588 of inline 249 (fractured zone).

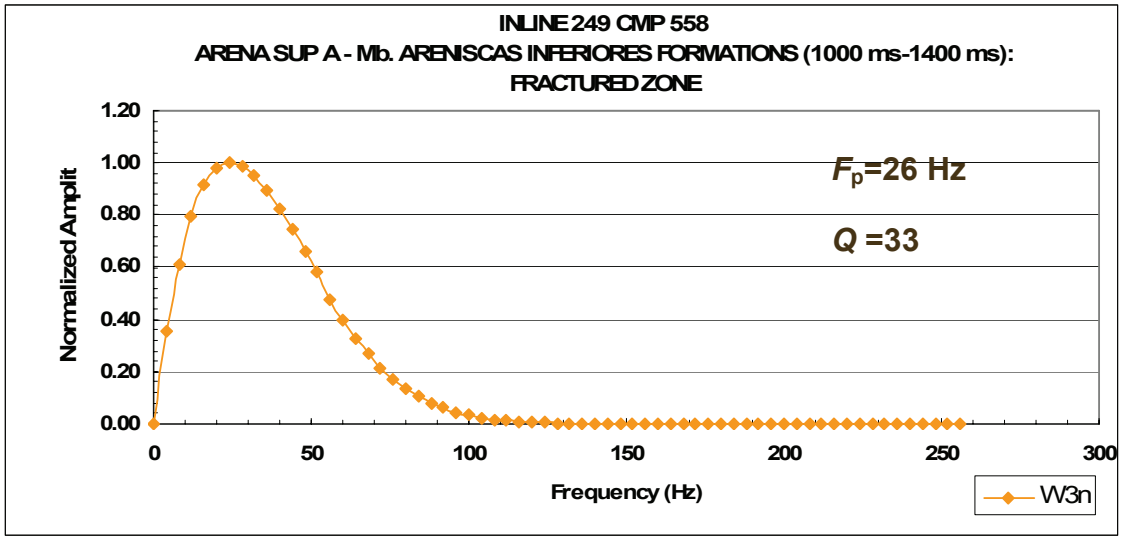

Figure 6.3.c. Normalized amplitude-frequency spectrum for 1000 ms -1400 ms of CMP 588 of inline 249 (fractured zone).

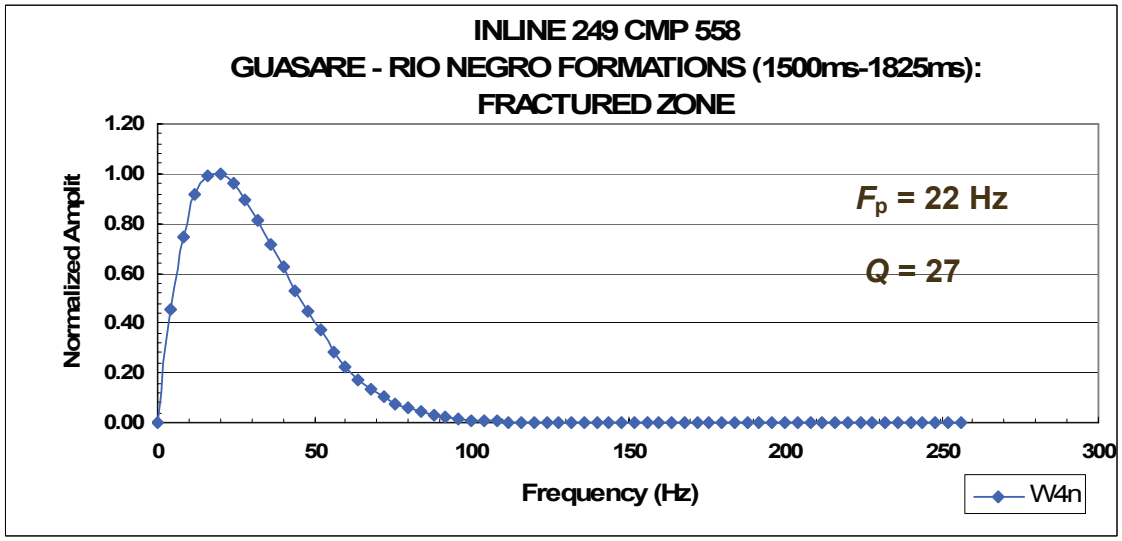

Figure 6.3.d. Normalized amplitude-frequency spectrum for 1500 ms -1825 ms of CMP 588 of inline 249 (fractured zone).

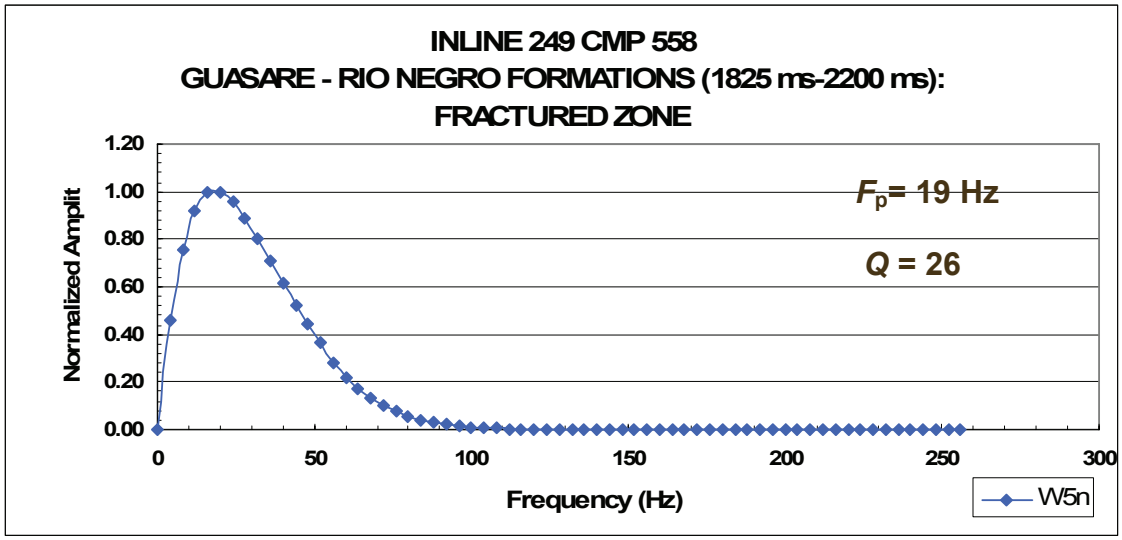

Figure 6.3.e. Normalized amplitude-frequency spectrum for 1825 ms -2200 ms of CMP 588 of inline 249 (fractured zone).

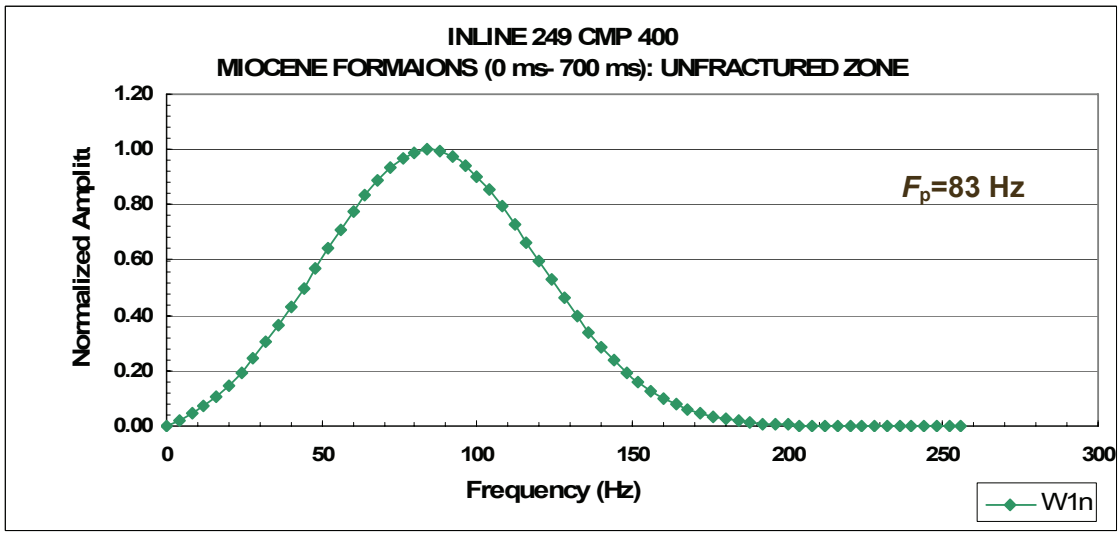

Figure 6.4.a. Normalized amplitude-frequency spectrum for 0.0 ms -700 ms of CMP 400 of inline 249 (unfractured zone).

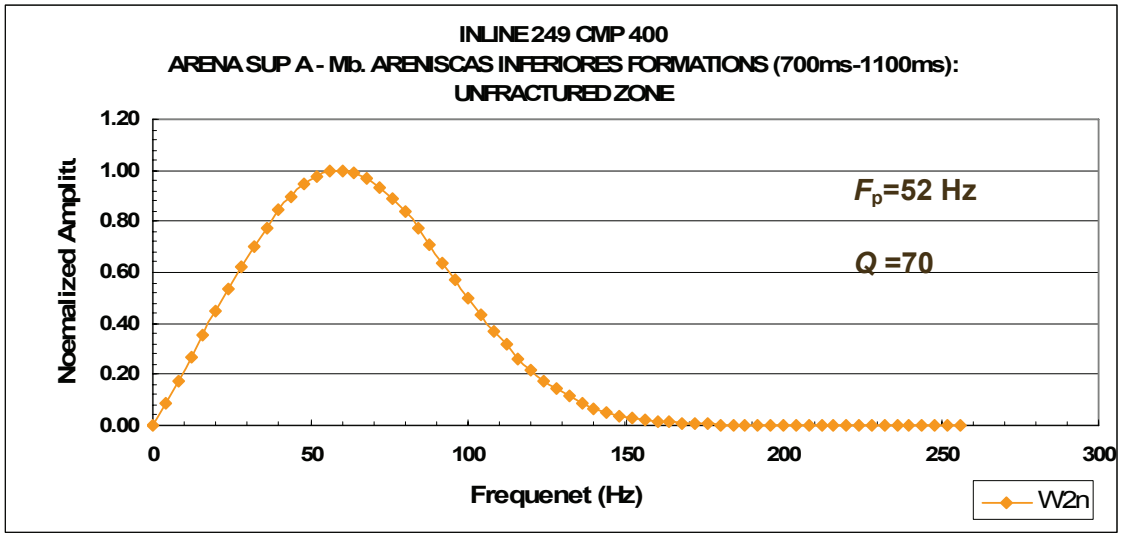

Figure 6.4.b. Normalized amplitude-frequency spectrum for 700 ms -1100 ms of CMP 400 of inline 249 (unfractured zone).

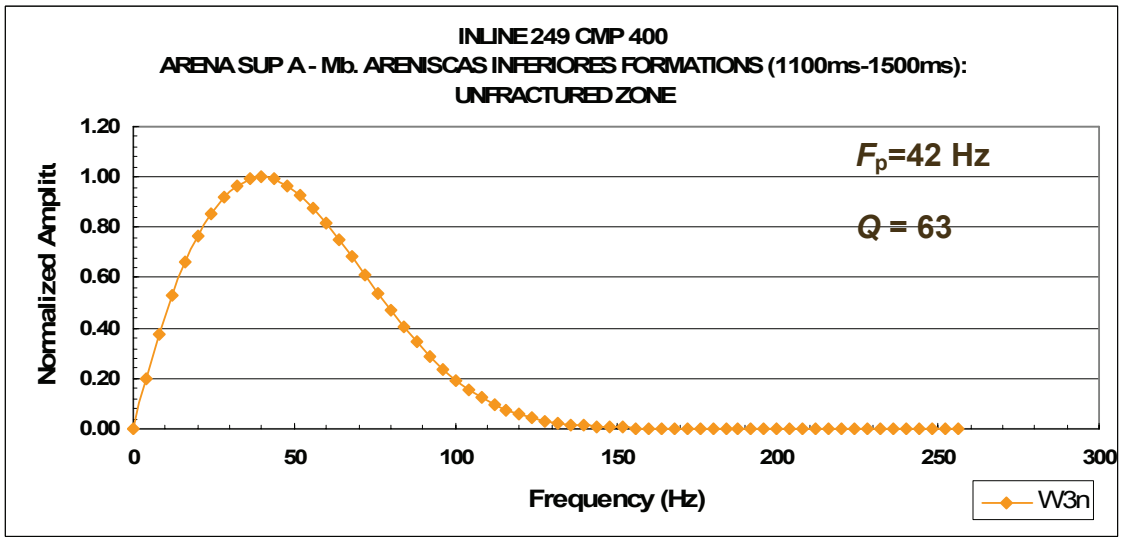

Figure 6.4.c. Normalized amplitude-frequency spectrum for 1100 ms -1500 ms of CMP 400 of inline 249 (unfractured zone).

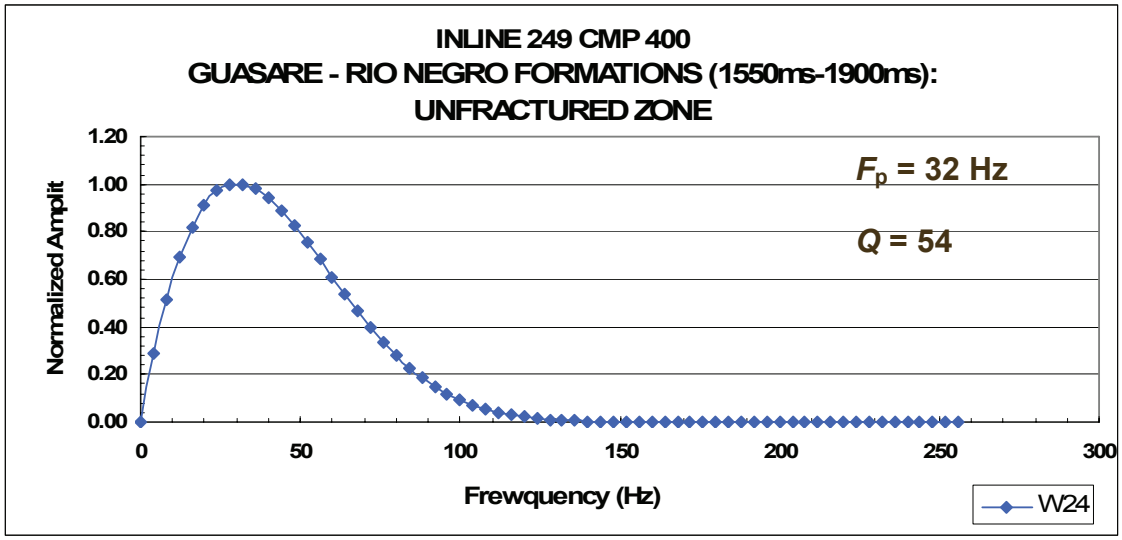

Figure 6.4.d. Normalized amplitude-frequency spectrum for 1550 ms -1900 ms of CMP 400 of inline 249 (unfractured zone).

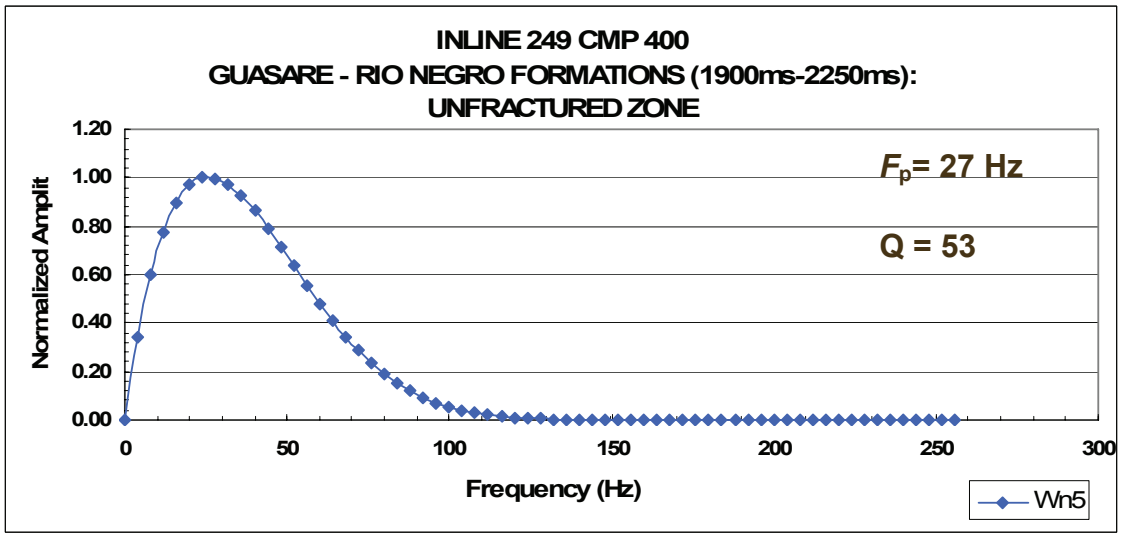

Figure 6.4.e. Normalized amplitude-frequency spectrum for 1900 ms -2250 ms of CMP 400 of inline 249 (unfractured zone).

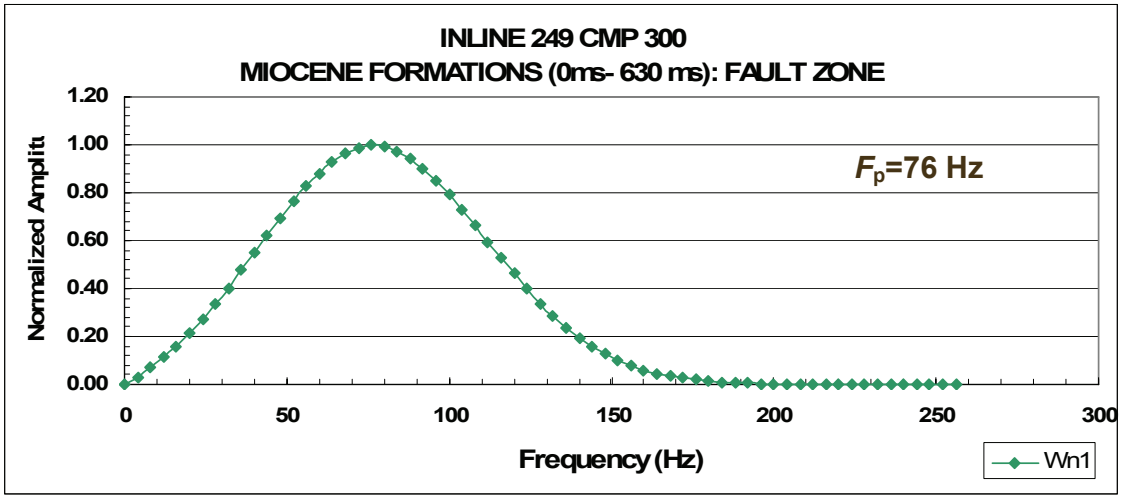

Figure 6.5.a. Normalized amplitude-frequency spectrum for 0.0 ms -630 ms of CMP 300 of inline 249 (fault zone).

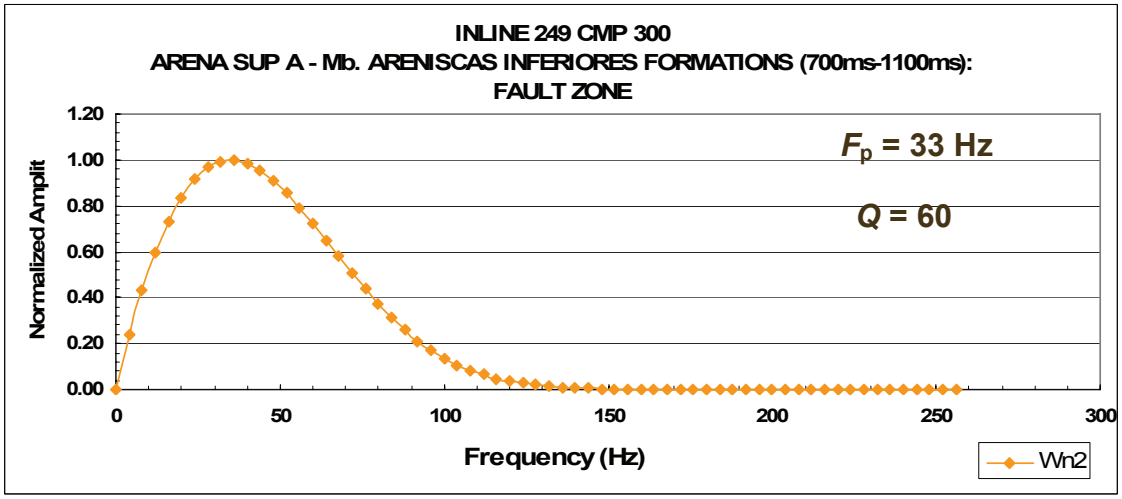

Figure 6.5.b. Normalized amplitude-frequency spectrum for 700 ms -1100 ms of CMP 300 of inline 249 (fault zone).

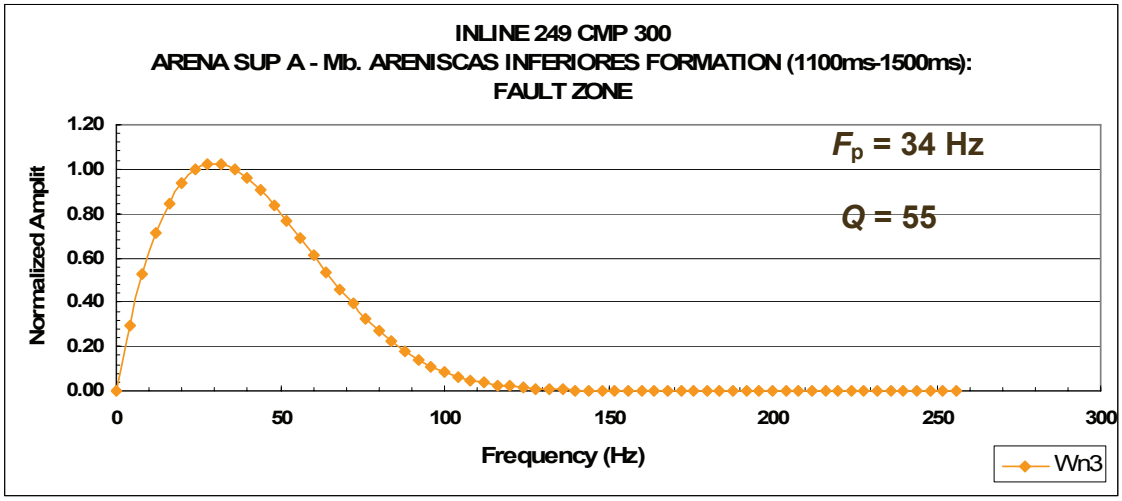

Figure 6.5.c. Normalized amplitude-frequency spectrum for 1100 ms -1500 ms of CMP 300 of inline 249 (fault zone).

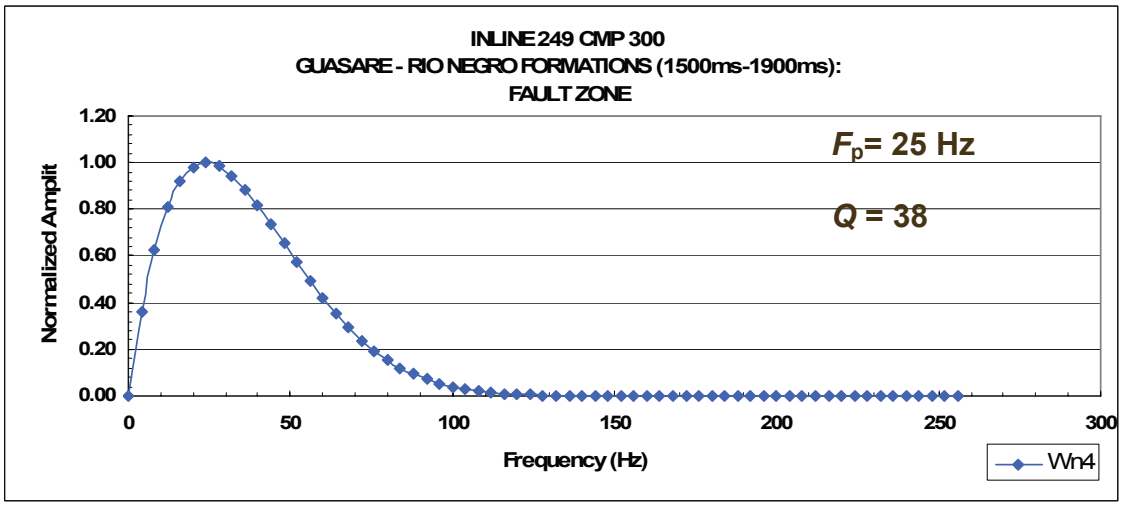

Figure 6.5.d. Normalized amplitude-frequency spectrum for 1500 ms -1900 ms of CMP 300 of inline 249 (fault zone).

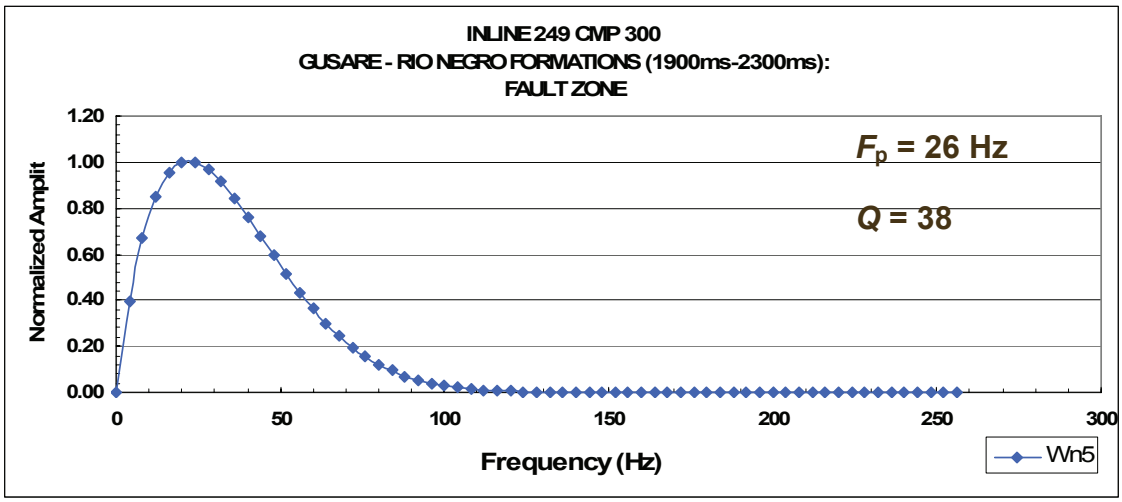

Figure 6.5.e. Normalized amplitude-frequency spectrum for 1900 ms -2300 ms of CMP 300 of inline 249 (fault zone).

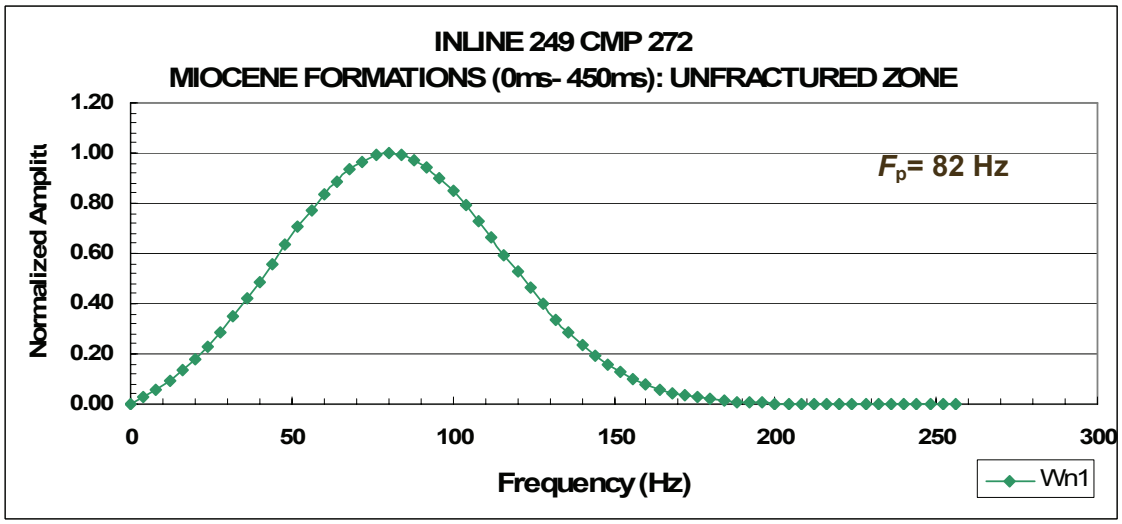

Figure 6.6.a. Normalized amplitude-frequency spectrum for 0.0 ms -450 ms of CMP 272 of inline 249 (unfractured zone).

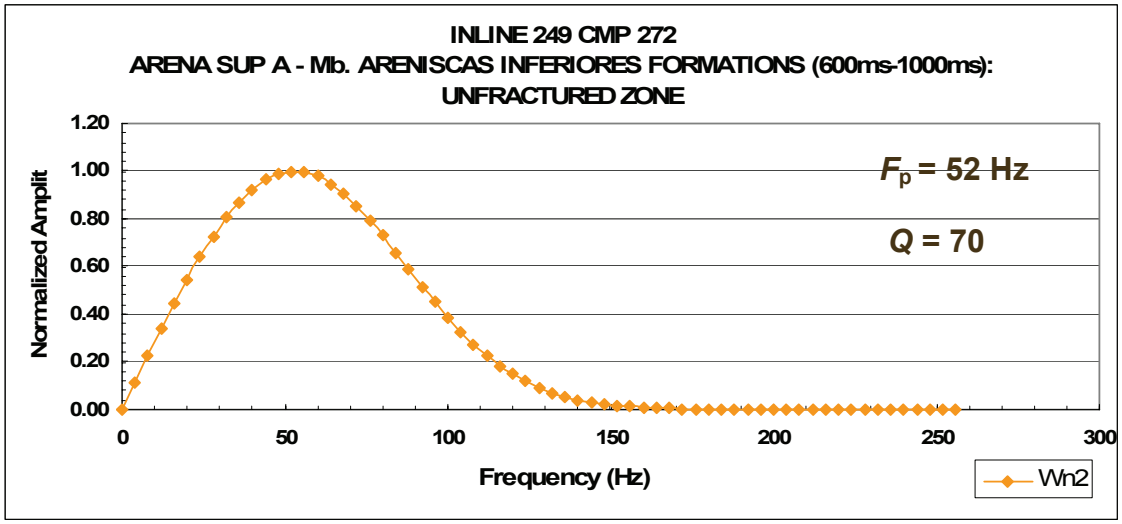

Figure 6.6.b. Normalized amplitude-frequency spectrum for 600 ms -1000 ms of CMP 272 of inline 249 (unfractured zone).

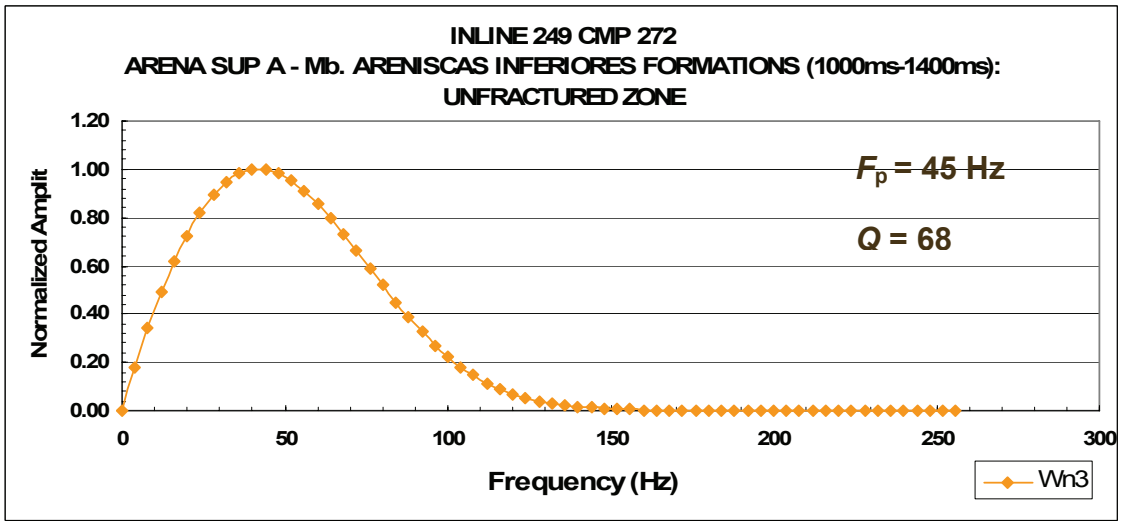

Figure 6.6.c. Normalized amplitude-frequency spectrum for 1000 ms -1400 ms of CMP 272 of inline 249 (unfractured zone).

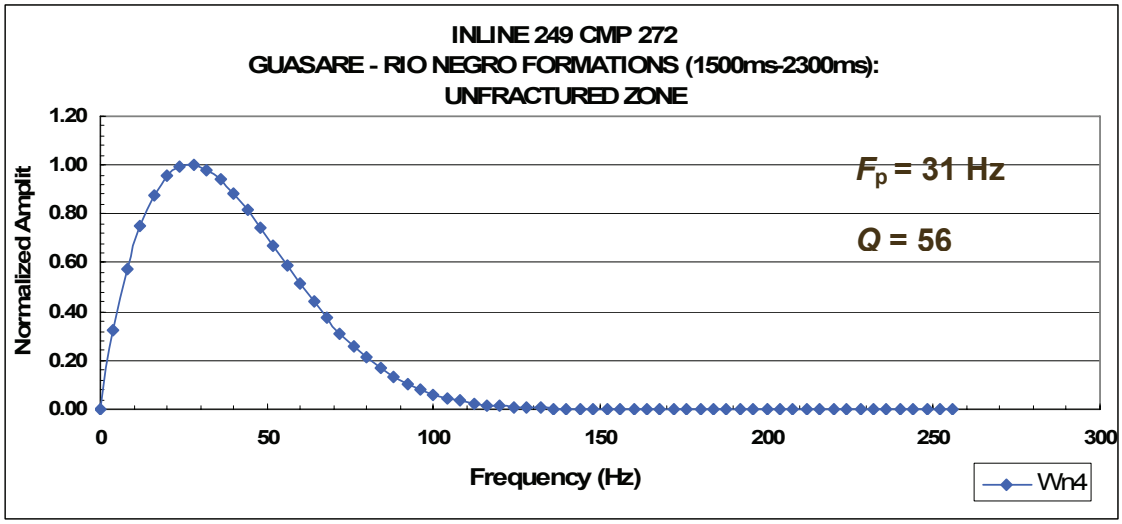

Figure 6.6.d. Normalized amplitude-frequency spectrum for 1500 ms -1900 ms of CMP 272 of inline 249 (unfractured zone).

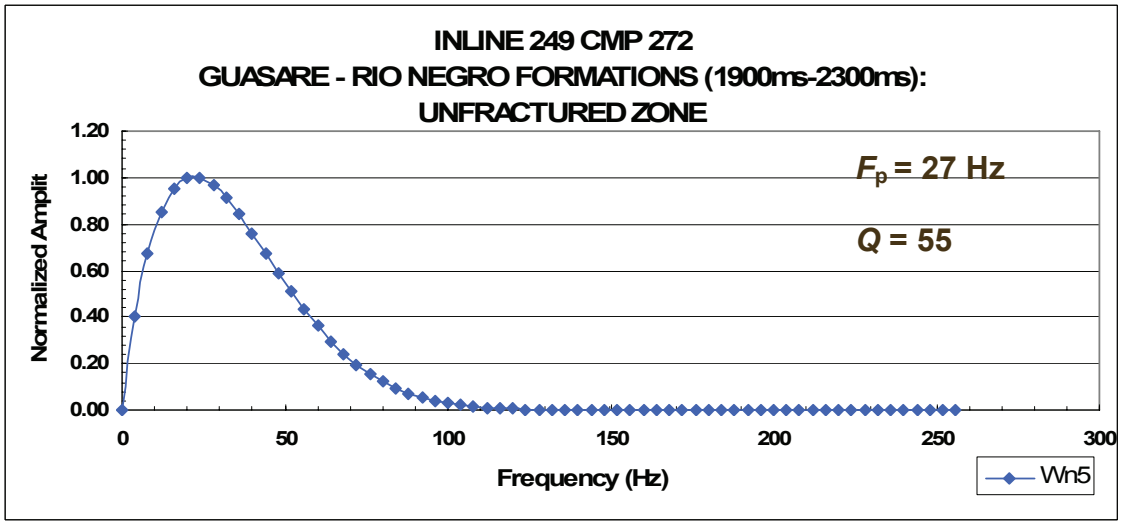

Figure 6.6.e. Normalized amplitude-frequency spectrum for 1900 ms -2300 ms of CMP 272 of inline 249 (unfractured zone).

Table 6.1 Summary of the peak frequency F_p and quality factor $Q_{seismic}$ for six CMP gathers of seismic inline 249. Quality factor $Q_{seismic}$ and Peak frequencies F_p are indicative of relative attenuation in different time windows. Important data in bold (for approximate time reference, see Figures 5.12-5.17).

Name of Formation	Peak Frequency /Quality Factor $Q_{seismic}$	CMP Number					
		670 Unfractured Zone	600 Fractured Zone	558 Fractured Zone	400 Unfractured Zone	300 Fault Zone	272 Unfractured Zone
Miocene Formations	$F_{p\ (Hz)}$	87	**48**	**51**	83	**70**	82
Arena Sup A – Mb. Areniscas Inferiores Formations (Upper Window)	$F_{p\ (Hz)}$	53	**32**	**26**	52	**53**	52
	$Q_{seismic}$	75	**35**	**36**	70	**60**	70
Arena Sup A – Mb. Areniscas Inferiores Formations (Lower Window)	$F_{p\ (Hz)}$	45	**27**	**26**	42	**34**	45
	$Q_{seismic}$	68	**32**	**33**	63	**55**	68
Guasare – Rio Negro Formations (Upper Window)	$F_{p\ (Hz)}$	34	**21**	**22**	32	**25**	31
	$Q_{seismic}$	54	**27**	**27**	54	**38**	56
Guasare – Rio Negro Formations (Lower Window)	$F_{p\ (Hz)}$	28	**22**	**19**	27	**26**	27
	$Q_{seismic}$	50	**27**	**26**	53	**38**	55

The $Q_{seismic}$ values observed in Table 6.1 reflect distinctive vertical and lateral variations along the seismic line 249. The fracture and fault zones covered by CMP gathers 600, 558, and 300 show relatively lower $Q_{seismic}$ values through ASA-MAI and G-RN Formations. The $Q_{seismic}$ values in the upper time window through ASA-MAI Formations are 35 and 36 at CMP 600 and CMP 558 respectively, and 32 and 33 in the lower time window (Table 6.1). Through G-RN, Formations, the $Q_{seismic}$ values decrease to 27 and 27 in the upper time window and to 27 and 26 in the lower time window for the same CMP gathers 600 and 558.

Across the faulted zone, the $Q_{seismic}$ value at CMP gather 300 ranges from 60 to 55 in the upper and lower time windows through ASA-AMI Formations. The $Q_{seismic}$ value then lowers to 38 in the upper and lower time windows through G-RN Formations.

In contrast to the fracture and fault zones, the un-fractured zones at CMP gather 670, CMP gather 400 and CMP gather 272 exhibit higher values of $Q_{seismic}$. The $Q_{seismic}$ values at CMP gather 670 are 75 and 68 through ASA-MAI Formations in the upper windows. But these $Q_{seismic}$ values lower through G-RN Formations to 54 in the upper time window and 50 in the lower time window. At CMP gather 400, the $Q_{seismic}$ values through ASA-AMI Formations range from 70 in the upper time window to 63 in the lower time window. Through the G-RN Formations, the $Q_{seismic}$ is 54 in the upper time window and 53 in the lower time window. Finally, $Q_{seismic}$ values at CMP gather 272 vary from 70 in the upper

time window to 68 in the lower time window through ASA-MAI Formations. But through G-RN Formations, these values decrease to 56 in the upper time window and to 55 in the lower time window. The following section presents comparison of the $Q_{seismic}$ values and measured $Q_{core.}$

6.3 Geological Validation of $Q_{seismic}$

In Table 6.1, this study presents the $Q_{seismic}$ values of 54 and 50 from CMP gather 670 through GRN Formations as calculated from seismic data, inline 249 (Figure 2.1). An average $Q_{seismic}$ value of 52 is correlated with an average Q_{core} value of 56 which was obtained from G-RN Formations core measurements conducted by Gebretsadik (2005) in the Borehole 276 (Figure 1.2) for the depth from 10450 ft to 11541 ft using three confining pressure values of 5372 psi , 5372 psi, and 5753 psi in order to simulate the borehole conditions at the depth of 10462 ft, 10896.3 ft, and 11506.8 ft. In addition, the experiment was carried out at 750 kHz. Table 6.2 summarizes the comparison results of Q_{core} and $Q_{seismic}$ values in the unfractured zones of G-RN Formations.

Table 6.2 Comparisons of Q_{core} values with $Q_{seismic}$ values.

Q from Core Measurements (Well 276)		Q from Surface Seismic Data (Inline 249-CMP 760)		
Depth (ft)	Q_{core}	Depth	Two-way Times	$Q_{seismic}$
		10703	1700	
11133.80	22.78			
11135.90	20.94			
11163.90	61.70			
11198.70	36.62			
11214.80	89.56			
11220.50	59.94			
11242.50	70.23			
11259.50	89.24			
11283.20	63.12			54
11290.80	48.89			
11293.50	72.28			
11300.90	99.62			
11301.50	20.54			
11307.90	59.20			
11322.00	39.66			
11330.20	27.21			
11345.60	92.79			
11347.70	69.26			
11363.00	33.19			
11390.60	60.66	11383	2075	
11408.00	26.25			
11442.10	87.48			
11450.90	55.38			
11484.20	63.02			
11504.50	69.72			50
11520.20	46.65			
11529.40	23.54			
11541.10	61.74			
		12014	2450	
Average Q	56			52

6.4 Summary and Conclusions

The travel-times analysis through the fracture zones of ASA-MAI and G-RN Formations were calculated and the values of the seismic quality factor Q_{seismic} for the six selected DCP gathers of inline 249 were computed using the Gaussian function. It is concluded that the total travel-times it takes the seismic waves to travel through ASA-MAI and G-RN Formations is longer than the total travel-times it takes the sonic waves and suggests greater attenuation of the seismic waves. It is also concluded that the low values of the seismic quality factor Q_{seismic} may help discriminate the leaking faults from sealing faults. An average computed Q_{seismic} value is compared to the measured Q_{core}.

CHAPTER 7

SYNTHESIS, CONCLUSIONS, AND RECOMMENDATIONS

Synthesis

Analysis of seismic attributes, velocity and *Q* of a 3-D seismic volume over La Concepcion Field, onshore La Maracaibo, Venezuela, provide not only the delineation of major fault zones but also may reveal aspects of their possible permeable-impermeable nature with respect to hydrocarbon migration.

With respect to the specific problem of leaky faults in this field's petroleum system, the syllogistic logic is as follows:

1. La Luna is the source rock for the of gas and oil (Parnaud et al, 1995) in the upper reservoirs of the field and must migrate through a vertical pathway, i.e. Faults.
2. The Borehole (C-270) on the inline 164 on a closed structure produces oil and gas in the Misoa and La Luna Formations and these formations are clearly connected by a fault zone to lower La Luna, thus establishing the faults as petroleum conduits from the source rock to the reservoir rocks..
3. The Borehole (C-152) on a closed structure on inline 249 is dry, though the Misoa and La Luna Formations are clearly connected by faults zone to La Luna, thus establishing these faults to be impermeable to hydrocarbon migration..

4. The $Q_{seismic}$ values of fault zone proximal to Borehole C-270 are low, whereas the $Q_{seismic}$ values of fault zone proximal to Borehole C-152 are high.
5. Therefore, low $Q_{seismic}$ in fault zones proximal to the Borehole C-270 suggests attenuation owing to permeability and porosity and the high $Q_{seismic}$ in near the Borehole C-152 proximal to fault zones suggests less attenuation owing to low fault zone permeability and porosity.

Conclusions

1. An application of variance cube attribute to La Concepcion 3-D seismic data delineates the location of fault and fracture zones along a northeast-southwest general trend.
2. The image ray perturbation analysis serves as an interval velocity estimation method indicates that the seismic waves traveling through ASA-MAI Formations near the fracture zone are affected the most.
3. The interval velocity comparisons consistently indicate low velocity zones through ASA-MAI and G-RN Formations and suggest possible fluid effects proximal to permeable fault zones.
4. The Fourier transform analysis supportingly reveals that the peak frequencies at the fractured zones are lower than those at the unfractured zones, suggesting fluid effects or leaking faults.
5. The travel-times analysis indicates that the total traveltime it takes the seismic waves to travel through ASA-MAI and G-RN Formations is longer than the

time it takes the sonic waves and suggests greater attenuation of the seismic waves.

6. It is also concluded that the low values of the seismic quality factor $Q_{seismic}$ may help discriminate the leaking faults from sealing faults. And average computed $Q_{seismic}$ value is compared to the measured Q_{core}.

Recommendations

The above qualitative results addressing the physical aspects of faults as detected by reflection seismic are useful for oil/gas exploration and development not just in La Concepcion Field, but elsewhere. However, though these qualitative results are encouraging, quantitative future work should be conducted to establish a quantitative relationship between fault zone permeability and *Q*. For example, possible additional seismic extracted *Q* should be validated proximal to core measurements of *Q*. If possible, investigations of sensitivity analyses of size of layers to seismic *Q* analysis also should be performed. Finally, quantification of the effects of sealing versus non-sealing faults (e.g. fault gouge ratios) should be compared to the *Q* analyses along the faults. In this manner, the questions which this dissertation asked may be answered, InshaAllah, or at the very least, they may lead to more questions, which is, after all, the normal outcome of the geoscientific investigation.

REFERENCES

Amery, G., 1993. Basics of Seismic Velocities. The Leading Edge, November 1993, 1087-1091.

Bahorich, M. and Farmer, S., 1995. 3-D Seismic Discontinuity for Faults and Stratigraphic Features: The Coherence Cube. The LEADING EDGE, October 1995, 1053-1058.

Cardozo, L.E., 2001. Integrated Geological Geophysical Reservoir Characterization of the Lower Middle Cretaceous Cogollo group limestone, La Concepcion Field, Venezuela. University of Oklahoma. M.S. Thesis. 75 pages.

Chen M. Andre, 2002, Using 3-D Seismic Attributes to Predict the Net Sand Thickness of the Upper Dakota Parasequence. http://www.eps.mcgill.ca/~hart/dakota/indiestudy.htm#iph

Dix, C., 1955. Seismic Velocities from Surface Measurements. Geophysics, vol. xx., No. 1, p. 68-86.

Escalona A., and Mann P., 2006, Tectonic controls of the right-lateral Burro Negro tear fault on Paleogene structure and Stratigraphy, Northeastern Maracaibo Basin. AAPG Bulletin, v. 90, No. 4, pp. 479-504.

Fagin, W. S., 1996. Seismic Modeling of Geologic Structures: SEG-Geophysical

Development, No. 2.

Ferro, E., Peralta, E. and Marachal, D. 2001. Development of a fractured reservoir in a mature oil field: La Concepcion Field (Cretaceous) Maracaibo Basin, Venezuela. EXITEP. Mexico 11 pages.

Gebretsadik, E., 2005, Geologically and Well-Log Constrained Quality Factor (Q) Analysis for Seismic Reservoir Characterization. University of Oklahoma. PhD. Dissertation. 154 pages.

Gelchinsky, B., Landa, E. and Shtivelman, V., 1985. Algorithms of phase and group correlation. Geophysics, 50, 596-608.

GX II Technological Corporation, 1995: GX user's Guide.

Haq, B., M. Jervey and P.R. Vail, 1988. Mesozoic and Cenozoic chronostratigraphy and eustatic cycles. SEPM, Sea-Level changes: an integrated approach. Espc., 42: 71-108.

Hoang, N.T.B., 2005, Two-Dimensional Basin Analysis of La Concepcion Field, Maracaibo Basin, Venezuela: Masters Thesis, University of Oklahoma, 128p.

Hubral, P., 1977**.** Time Migration-Some Ray Theoretical Aspects. Geophysical Prospecting 25, 738-745.

IESX ®, reference guide. 1998. Geoframe IESX Seismic Data Interpretation. Schlumberger, Texas.

Lugo, J. 1991, Tectonics and Stratigraphics history of the Maracaibo Basin. Austin University of Texas. Ph.D. Thesis. 142 pages.

Lugo, J. and Mann P., 1995, Jurassic-Eocene tectonic evolution of Maracaibo Basin, Venezuela. Amer. Assoc. Petrol. Geol. Memoir " Petroleum Basins of south America", pages: 699-725.

Marinic, D., Larson, G., Gray, D., Soule, G., Zheng, Y., and Pelletir, J., 2004, Identifying vertical productive fractures in the Narraway gas field using the envelope of seismic anisotropy. CSEG National Convention 2004.

Metwalli, F. I., Pigott, D. J., 2005, Analysis of petroleum system criticals of the Matruh-Shushan Basin, Western Desert, Egypt. Petroleum Geocience, Vol. 11, pp. 157-178.

Neidell, N.S., and Taner, M.T., 1971. Semblance and other Coherency Measures for Multichannel Data. Geophysics. Vol. 36, No. 3, p. 482-497.

Nissen, S., 2000, Interpretive Aspects of Seismic Coherence and Related Multi-Trace Attributes**.** **http://www.kgs.ku.edu/PRS/publication/2000/ofr84/index.html.**

Nissen, S., 2002. Seismic Attributes for Explorationist. **http://www.kgs.ku.edu/PRS/publication/2002/ofr49/index.html.**

Sheriff, R. E., 1973. Encyclopedic dictionary of exploration geophysics. Tulsa, Society of Exploration Geophysicits.

Talukdar, S., Gallango, O., and Rugglero, A., 1985, Formaciones La Luna y Querrecual: rocas madres de potroleo: *in* Espejo , A., Rios, J.H., de Bellizzia, N.P., and de Pardo, A.S., Memoria: VI Congreso

Geologico Venzeuelano, Memorias. Sociedad Venezolana de Geologos, Caracas, p. 3606-3642.

Taner, M. T., 2000. Attributes revisited. **http://www.rocksolidimages.com/pdf/attrib_revisited.htm#_Toc494264879.**

Taner, M. T., and Sheriff, R.E., 1979**.** Complex Seismic Trace Analysis. Geophysics. Vol. 44, No. 6, p. 1041-1063.

Taner, M. T., and Koehler, F., 1969. Velocity Spectra-Computer Derivation and Applications of Velocity Functions. Geophysics. Vol. 34, No. 6, p. 859-881.

Tipsword, H. L., F. M. Seltzer and F. L. Smith Jr, 1966. Interpretation of depositional environment in Gulf Coast petroleum exploration from paleoecology and related stratigraphy: Transaction the Gulf Coast Association of Geological Society, vol. 16, pages: 119-130.

West, J., ed., 1996, International Petroleum Encyclopedia: Pennwell Publishing Co., Tulsa, p. 110, 186-187.

Yilmaz, O., 2001. Seismic Data Analysis: Processing, Inversion, and Interpretation of Seismic Data, V. II. Society of Exploration Geophysicists (SEG).